

May 2016

# Numerical and Experimental Studies of Atomic Layer Deposition for Sustainability Improvement

Dongqing Pan

*University of Wisconsin-Milwaukee*

Follow this and additional works at: <https://dc.uwm.edu/etd>

 Part of the [Film and Media Studies Commons](#), [Mechanical Engineering Commons](#), and the [Nanoscience and Nanotechnology Commons](#)

---

## Recommended Citation

Pan, Dongqing, "Numerical and Experimental Studies of Atomic Layer Deposition for Sustainability Improvement" (2016). *Theses and Dissertations*. 1187.

<https://dc.uwm.edu/etd/1187>

This Dissertation is brought to you for free and open access by UWM Digital Commons. It has been accepted for inclusion in Theses and Dissertations by an authorized administrator of UWM Digital Commons. For more information, please contact [open-access@uwm.edu](mailto:open-access@uwm.edu).

NUMERICAL AND EXPERIMENTAL STUDIES OF ATOMIC LAYER  
DEPOSITION FOR SUSTAINABILITY IMPROVEMENT

by

Dongqing Pan

A Dissertation Submitted in  
Partial Fulfillment of the  
Requirements for the Degree of

Doctor of Philosophy  
in Engineering

at

The University of Wisconsin- Milwaukee

May 2016

ABSTRACT  
NUMERICAL AND EXPERIMENTAL STUDIES OF ATOMIC LAYER  
DEPOSITION FOR SUSTAINABILITY IMPROVEMENT

by

Dongqing Pan

The University of Wisconsin-Milwaukee, 2016  
Under the Supervision of Professor Chris Yingchun Yuan

Atomic layer deposition (ALD) is an approved nano-scale thin films fabrication technique with remarkable uniformity and conformity in surface geometry. This dissertation presents numerical and experimental studies to investigate the transient physical and chemical ALD process in order to improve its sustainability performance in terms of throughput, wastes and emissions.

To be specific, in this dissertation, the transient process of ALD is studied extensively through both numerical and experimental approaches to find the influential factors on the two main critical sustainability issues: low throughput and negative environmental impacts. Different numerical schemes are developed and studied for ALD process simulations. In particular, the gas fluid dynamics of the carrier gas flow is studied numerically by introducing and comparing two Lattice Boltzmann Method (LBM) models. To account for the surface deposition process, the strong-coupled physical and chemical process of ALD is recovered numerically by Finite Volume Method (FVM). The 3D transient reactive

thermal-fluid dynamic model adopts surface reaction kinetics and mechanisms based on the atomic-level calculations to study the surface deposition process.

Experimental investigations are carried out to characterize the growth rate under different deposition conditions. The experimental observations are correlated with the simulations for better understanding the transient physical and chemical ALD process. The experimentally-validated numerical model is further applied for in-depth investigation of two types of batch and spatial ALD process for throughput improvement. A multi-wafer batch ALD with vertical and horizontal wafer arrangements is studied to investigate the influences of wafer layout on the deposition process with both experimental and numerical approaches. An in-line spatial ALD is also studied numerically to investigate three geometric and process factors, gap size, temperature, and pressure on the precursor intermixing and chemical deposition process. Spatial ALD is shown significantly effective in improving the throughput of ALD thin film depositions.

To study the adverse environmental impacts of ALD nano-manufacturing technology on  $\text{Al}_2\text{O}_3$  nano-scale thin films, numerical simulations with detailed ALD surface reaction mechanisms developed based on Density Functional Theory (DFT) are performed to investigate the effects of four process parameters on ALD film deposition rate, process emissions and wastes. The influential factors on process emissions and wastes are studied and identified.



The studies presented in this dissertation provide valuable knowledge in understanding the transient physical and chemical processes, and identifying the influential process or geometric factors to improve its throughput and minimize its emissions and wastes.

© Copyright by Dongqing Pan, 2016  
All Rights Reserved

To  
my mother,  
who brought me to this beautiful world,  
and left me so early, with such great loneliness

and my grandma,  
who held me in those dark days so tightly, with such great warmth

# TABLE OF CONTENTS

ABSTRACT.....	ii
LIST OF FIGURES .....	x
LIST OF TABLES .....	xvii
ACKNOWLEDGEMENTS .....	xviii
CHAPTER 1 INTRODUCTION .....	1
1.1 Nano-manufacturing and atomic layer deposition .....	1
1.1.1 Nano-manufacturing technology .....	1
1.1.2 Atomic layer deposition.....	4
1.1.3 ALD of Al <sub>2</sub> O <sub>3</sub> .....	8
1.2 ALD applications .....	11
1.2.1 Microelectronics applications .....	11
1.2.2 Energy conversion and storage applications.....	12
1.2.3 Medical and environmental health applications .....	14
1.3 Research motivation and objectives.....	14
1.3.1 ALD sustainability limitations.....	14
1.3.2 Previous research of ALD process .....	16
1.3.3 Research objective and outline .....	19
1.4 Summary and conclusions.....	21
CHAPTER 2 NUMERICAL SIMULATIONS OF ALD FLUID DYNAMICS BY LATTICE BOLTZMANN METHOD.....	22
2.1 Introduction .....	22
2.2 Computational fluid dynamics (CFD) for ALD.....	23
2.3 Lattice Boltzmann Method.....	26
2.3.1 The LBGK-D2Q9 model .....	27
2.3.2 The MRT and TRT models.....	29
2.3.3 Conservation laws.....	32
2.4 Numerical methods .....	32
2.4.1 Two-dimensional geometry .....	33
2.4.2 Boundary conditions and initial conditions .....	34

2.4.3	Numerical parameters setup .....	37
2.4.4	Relation of lattice and physical values .....	38
2.5	Results and discussion.....	39
2.5.1	Simulations of gas flow in ALD: LBGK-D2Q9 vs. TRT.....	39
2.5.2	ALD carrier gas flow characterization and discussion .....	46
2.6	Summary and conclusions.....	48
<b>CHAPTER 3 A COMBINED NUMERICAL AND EXPERIMENTAL STUDY OF THE PHYSICAL AND CHEMICAL DETAILS OF AL<sub>2</sub>O<sub>3</sub> ALD .....</b>		
<b>49</b>		
3.1	Introduction .....	49
3.2	Experiments.....	49
3.3	Mathematical modeling.....	51
3.3.1	Fluid dynamics .....	51
3.3.2	Heat transfer .....	53
3.3.3	Chemical kinetics .....	54
3.3.4	Surface reaction mechanisms .....	56
3.4	Numerical methods .....	58
3.5	Results and discussion.....	59
3.5.1	Experiments: effects of purging time and process temperature.....	59
3.5.2	Numerical investigations .....	64
3.6	Summary and conclusions.....	72
<b>CHAPTER 4 EXPERIMENTAL AND NUMERICAL INVESTIGATIONS OF MULTI-WAFER BATCH ALD FOR THROUGHPUT IMPROVEMENT .....</b>		
<b>75</b>		
4.1	Introduction .....	75
4.2	Experiments.....	79
4.3	Model equations .....	81
4.4	Numerical solutions.....	82
4.5	Results and discussion.....	84
4.5.1	Experimental and numerical characterizations of film deposition rate .....	84
4.5.2	Numerical investigations of ALD transient deposition process .....	90
4.6	Summary and conclusions.....	97

CHAPTER 5 EFFECTS STUDY OF IN-LINE SPATIAL ALD FOR THROUGHPUT IMPROVEMENT .....	99
5.1 Introduction .....	99
5.2 In-line spatial ALD process modeling.....	103
5.3 Numerical implementations .....	104
5.3.1 System boundary definition.....	104
5.3.2 Boundary conditions.....	105
5.3.3 Initial conditions.....	107
5.3.4 Numerical calculations .....	108
5.4 Results and discussion.....	109
5.4.1 Effects on the in-line spatial ALD flow field .....	109
5.4.2 Effects on the in-line spatial ALD chemical depositions .....	116
CHAPTER 6 NUMERICAL MODELING AND EXPERIMENTAL INVESTIGATION OF ALD WASTES AND EMISSIONS FOR SUSTAINABLE NANO-MANUFACTURING.....	124
6.1 Introduction .....	124
6.2 Al <sub>2</sub> O <sub>3</sub> ALD modeling with detailed chemical reaction mechanisms .....	125
6.2.1 Physical process modeling.....	125
6.2.2 Detailed surface reaction mechanism .....	126
6.2.3 Surface chemical kinetics .....	132
6.3 Experiments.....	134
6.4 Results and discussion.....	136
6.4.1 Al <sub>2</sub> O <sub>3</sub> ALD deposition process .....	136
6.4.2 Effects of process parameters on ALD wastes and emissions.....	142
6.5 Summary and conclusions.....	150
CHAPTER 7 CONCLUSIONS AND RECOMMENDATIONS FOR FUTURE STUDY	153
7.1 Conclusions .....	153
7.2 Recommendations for future study .....	157
REFERENCES .....	159
CURRICULUM VITAE.....	171

## LIST OF FIGURES

Figure 1.1 Schematic illustrations of ALD reaction cycles. ....	5
Figure 1.2 Various ALD reactors: (a) Showerhead type single-wafer ALD reactor; (b) Multi-wafer batch ALD reactor; (c) In-line spatial ALD reactor; (d) Roll-to-roll ALD reactor [Delft, et al., 2012]. ....	6
Figure 1.3 Cambridge Nanotech Savannah S100 ALD system consists of precursor cylinders, precursor manifold, carrier gas manifold, chamber, outlet manifold and a vacuum pump (not shown in the figure). ....	7
Figure 1.4 TEM of high-k dielectric with metal gate for 45 nm PMOS transistor with ALD-deposited high-k $\text{Al}_2\text{O}_3$ dielectric [Mistry, et al., 2007]. ....	9
Figure 1.5 Cross-sectional SEM image of an 300 nm $\text{Al}_2\text{O}_3$ ALD thin film on a Si wafer with a trench structure for DRAM application [George, 2010]. ....	10
Figure 2.1 Comparisons of CFD models and their preferred application range [Raabe, 2004]. ....	24
Figure 2.2 The D2Q9 lattice arrangement in LBM. ....	28
Figure 2.3 Two-dimensional geometry of ALD vacuum reactor based on Cambridge Nanotech's Savannah S100 ALD system. Grey area denotes the solid wall nodes, and white is the fluid domain. Chamber is connected with the inlet pipe and outlet pipe. Wafer is located in the center of the chamber. ....	33
Figure 2.4 Scheme of bounce-back boundary condition for the solid wall nodes (grey) in the domain. ....	34

Figure 2.5 Scheme of velocity boundary condition which is applied at the inlet. Velocities in both x and y directions are specified.....35

Figure 2.6 Dimensionless velocity magnitude contour plots of carrier gas in ALD for incompressible flow by D2Q9: (a) viscosity relaxation factor  $w_\eta = 1.95$ , (b)  $w_\eta = 1.97$ , (c)  $w_\eta = 1.99$ . .....39

Figure 2.7 Dimensionless velocity magnitude contour plots of carrier gas in ALD for incompressible flow by TRT. (a)  $w_\eta = 1.95$ , (b)  $w_\eta = 1.97$ , (c)  $w_\eta = 1.99$ . .....40

Figure 2.8 Computational efficiency: D2Q9 vs. TRT for incompressible flow simulations...41

Figure 2.9 Dimensionless velocity magnitude contour plots of carrier gas in ALD with compressible ratio (1:0.96) by D2Q9. From (a), (b), (c) to (d):  $w_\eta = 1.74, 1.79, 1.84, 1.89$ . ....42

Figure 2.10 Dimensionless velocity magnitude contour plots of carrier gas in ALD with compressible ratio (1:0.96) by TRT. From (a), (b), (c) to (d): relaxation factor  $w_\eta = 1.74, 1.79, 1.84, 1.89$ . .....43

Figure 2.11 Comparison of velocity (m/s) countour plots by LBM-TRT with conventional continuum-based solver packages. (a) dimensional velocity (m/s) contour plots by LBM, (b) flow simulation result (m/s) by Comsol and Fluent, (c) flow simulation result (m/s) by Fluent. ....44

Figure 2.12 Plots of velocity variations along flow streamline by LBM, Comsol and Fluent, respectively. Position 1 and 2 are located in the inlet area, 3-7 in the chamber, 8 and 9 in the outlet field. It is shown that LBM repeats the velocity variations observed by Comsol and Fluent in the same way.....45

Figure 3.1 Illustrations of surface chemisorption reaction mechanism for: (a) TMA pulse; and (b) water pulse.....57



Figure 3.2 3D computational domain in the numerical model is based on S100 ALD reactor system. There are three inlets, one outlet and surface reactions are enabled only on the chamber bottom wall.....58

Figure 3.3 Al<sub>2</sub>O<sub>3</sub> film growth rate in Å/cycle for: (a) 8s purging experiments; (b) 20s purging experiments. Sample A is located in the inlet area, and sample C in the outlet area..60

Figure 3.4 Comparisons of surface-averaged Al<sub>2</sub>O<sub>3</sub> film growth rates in Å/cycle by experimental and numerical investigations.....63

Figure 3.5 Precursor distributions during the full cycle of flow simulations for: (a) TMA molar fraction for carrier gas flow rate of 20sccm; (b) TMA molar fraction for carrier gas flow rate of 200sccm; (c) Water molar fraction for carrier gas flow rate of 20sccm; (d) Water molar fraction for carrier gas flow rate of 200sccm. A is located in inlet area, and C in the outlet area. ....66

Figure 3.6 Correlations of surface deposition rate of O<s> and TMA molar fraction with coverage of \*Al(CH<sub>3</sub>)<sub>2</sub>(s) for TMA pulsing step at 100°C, 150°C, 200°C and 250°C, respectively. The grey dot lines show the temperature effect on surface deposition.....69

Figure 3.7 Relation of surface deposition rate of Al<s>, H<sub>2</sub>O molar fraction and coverage of species \*OH for water pulsing step at 100°C, 150°C, 200°C and 250°C, respectively. The grey dot lines show the process temperature effect on surface deposition. ....70

Figure 3.8 Surface deposition rate of bulk Al<sub>2</sub>O<sub>3</sub><s> at five different positions in TMA pulsing step for 100°C, 150°C, 200°C and 250°C, respectively. Point A is located in the inlet area, and point C in the outlet area. ....72

Figure 4.1 Schematics of the two main categories of batch ALD systems: (a) vertical stack-type multi-wafer ALD reactor [Granneman, et al., 2007]; and (b) in-line spatial ALD reactor [Johansson, et al., 2010, Poodt, et al., 2012]. ....76

Figure 4.2 (a) Cambridge Nanotech Savannah S100 ALD reactor with a flat lid consists of precursor cylinders, precursor manifold, carrier gas delivery manifold, chamber, outlet manifold and a vacuum pump (not shown in the figure); (b) S100 equipped with dome lid for batch ALD; (c) vertical multi-wafer batch ALD setup with 27 silicon wafer samples; and

(d) horizontal multi-wafer batch ALD setup with 27 silicon wafer samples.....80

Figure 4.3 3D computational domains in the numerical model are based on S100 ALD reactor with the dome lid: (a) vertical multi-wafer arrangement; and (b) horizontal multi-wafer arrangement.....82

Figure 4.4  $\text{Al}_2\text{O}_3$  film growth rate in  $\text{\AA}/\text{cycle}$  for vertical and horizontal multi-wafer arrangements obtained from both experiments and simulations. The 18 wafers are labeled in three directions using A, B, C for X direction, b, c for Y direction, and 1, 2, 3 for Z direction. ....85

Figure 4.5 Numerical velocity contour plots and mass fluxes normal to the wafer (B-b-2) surface during TMA pulsing process: (a) and (b) velocity contour plots for vertical and horizontal arrangement at 0.015 s, respectively; (c) and (d) mass flux normal to the wafer surface for vertical and horizontal arrangement, respectively. ....87

Figure 4.6 Transient normal velocity at (a) B-b-2 wafer, and (b) the space between B-b-2 and B-c-2 in TMA pulsing process for the vertical arrangement.....88

Figure 4.7 Averaged  $\text{Al}_2\text{O}_3$  film growth rates for the three directions from both experimental and numerical investigations: (a) averaged GPCs of the wafers in Y, Z direction; (b) averaged GPCs of the wafers in X, Z direction; and (c) averaged GPCs of the wafers in X, Y direction. ....89

Figure 4.8 Correlations of precursor concentration, surface species coverage, methane generation and bulk material deposition rate in the transient pulsing processes by vertical multi-wafer ALD simulation: (a) TMA pulse; and (b) water pulse. Data are extracted from the center wafer (B-b-2) for both TMA and water pulses. The pulsing times are doubled from experiments in order to observe the entire pulsing processes. ....91

Figure 4.9 Correlations of precursor concentration, surface species coverage, and bulk material deposition rate in the transient pulsing processes by vertical multi-wafer ALD simulation for the 6 wafers located on the middle layer: (a) and (b) TMA pulse for the 6 wafers; (c) and (d) water pulse for the 6 wafers. Data are extracted from the middle wafers (layer 2 in Z direction), A (B, C)-b (c)-2, for both TMA and water pulses. The pulsing times are doubled from experiments in order to observe the entire pulsing processes. ....93

Figure 4.10 Correlations of precursor concentration, surface species coverage, and bulk material deposition rate in the transient pulsing processes by vertical multi-wafer ALD simulation for the six wafers located on the middle row: (a) and (b) TMA pulse; (c) and (d) water pulse. Data are extracted from the middle wafers (row B in X direction), B-b (c)-1 (2, 3) for both TMA and water pulses. ....95

Figure 5.1 (a) stack-type multi-wafer batch ALD reactor [Granneman, et al., 2007]; (b) in-line spatial ALD reactor [Johansson, et al., 2010, Poodt, et al., 2012]; and (c) rotary spatial ALD reactor. .... 100

Figure 5.2 3D computational domain of in-line spatial ALD reactor: (a) fluid domain in the two precursor dosing cylinders, one separating gas injecting cylinder, two exhaust cylinders, and the gap spaces between each arrangement, dimension scale in meters, and (b) center slice of the 3D domain, A, B, C and D are the probing points for the flow or chemical deposition analysis. .... 105

Figure 5.3 The effects of gap size on precursor intermixing with ideal pumping condition (0.22 torr) and 200°C deposition temperature: (a) TMA and water concentration in mol/m<sup>3</sup> at water side (position B) with gap size 1, 1.5, and 2 mm, and (b) at TMA side (position C) with gap size 1, 1.5, and 2 mm. .... 110

Figure 5.4 Comparison of relative intermixing ratios for position B (water side) and C (TMA side) with different gap sizes, and the relative intermixing ratios is defined as the concentration ratio of the foreign gas to the home gas. .... 112

Figure 5.5 The effects of relative pumping pressure (0, 0.05, to 0.1 torr) on the precursor intermixing with gap size and wafer temperature fixed at 1.5 mm and 200°C: (a) TMA and water concentration in mol/m<sup>3</sup> at water side (position B), and (b) at TMA side (position C). The simulation time is 0.04 s with 1.5 mm gap size. .... 113

Figure 5.6 The effects of wafer temperature (150°C, 200°C and 250°C) on the precursor intermixing with gap size and pumping pressure fixed at 1.5 mm and 0.22 torr: (a) TMA and water concentration in mol/m<sup>3</sup> at position B (water side), and (b) at position C (TMA side). The simulation time is 0.04 s with 1.5 mm gap size. .... 115

Figure 5.7 Growth per cycle of bulk Al<sub>2</sub>O<sub>3</sub> thin films with different deposition temperatures, 150°C, 200°C and 250°C with 1.5 mm gap size and the ideal pumping condition (0.22 torr).117

Figure 5.8 Growth per cycle of bulk Al <sub>2</sub> O <sub>3</sub> thin films with different gap sizes 1, 1.5 and 2 mm with ideal pumping condition (0.22 torr) and 200°C wafer temperature. ....	119
Figure 5.9 Growth per cycle of bulk Al <sub>2</sub> O <sub>3</sub> thin films with different relative pumping pressure (to the base pressure, 0.22 torr) 0, 0.05 and 0.1 torr with 1.5 mm gap size and 200°C wafer temperature. ....	120
Figure 5.10 Slice contours of transient flow and deposition process in the in-line spatial ALD reactor at 0.005, 0.015, 0.025, and 0.035 s for 1 mm gap size, 0.22 torr pumping pressure, and 250°C wafer temperature. ....	121
Figure 6.1 Experimental ALD system with residual gas analyzer (RGA) to characterize the methane emissions. ....	135
Figure 6.2 Contour plots of gaseous species distributions and the bulk species deposition rates (a) 0.02 s at the end of TMA pulse and (b) 10.04 s at the end of water pulse. ....	137
Figure 6.3 Gaseous species distributions during the full ALD cycle. ....	138
Figure 6.4 Surface coverage for the main surface species during the full ALD cycle. ....	139
Figure 6.5 Contour plots of surface coverage and precursor distributions in the entire ALD system (a) 0.02 s at the end of TMA pulse and (b) 10.04 s at the end of water pulse. ....	140
Figure 6.6 Correlation of the bulk species deposition rate and precursors concentration during the ALD cycle. ....	141
Figure 6.7 Effects of chamber temperatures on the process wastes and emissions (a) precursor dosage, precursor wastes and methane emissions and (b) film growth rate and precursor waste rate. ....	144
Figure 6.8 Effects of pulse time on the process wastes and emissions (a) precursor dosage, precursor wastes and methane emissions and (b) film growth rate and precursor waste rate. ....	145

Figure 6.9 Effects of purge time on the process wastes and emissions (a) precursor dosage, precursor wastes and methane emissions and (b) film growth rate and precursor waste rate.148

Figure 6.10 Effects of carrier gas flow rate on the process wastes and emissions (a) precursor dosage, precursor wastes and methane emissions and (b) film growth rate and precursor waste rate. .... 149

## LIST OF TABLES

Table.1.1 Major nano-manufacturing techniques [Sengul, et al., 2008].....	3
Table 1.2 ALD variations based on the scalability and the process conditions [Delft, et al., 2012, George, 2010, Groner, et al., 2004].....	7
Table 1.3 Common precursors developed to deposit Al <sub>2</sub> O <sub>3</sub> thin films [Puurunen, 2005]. .....	10

## ACKNOWLEDGEMENTS

In the first place, I would like to thank my advisor Prof. Chris Yuan for his tremendous support during these years in my PhD study. I will always be grateful for his insightful suggestions, constant support, invaluable guidance, and great kindness for my study and my life. I will always remember his prompt responses to my difficulties, and his encouraging words. I deeply appreciate everything he has done for me during my PhD program. His hard-working and amiable personalities set such a great model for my entire life.

I also would like to thank my doctoral committee members, Prof. Jorg C. Woehl, Prof. Junhong Chen, Prof. Benjamin Church, Prof. Woo Jin Jin Chang and Prof. Emmanuel Y.A. Wornyoh, for their insightful comments on my research during my preliminary exam and defense. They provide me very helpful advices to improve this dissertation. I specially thank Prof. Jorg C. Woehl, Prof. Benjamin Church, and Prof. Tien-Chien Jen for their kind support in my study and my life.

Additionally, I thank all my previous and current colleagues in our lab at the University of Wisconsin-Milwaukee. I really enjoy sharing those happy moments together with them. Especially, I appreciate the help from Dr. Dongsheng Guan, Dr. Xianfeng Gao, Jianyang Li, Dr. Lulu Ma, Dr. Yuanyuan Xie, Dr. Ming Qiu, Junling Xie, Dr. Bingbing Li, and Dr. Endong Wang.

Finally, I also acknowledge the financial support from the National Science Foundation (CMMI-1200940).



# CHAPTER 1 INTRODUCTION

## 1.1 Nano-manufacturing and atomic layer deposition

### 1.1.1 Nano-manufacturing technology

Nanotechnology refers to the technologies to understand and manipulate materials in the dimensions between 1 and 100 nanometers [Wang, 2009]. In nano scale, materials tend to exhibit unique characteristics which potentially imply exciting applications. For instance, in the area of energy, applications of nanotechnologies such as solid state lighting, low-power display, fuel cells, hydrogen storage, battery materials, solar power, catalysis, etc. can be foreseen in the near future [Wang, 2009]. In the domain of environment, nanotechnologies can provide new pathways towards novel sensors, emission reduction, membrane separations, coating, radioactive waste containment, etc. [Wang, 2009].

Nanotechnologies have gained extensive attentions from both academic and public in the past decades. They have shown strong potentials to revolutionize many aspects of our society. Their value has been recognized by many governments worldwide. For example, in the U.S., a national nanotechnology initiative (NNI) was established in 2001 to coordinate research and development activities among different agencies in nanotechnologies.

Nano-manufacturing technology is particularly the process of manipulation of matters to develop nanomaterials, or fabricate 2D and 3D nanoscale structures [Busnaina, et al., 2013].

Nano-manufacturing has been shown very versatile in many research and application

frontlines, such as microelectronics, energy, environmental and human health. Nano-manufacturing, which is highly interdisciplinary, implies diverse subjects such as surface science, organic chemistry, molecular biology, semiconductor physics, micro-fabrication, etc. [Puurunen, 2003].

Based on the way of manipulating materials, nano-manufacturing technologies fall into the following two main categories: top-down and bottom-up [Sengul, et al., 2008, Wang, 2009]. Top-down techniques are subtractive methods, which achieve nanoscale features through carving or grinding methods (e.g., lithography, etching, and milling). Bottom-up methods are additive which form the nano structures through nucleation or growth from gas, liquid, or solid precursors by chemical or physical processes [Sengul, et al., 2008]. Table 1 lists the major nano-manufacturing techniques [Sengul, et al., 2008].

It is widely accepted that bottom-up techniques are less waste-producing than top-down methods, although top-down nano-manufacturing is more commonly used to fabricate nanoproducts. Bottom-up techniques generate nano structures through specific physical processes or chemical reactions at the molecular level, and hence minimize unwanted waste with careful process design and optimization [Sengul, et al., 2008].

Table.1.1 Major nano-manufacturing techniques [Sengul, et al., 2008].

<b>Top-down techniques</b>	<b>Lithography</b>	Conventional lithography	• Photolithography • E-beam lithography
		Next-generation lithography	• Immersion lithography • Lithography with lower wavelengths • Lithography with particles
		Nanoimprint lithography	• Step-and-flash imprint lithography
		Soft lithography	-
	<b>Etching</b>	Wet etching	-
		Dry etching	• Reactive ion etching • Plasma etching • Sputtering
	<b>Electrospinning</b>	-	-
	<b>Milling</b>	Mechanical milling	-
		Cryomilling	-
		Mechanochemical bonding	-
<b>Bottom-up techniques</b>	<b>Vapor-phase techniques</b>	Deposition techniques	• Vapor phase epitaxy • Chemical vapor deposition • Molecular beam epitaxy • <b>Atomic layer deposition</b> • Pulsed laser deposition • Sputtering • Evaporation.
		Nanoparticle/nanostructured materials synthesis techniques	• Evaporation • Laser ablation • Flame synthesis
	<b>Liquid-phase techniques</b>	Precipitation	-
		Sol-gel	-
		Solvothermal synthesis	-
		Sonochemical synthesis	-
		Microwave irradiation	-
		Reverse micelle	-
	<b>Self-assembly techniques</b>	Electrostatic self-assembly	-
		Self assembled monolayers	-
		Langmuir-Blodgett formation	-

### 1.1.2 Atomic layer deposition

As a vapor-phase bottom-up nano-manufacturing method, atomic layer deposition (ALD) is operated by alternately injecting two or more chemical precursors into a chamber to enable material deposition on substrates layer by layer. The one-by-one injections of precursors result in sequential saturated surface reactions, which make the ALD process highly self-limited. As a result, the resultant films are perfectly uniform in surface geometry which makes ALD ideal to fabricate conformal nano-films on complex structures. Due to depositions in atomic level, the film thickness can be accurately controlled in Ångstrom or monolayer level with high precisions [George, 2010]. The method is capable to deposit ultra-thin films in a few Ångstrom. ALD has been adopted extensively in silicon microelectronics and thin-film device industries, and is on rapid expansion to more industrial applications [George, 2010].

A typical ALD reaction cycle with two precursors is illustrated schematically in Figure 1.1. The main idea of ALD is to separate the half surface reactions in time or space. As shown in Figure 1.1, before the ALD cycles, substrates are cleaned, and ALD equipment is prepared. Then, the growth of thin film by ALD involves repeating the following four steps [Puurunen, 2005]:

- (1) Pulse the reactant A into ALD chamber to enable the first half surface reaction;
- (2) Purge the un-reacted reactants and the gaseous by-products out of the reactor;
- (3) Pulse the second reactant B into the chamber to enable the second half surface reaction;

(4) Purge the un-reacted reactants and the gaseous by-products out of the reactor.

Through the four steps, a certain amount of material is added to the substrate surface in each reaction cycle until desired thickness is achieved.

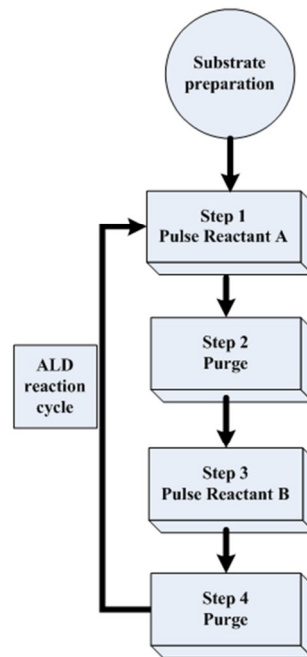


Figure 1.1 Schematic illustrations of ALD reaction cycles.

ALD has many variations based on the scalability and the process conditions. Table 1.2 presents the various types of ALD [Delft, et al., 2012]. As shown in Figure 2.2, based on scalability, single-wafer ALD is the most common variation, which can only process a single wafer at one time. Multi-wafer batch ALD reactors allow multiple substrates to be processed simultaneously. Spatial ALD is totally based on a brand new concept [Johansson, et al., 2010]. In conventional ALD, the precursors are dosed one by one, and separated in time by a purging step, but with the spatial idea, the ALD surface reactions are separated in

space other than in time, and precursors are dosed simultaneously and continuously with the relative movement of wafer belt [Poedt, et al., 2013]. Roll-to-roll ALD is capable to process flexible substrate continuously. Based on the process conditions, there are thermal ALD, plasma-enhanced ALD (PEALD), etc. as presented in Table 1.2 [George, 2010, Groner, et al., 2004].

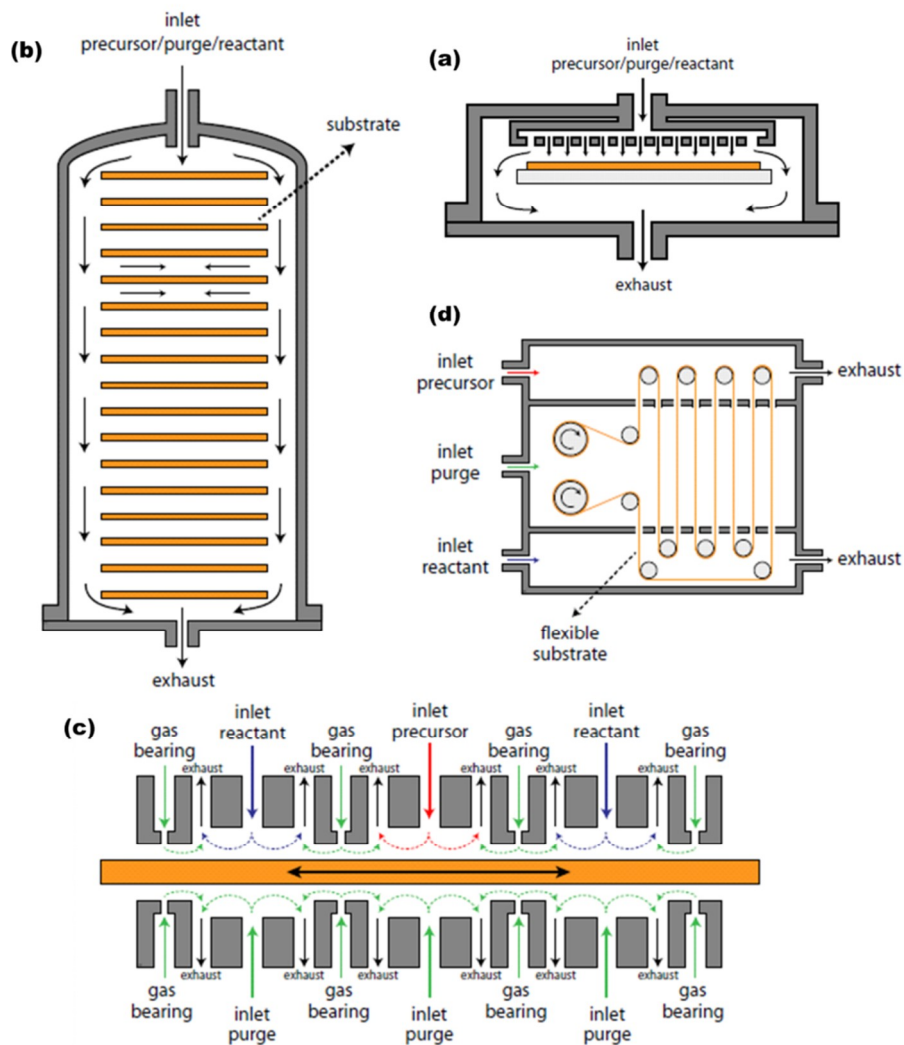


Figure 1.2 Various ALD reactors: (a) Showerhead type single-wafer ALD reactor; (b) Multi-wafer batch ALD reactor; (c) In-line spatial ALD reactor; (d) Roll-to-roll ALD reactor [Delft, et al., 2012].

A typical thermal ALD reactor mainly consists of a precursor delivery unit, a carrier gas

delivery unit, a heating unit, a pumping unit and a chamber. For instance, the Cambridge Nanotech Savannah S100 ALD system shown in Figure 1.3 consists of precursor cylinders, precursor manifold, carrier gas manifold, chamber, outlet pipe and a vacuum pump.

Table 1.2 ALD variations based on the scalability and the process conditions [Delft, et al., 2012, George, 2010, Groner, et al., 2004].

Based on scalability	Based on process conditions
Single-wafer ALD	Thermal ALD
Multi-wafer batch ALD	Plasma-enhanced ALD
Spatial ALD	Low temperature ALD
Roll-to-roll ALD	Low-pressure ALD
-	Atmospheric pressure ALD

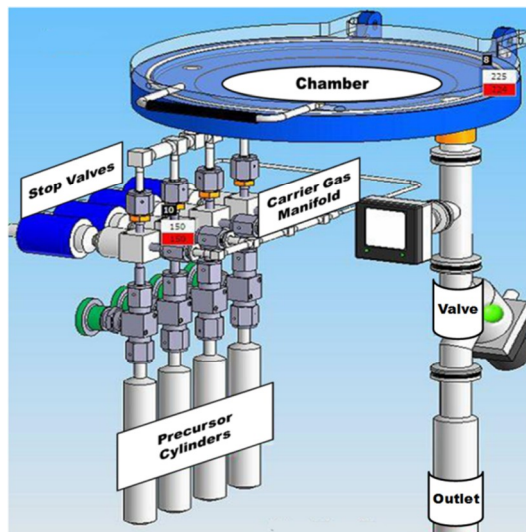


Figure 1.3 Cambridge Nanotech Savannah S100 ALD system consists of precursor cylinders, precursor manifold, carrier gas manifold, chamber, outlet manifold and a vacuum pump (not shown in the figure).

Precursors stored in separate cylinders are injected into chamber by their own vapor

pressure at room temperature (25°C), and pulsing (in milliseconds) is controlled by ALD stop valves. Nitrogen or argon is the carrier gas flowing through the system continuously during all the operations. A vacuum pump is connected with outlet pipe to maintain the low vacuum pressure ( $\sim 10^{-1}$  torr) in chamber. The reactor chamber (with 150mm inner diameter) is designed for deposition of films on substrates with diameter up to 100mm and can be heated from 100°C to 250°C depending on specific deposition conditions.

### 1.1.3 ALD of $\text{Al}_2\text{O}_3$

$\text{Al}_2\text{O}_3$  thin film is one of most widely studied materials fabricated by ALD due to its high dielectric constant, high thermal stability and good adhesion to many surfaces [Li, et al., 2007]. These unique properties make  $\text{Al}_2\text{O}_3$  an excellent material in the silicon microelectronics and thin-film device industries.  $\text{Al}_2\text{O}_3$  thin film is extensively used as the high-k gate dielectric in transistors. For instance, Intel deposited  $\text{Al}_2\text{O}_3$  thin film as the gate oxide in its 45 nm transistor as shown in Figure 1.4 [Mistry, et al., 2007].

Other applications of  $\text{Al}_2\text{O}_3$  thin film include dynamic random access memory (DRAM) with trench structures. ALD allows trench features to be scaled to less than 100 nm and provides an effective means of depositing thin films like the trench capacitor dielectric material [Ko and Lee, 2007]. Figure 1.5 presents the cross-sectional SEM image of an 300 nm  $\text{Al}_2\text{O}_3$  ALD thin film on a Si wafer with a trench structure for DRAM application [George, 2010]. Besides,  $\text{Al}_2\text{O}_3$  thin film is also promising to replace  $\text{Si}_2\text{O}_3$  as the gate



dielectric material for metal oxide semiconductor field effect transistors (MOSFETs) [Li, et al., 2007].

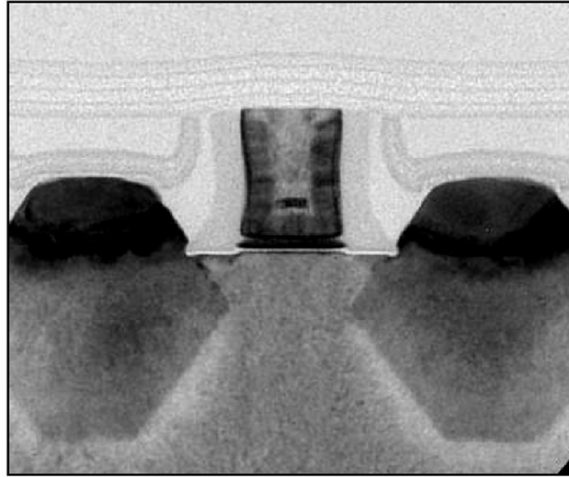


Figure 1.4 TEM of high-k dielectric with metal gate for 45 nm PMOS transistor with ALD-deposited high-k Al<sub>2</sub>O<sub>3</sub> dielectric [Mistry, et al., 2007].

Al<sub>2</sub>O<sub>3</sub> film was firstly reported to be deposited by ALD using trimethylaluminum [Al(CH<sub>3</sub>)<sub>3</sub>, or Al(Me)<sub>3</sub>, or TMA] as the metal provider, and H<sub>2</sub>O as the oxidant [Higashi and Fleming, 1989, Soto and Tysoe, 1991], and then more precursors such as TMA and ozone were developed [Goldstein, et al., 2008, Li, et al., 2007, McDonnell, et al., 2012, Mousa, et al., 2014]. Table 1.3 lists the common precursors used to deposit Al<sub>2</sub>O<sub>3</sub> thin films [Puurunen, 2005].

For the Al<sub>2</sub>O<sub>3</sub> ALD deposition process using TMA and water as the precursors, the overall reaction with the two reactants is as following,



In ALD, the reaction is separated into two half surface reactions as following,



where \*items denote surface species.

Table 1.3 Common precursors developed to deposit  $\text{Al}_2\text{O}_3$  thin films [Puurunen, 2005].

Metal provider	Oxidant
$\text{AlCl}_3$	$\text{H}_2\text{O}$
$\text{AlCl}_3$	$\text{O}_2$
$\text{AlBr}_3$	$\text{H}_2\text{O}$
$\text{Al}(\text{CH}_3)_3$	$\text{H}_2\text{O}$
$\text{Al}(\text{CH}_3)_3$	$\text{H}_2\text{O}_2$
$\text{Al}(\text{CH}_3)_3$	$\text{O}_3$
$\text{Al}(\text{CH}_3)_3$	$\text{N}_2\text{O}$
$\text{Al}(\text{CH}_3)_3$	$\text{NO}_2$
$\text{Al}(\text{CH}_3)_3$	$\text{N}_2\text{O}_4$

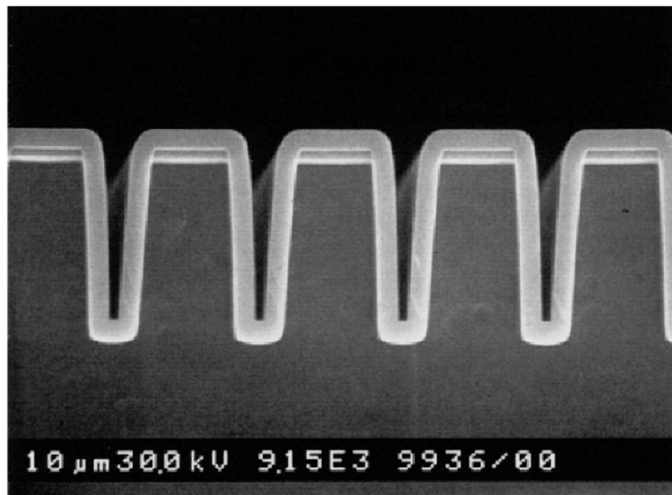


Figure 1.5 Cross-sectional SEM image of an 300 nm  $\text{Al}_2\text{O}_3$  ALD thin film on a Si wafer with a trench structure for DRAM application [George, 2010].

In the first half reaction,  $\text{Al}(\text{CH}_3)_3$  is absorbed on the surface by substituting the surface H

atom with  $\text{CH}_3$  and releasing a  $\text{CH}_4$ , and in the second half, the methyl ligand is substituted by hydroxyl ligand. As a result, oxygen atom is deposited on the surface. At this point, the surface is coated with one layer of aluminum and oxygen atoms forming the  $\text{Al}_2\text{O}_3$  film materials. Multilayer depositions are achieved by repeating the two half reactions.

## **1.2 ALD applications**

### 1.2.1 Microelectronics applications

Currently, the majority of ALD applications are in the field of microelectronics. Large amount of materials have been fabricated by ALD for the microelectronics applications. To be specific, high-k dielectric materials such as  $\text{Al}_2\text{O}_3$ ,  $\text{HfO}_2$ ,  $\text{ZrO}_2$  are prepared by ALD for gate oxides to substitute  $\text{SiO}_2$  gate dielectric in metal-oxide-semiconductor field-effect transistors (MOSFETs) [George, 2010, Groner, et al., 2004, Mistry, et al., 2007, Scarel, et al., 2003]. Also, ALD is an excellent method to fabricate transition-metal nitrides such as  $\text{TiN}$ ,  $\text{WN}$ ,  $\text{TaN}$ ,  $\text{MoN}$ ,  $\text{HfN}$ , and  $\text{TaCN}$ , which are used as metal barriers and gate metals in modern Cu-based chips. In such Cu-based chips, in order to avoid diffusion of Cu into the surrounding materials, and prevent Cu contamination by elements diffusing from the insulators, the metal barriers are required pure, dense, conformal, and thin, and they must have good adhesion towards metals and insulators [Anacleto, et al., 2010, Klaus, et al., 2000, Lee, 2005]. These requirements are perfectly fulfilled by the superiorities of ALD.

Another important microelectronic application of ALD is in Dynamic Random-Access

Memory (DRAM) capacitors. Major efforts are being put into reducing the size of the DRAM capacitor which will effectively allow for greater memory density. In order to reduce the capacitor size without affecting the capacitance, different cell orientations are being used. Some of these include stacked or trench capacitors. The huge challenge for trench capacitors is fabrication due to the small size in trench and high aspect ratio. ALD allows trench features to be scaled to below 100 nm, and provides an effective means of depositing perfectly uniform thin films on the trench structures [Ko and Lee, 2007] [Ritala, et al., 1999].

Noble metals are excellent conductors, but they are more notable for the catalytic effects in many oxidation, reduction, and hydrogenation reactions to accelerate or control the rate of reactions [Hamalainen, et al., 2014]. Noble metals and their oxides including ruthenium, osmium, rhodium, iridium, palladium, platinum, silver, and gold can be prepared by ALD through thermal or plasma-enhanced ALD process [Hamalainen, et al., 2014]. Also, ALD is capable to fabricate magnetic materials such as magnetic nanopowders and nanofibers. They have multiple applications in electrochemical biosensing, bioseparation and detection of cells and proteins, separation of catalyst materials, controlled drug and gene delivery and release, and magnetic resonance imaging (MRI) [Santala, et al., 2009].

### 1.2.2 Energy conversion and storage applications

Besides microelectronics, ALD applications are expanded to the energy conversion and

storage applications such as fuel cells, solar cells, and batteries, e.g., lithium-ion batteries (LIBs). In fuel cells, ALD is mostly used to fabricate platinum electrocatalysts on carbon nanotubes (CNTs). For instance, since ALD is a dry process and it has some advantages for deposition of Pt nanoparticle catalysts on CNTs with especially high surface area in proton exchange membrane fuel cells (PEMFCs) [Hsueh, et al., 2012, Shu, et al., 2012]. In solid oxide fuel cells (SOFCs), ALD is used to coat catalysts with Pt surface to improve the fuel cell performance [Shim, et al., 2010].

ALD applications in solar cells include fabrication of nanostructured electrodes or charge transporters (e.g., ZnO, TiO<sub>2</sub>, Fe<sub>2</sub>O<sub>3</sub>, Cu<sub>2</sub>O), forming heterojunction (e.g., AlZnO,TiO<sub>2</sub>), inert surface passivation of trap states (e.g., Al<sub>2</sub>O<sub>3</sub>), and preparation of catalytic noble metals (e.g., Pt, Pd, Ru, Ir) [Niu, et al., 2015]. In lithium-ion batteries, ALD is particularly used to fabricate novel battery components with nanostructured anode materials to improve the electrodes performance of batteries [Meng, et al., 2012]. Also, ALD is used for surface modification of battery electrodes, since LIBs currently suffer from capacity fading during electrochemical cycling and potential safety risks caused by unwanted side reactions occurring during charge-discharge cycles, causing electrolyte decomposition, solid electrolyte interphase (SEI) formation, and active material dissolution [Meng, et al., 2012]. Other application of ALD can also be found in Lithium–Sulfur (Li–S) rechargeable batteries for modification of graphene-sulfur composite with an ALD-Al<sub>2</sub>O<sub>3</sub> coating [Yu, et al., 2014].

### 1.2.3 Medical and environmental health applications

The newly developed application for ALD is in medical and biological area. ALD is adopted to create flexible sensors, bioelectronic device, implantable device, drug delivery device, tissue engineering scaffold and bioassay device, modify nanoporous membranes, and create thin biocompatible coatings [Skoog, et al., 2013]. For example, atomic layer deposition is used to functionalize nanoporous alumina membranes coated with platinum for medical and environmental health applications [Narayan, et al., 2010].

## **1.3 Research motivation and objectives**

### 1.3.1 ALD sustainability limitations

With more than three decades' development, ALD has been developed into one of the well-established nano-manufacturing techniques to fabricate ultra-thin films of various materials with excellent uniformity and conformity in surface geometry [George, 2010, Haukka, 2007]. Since the materials are deposited layer by layer in atomic level, ALD is an excellent technology to precisely control the thickness of deposited thin films [Pan, et al., 2015, Pan, et al., 2014]. However, this intrinsic superiority comes along with one of the serious sustainability limitations, especially in the industrial level ALD applications: low material deposition efficiency or throughput [Haukka, 2007]. Because of the one-atomic-layer growth pattern per cycle in ALD process, the low deposition efficiency

remains an inherent challenge for the ALD community, especially for the single-wafer reactors [Delft, et al., 2012]. The conventional single-wafer ALD, for instance, can only achieve 1.1~1.3 Å/cycle growth rate, that is a few nm per min for deposition of Al<sub>2</sub>O<sub>3</sub> [Poodt, et al., 2013]. This growth rate is considered too low [Delft, et al., 2012].

Another serious sustainability issue is the negative environmental impacts of the technique. Taking Al<sub>2</sub>O<sub>3</sub> ALD for example, one of the reactants, TMA, is extremely flammable and highly toxic. It can cause severe skin burns and eye damage even when one is exposed to TMA for a very short time [Yuan and Dornfeld, 2010]. The un-reacted TMA may be purged out of the system as one of the emissions that poses a high risk to the public health and environment. The by-product, methane, is one of the major greenhouse gases [Yuan and Dornfeld, 2010]. Nano-particles can also be formed in the space of chamber in the ALD system due to gaseous reactions between the two precursors and other complex side reactions. Although these emissions are very little, even negligible in a few hundred reaction cycles of ALD process in lab level, in the context that the large amount of dielectric material is demanded in the semiconductor industry globally, the amount of emissions is extremely high [Yuan and Dornfeld, 2010]. With the great application potential of ALD technology in the semiconductor and a number of other industrial sectors, the sustainability performance of ALD technology becomes astonishingly critical and needs to be improved prior to its large scale industrial applications.

Since the deposition efficiency and material utilization are influenced by a lot of factors, such as process temperature, process pressure, precursor dosage, purge time, etc., choice of process parameters, e.g., pulsing time, purging time, temperature, have a crucial influence on the overall ALD deposition process [Lankhorst, et al., 2007]. Therefore, detailed information on the transient physical and chemical processes must be obtained before the improvement and optimization of the process.

### 1.3.2 Previous research of ALD process

Previous ALD research is mainly focused on development of new precursors, but details on ALD physical and chemical process are not yet well understood [Puurunen, 2005]. In general, studies of ALD process have been developing into two domains: experimental and numerical.

Experimental researchers improve the deposited films by adjusting experimental conditions, e.g., process pressure, temperature, dosage, etc.[Cheng, et al., 2005, King, et al., 2011, Krajewski, et al., 2009, Kukli, et al., 2002, Rai, et al., 2012, Wind and George, 2010]. Li et al. studied the effects of process temperature and pressure on  $\text{Al}_2\text{O}_3$  film properties by characterizing the film thickness uniformity, impurity incorporation, and the step coverage in high aspect ratio features [Li, et al., 2007]. Mousa et al. presented a study of the effects of temperature and gas velocity on film growth in  $\text{Al}_2\text{O}_3$  and ZnO ALD, respectively [Mousa, et al., 2012]. Sammelselg et al. studied the growth unevenness and film compositions in



ALD of TiO<sub>2</sub> thin films [Sammelseg, et al., 1998]. Influence of growth temperature on properties of zirconium dioxide films by ALD was examined by Kukli et al. [Kukli, et al., 2002]. Similar research was conducted by Scarel et al. to study the electric properties of ZrO<sub>2</sub> films [Scarel, et al., 2003].

Confined by technical, economic and time feasibilities in experimental implementations, ALD experiments are always facing a “black box” without knowing enough details about the transient process, and thus they only focus on the “output”, such as growth rate, film properties. Consequently, they are not able to shed adequate light on the detailed information of ALD process. With progresses in computing technologies, many researchers are devoted to studying physical interactions and chemical kinetics of ALD by numerical approaches.

ALD process is in essence a multi-scale process, which not only involves atomic bonds formations, species chemisorptions and nano-film deposition (in molecular scale), but also includes material interactions and energy transport in macroscopic scale (in chamber scale). In molecular scale, most numerical investigations adopt the first principle methods, such as the density function theory (DFT) method to explore surface reaction mechanisms and chemical reaction pathways [Afshar and Cadien, 2013]. In the paper of Delabie et al., ALD of Al<sub>2</sub>O<sub>3</sub> using TMA and water was studied using DFT to investigate reaction pathways and possible mechanisms for growth inhibition in ALD cycles [Delabie, et al., 2012]. The

atomic-scale structure of alumina film by ALD was also studied by Elliott et al. using the DFT method [Elliott and Greer, 2004]. Besides DFT, Puurunen derived a mathematical model to describe the growth rate in ALD [Puurunen, 2003]. In the cited research, “ligand exchange” and “dissociation or association” were proposed as two types of chemisorption mechanisms [Puurunen, 2003]. The above atomic-level models revealed certain microscopic details of the surface reaction mechanisms and chemical kinetics, but few of them considered the material and energy transfer processes in ALD.

On the other hand, some researchers took the macroscopic transport processes into consideration using methods such as Monte Carlo method, molecular dynamics and Lattice Boltzmann method. Gilmer et al. applied the Monte Carlo models to simulate film deposition in atomic scale [Gilmer, et al., 2000]. Kinetic Monte Carlo methods were proposed in the cited work to investigate ALD process of  $\text{HfO}_2$  and  $\text{Al}_2\text{O}_3$ , respectively [Dkhissi, et al., 2008, Mazaleyrat, et al., 2005]. Hu et al. used molecular dynamics model to study the structure of  $\text{Al}_2\text{O}_3$  film in the aspects of surface composition, roughness and growth rate [Hu, et al., 2009]. Similar method was adopted by Gou et al. to simulate surface interactions on silicon wafer in ALD [Gou, et al., 2008]. Lattice Boltzmann method is a relatively new but rapidly developing mesoscopic approach, which uses the lattice schemes to solve the Boltzmann equation [Pan, et al., 2014]. He et al. firstly applied the Lattice Boltzmann method to simulate diffusion-convection processes with surface chemical reactions on solid surfaces [He, et al., 2000]. Lately, we extended the method and used it in

simulating the gas flow in ALD which is also presented in Chapter 2 [Pan, et al., 2014].

Due to multiple scales both in space and time, ALD simulation in chamber scale still remains challenging. In this field, Adomaitis developed numerical models to describe the ballistic transport of chemical precursor species in ALD process [Adomaitis, 2011]. Holmqvist et al. claimed a mechanistic model of continuous flow reactors [Holmqvist, et al., 2012, Holmqvist, et al., 2013]. By continuum-based models in the cited research, gas-phase fluid dynamics, mass transport, and heterogeneous gas-surface reaction mechanisms were analyzed numerically. We recently constructed a similar mechanistic model with detailed chemical kinetics to study alumina ALD process [Xie, et al., 2015]. In a paper published by Adomaitis, a multiscale model of ALD was developed by coupling the lattice Monte Carlo method with a continuum approach of precursor transport [Adomaitis, 2010].

These chamber-scale models can fundamentally describe the ALD process together with the chemical kinetics in a larger picture. However, most of them lack detailed surface reaction mechanisms and numerical results are not well correlated with the experimental observations. Without these detailed information, the process improvements and optimizations cannot be convincing.

### 1.3.3 Research objective and outline

The main research objective of this dissertation is to model the ALD process mathematically,

and study the transient process of ALD in detail to find the influential factors on the two main critical sustainability issues: low throughput, and negative environmental impacts, through both numerical and experimental approaches.

In particular, the gas fluid dynamics of the carrier gas (nitrogen) flow is studied numerically by introducing and comparing two LBM models in Chapter 2. To account for the surface deposition process, the strong-coupled physical and chemical processes of ALD are recovered numerically by Finite Volume Method (FVM) in Chapter 3. The 3D transient numerical model adopts surface reaction kinetics and mechanisms based on the atomic-level calculations [Delabie, et al., 2012, Puurunen, 2003] to study the surface deposition process. The numerical model developed for ALD is validated by experiments investigating the growth rate under different deposition conditions. Then, the experimentally-validated numerical model is used for in-depth investigation of two types of batch and spatial ALD process for throughput improvement. In Chapter 4, a multi-wafer batch ALD with vertical and horizontal wafer arrangements is studied to investigate the influences of wafer layout on the deposition process with both experimental and numerical approaches. An in-line spatial ALD is studied numerically in Chapter 5 to investigate three geometry and process factors, gap size, temperature, and pressure on the precursor intermixing and chemical deposition process. In Chapter 6, the reactive model is improved with detailed ALD surface reaction mechanisms based on DFT calculations regarding the  $\text{Al}_2\text{O}_3$  ALD reactions, and the effects of the four process parameters of temperature, pulse and purge time as well as the

carrier gas flow rate on material deposition, process wastes and emissions are explored and characterized. Important conclusions of the studies in this dissertation are summarized, and recommendations for future study are presented in Chapter 7.

#### **1.4 Summary and conclusions**

ALD is an approved nano-scale thin films fabrication technique with remarkable uniformity and conformity in surface geometry. Since the materials are deposited layer by layer in atomic level, ALD is an excellent technology to precisely control the thickness of deposited thin films. ALD plays a great role in microelectronics to fabricate ultra-thin films used in transistors, memory devices, electrodes, etc. It is on a rapid expansion to fields such as energy conversion, energy storage, medical devices and health and environmental applications. However, ALD has several critical sustainability limitations: low throughput and negative environment impacts such as gaseous emissions, nano-wastes, which pose high risk to the public health and the environment in the context of strong industrial demand of thin film materials by ALD globally. This dissertation presents numerical and experimental studies of the ALD process to investigate the transient physical and chemical ALD process in detail to improve the technique in the aspect of sustainability.

## CHAPTER 2 NUMERICAL SIMULATIONS OF ALD FLUID DYNAMICS BY LATTICE BOLTZMANN METHOD

### 2.1 Introduction

ALD process is a complex system which involves not only the chemisorptions and surface reaction processes in microscopic scale but also the gas flow, precursor transport, and heat transfer in larger scales. In the macroscopic scale, flow and precursor transport in an ALD reactor can be described by the continuum-based Navier–Stokes equations [Lankhorst, et al., 2007], but they are not able to take the molecule nature of gas flow into account when it comes to the surface deposition in smaller scale. Due to the intrinsic philosophy of recovering the macroscopic physical phenomena from the microscopic perspective, the mesoscopic methods such as LBM and direct simulation Monte Carlo method are promising in the ALD simulation.

In fact, the direct simulation Monte Carlo methods have been used to simulate the transition regime flows and rarefied gas flows in Chemical Vapor Deposition (CVD) [Adomaitis, 2010, Coronell and Jensen, 1992, Coronell and Jensen, 1994]. Other attempts of ALD simulation also includes solving the Boltzmann equation directly [Gobbert, et al., 2002], developing analytical models of mass transport and kinetic description of the surface reactions [Ylilammi, 1995] [Yanguas-Gil and Elam, 2012].

In this chapter, the Lattice Boltzmann Method (LBM) through a comparative study of two

LBM models is introduced to study the carrier gas fluid dynamics in ALD reactor. Numerical models of gas flow are constructed and implemented in two-dimensional geometry based on Lattice Bhatnagar-Gross-Krook (LBGK)-D2Q9 model and Two-Relaxation-Time (TRT) model. Both incompressible and compressible scenarios are simulated and the two models are compared in the aspects of flow features, stability and efficiency.

## **2.2 Computational fluid dynamics (CFD) for ALD**

In computational fluid dynamics (CFD), a number of models are available for different scales and applications [Raabe, 2004]. As shown in Figure 2.1, in atomic scale, the Molecular Dynamics Method is a microscopic approach by determining the motion of atoms and molecules, and numerically solving the Newton's equations of motion for a system of interacting particles [Raabe, 2004]. In the conventional continuum scale, with the conservation laws of mass, momentum and energy in a fluid domain, macroscopic properties such as velocity, pressure, temperature, etc. are achieved by solving the partial differential equations (PDEs) numerically. This approach is widely adopted in commercial CFD solver packages, such as Fluent, Comsol, etc. and applied in large scale system modeling.

Between the microscopic and macroscopic approaches, pseudo-particle, or mesoscopic methods, are derived from the molecular dynamics method by coarse graining to reduce the

complexity of the target system. In the pseudo-particle method group, off-lattice approaches such as Dissipative Particle Dynamics method, Direct Simulation Monte Carlo method simulate the fluid mechanics by pseudo-particles which move continuously in space [Aarik, et al., 2006, Li, et al., 2007, Mousa, et al., 2012]. In lattice-based pseudo-particle models such as Lattice Gas Cellular Automata (LGCA) and Lattice Boltzmann Method (LBM), pseudo-particles travel along a fixed lattice in the domain.

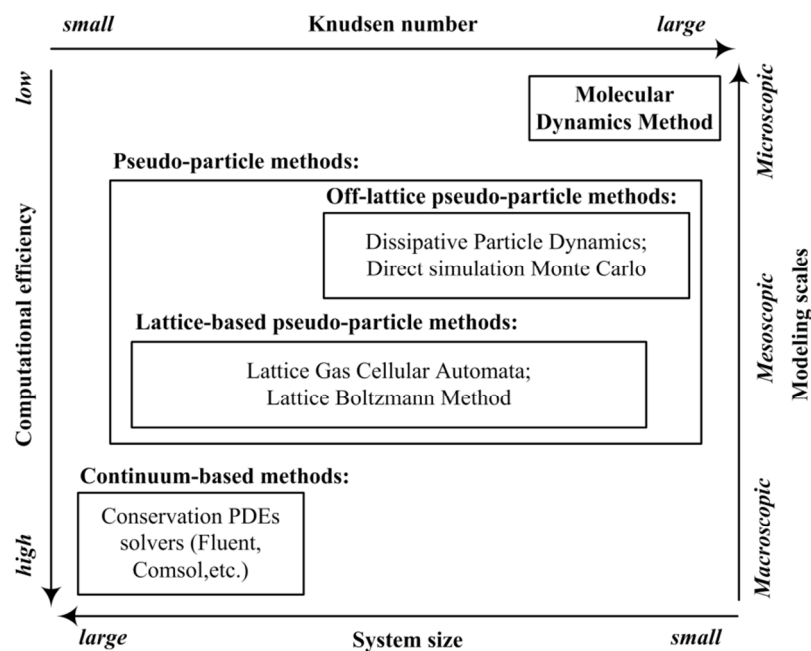


Figure 2.1 Comparisons of CFD models and their preferred application range [Raabe, 2004].

As illustrated in Figure 2.1, the Molecular Dynamics Method fits for large Knudsen number system in microscopic scale but it is computation-intensive due to the high system complexity. The continuum-based macroscopic approaches are preferred for larger-scale systems with smaller Knudsen number, since it presumes the fluid domain as a continuum. The pseudo-particle methods are devised to overcome the deficiencies of both microscopic and macroscopic methods. They simplify the fluid system, and hence improve the



computational efficiency. They have been tested effective for various applications from larger-size systems to larger Knudsen-number flows.

Dissipative Particle Dynamics method and Direct Simulation Monte Carlo are off-lattice pseudo-particle methods in conjunction with Newtonian dynamics [Aarik, et al., 2006, Li, et al., 2007, Mousa, et al., 2012]. However, the exact Newtonian dynamics are not explicitly taken into account in the lattice-based pseudo-particle methods like Lattice Boltzmann Method [Raabe, 2004]. LBM employs sets of particle velocity distribution functions instead of single pseudo-particles as used in direct simulation Monte Carlo method. Therefore, LBM gains more system simplicity and requires lower memory use and has higher processing speed. Lattice-based pseudo-particle methods are superior to the off-lattice pseudo-particle methods in both aspects of computational efficiency and application range.

LBM is rooted on the classical kinetic theory of gases to study flow properties. It dates back to the late 1980s and adopts the idea of Lattice Gas Cellular Automata (LGCA) to imitate the gas flow phenomena in streaming and collision processes. LBM has advantages over other CFD methods especially when it is used to simulate multiphase flows, multi-component flows and flows in complex geometries, due to its relatively simple but effective schemes to treat the boundary conditions [Li, et al., 2012, Martys and Chen, 1996, Martys and Douglas, 2001]. Without complying with the continuity hypothesis, LBM, in essence, is promising to model the rarefied gas flow with large Knudsen number range,

which the macroscopic methods fail [Sbragaglia and Succi, 2005, Shokouhmand and Isfahani, 2011].

### 2.3 Lattice Boltzmann Method

LBM is rooted on the Boltzmann Transport Equation, a fundamental equation in the kinetic theory developed by Ludwig Boltzmann in 1872 [Mohamad, 2011]. The equation takes the form as,

$$\frac{\partial f(\mathbf{r}, \mathbf{v}, t)}{\partial t} + \mathbf{v} \times \frac{\partial f(\mathbf{r}, \mathbf{v}, t)}{\partial \mathbf{r}} + \frac{\mathbf{F}}{m} \times \frac{\partial f(\mathbf{r}, \mathbf{v}, t)}{\partial \mathbf{v}} = W \quad (2-1)$$

where  $f(\mathbf{r}, \mathbf{v}, t)$  is the probability density function which stands for the probability of appearance of a particle in position  $\mathbf{r}$ , with velocity  $\mathbf{v}$ , at time  $t$ .  $\mathbf{F}$  is the external force acting on the particles of mass  $m$ .  $W$  is called collision item, which is a function of  $f(\mathbf{r}, \mathbf{v}, t)$ .

With the “molecular chaos assumption” proposed by Boltzmann himself, which only considers the 2-body collisions in the particle interactions, the collision item is an integro-differential form which makes it complicated to solve the Boltzmann Transport Equation analytically [Mohamad, 2011].

The Lattice Boltzmann Method is achieved numerically by discretization of the Boltzmann Transport Equation in space and time dimensions as well as velocity space along specific directions [Raabe, 2004]. The solution domain is divided into lattices. At each lattice node,

the probability density functions are calculated after collisions and then move along specified directions to the neighboring nodes. Numerous models have been constructed for the various applications in LBM [Li, et al., 2012, Martys and Chen, 1996, Martys and Douglas, 2001] [Sbragaglia and Succi, 2005, Shokouhmand and Isfahani, 2011]. In this chapter we report the two most popular schemes, LBGK-D2Q9 and MRT.

### 2.3.1 The LBGK-D2Q9 model

To approximate the collision item with simpler operator without introducing significant error, in 1954 Bhatnagar, Gross and Krook (BGK) proposed a model for the collision item as [Mohamad, 2011],

$$W = w(f^{EQ} - f) = \frac{1}{t}(f^{EQ} - f) \quad (2-2)$$

where  $w = 1/t$  is called collision frequency (relaxation factor), and  $t$  is relaxation time;  $f^{EQ}$  is local equilibrium distribution function, which is the Maxwell–Boltzmann distribution function [Mohamad, 2011].

The number of streaming directions depends on lattice arrangements, which are denoted as  $D_mQ_n$ .  $m$  represents the number of dimensions,  $n$  is the number of possible streaming directions. Most common arrangement in two dimensions is D2Q9. For D2Q9, the local equilibrium distribution function is calculated as,

$$f_k^{EQ} = w_k \left[ 1 + \frac{\mathbf{c}_k \cdot \mathbf{u}}{c_s^2} + \frac{1}{2} \left( \frac{\mathbf{c}_k \cdot \mathbf{u}}{c_s^2} \right)^2 - \frac{1}{2} \frac{u^2}{c_s^2} \right], \quad k = 0, 1, 2, \dots, 8 \quad (2-3)$$

where  $\rho$  is the density;  $\mathbf{c}_k$  is the particle velocity vector at direction  $k$ ;  $\mathbf{u}$  is the flow velocity vector;  $c_s$  is the lattice speed of sound,  $c_s = 1/\sqrt{3}$ ;  $w_k$  are weighting factors,

$$w_k = \begin{cases} 4/9 & k = 0; \\ 1/9 & k = 1, 2, \dots, 4; \\ 1/36 & k = 5, 6, \dots, 8. \end{cases} \quad (2-4)$$

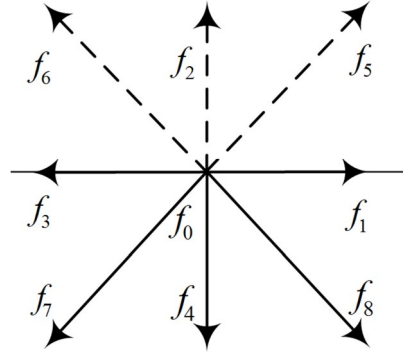


Figure 2.2 The D2Q9 lattice arrangement in LBM.

The Lattice BGK (LBGK) model is based on the BGK approximation [Eq.(2-2)]. It is also called Single Relaxation Time (SRT) model since only one relaxation time factor is used. More sophisticated models such as Multiple-Relaxation-Time (MRT), Two-Relaxation-Time (TRT), Entropy LBM models based on the LBGK model are also proposed to improve the LBM scheme, especially the computational stability [d'Humieres, et al., 2002, Lallemand and Luo, 2000, Luo, et al., 2011].

By Finite Difference approximations to the derivative items, the Boltzmann Transport Equation of BGK approximation without external forces becomes,

$$f_k(\mathbf{r} + \mathbf{c}_k \mathbf{Dt}, t + \mathbf{Dt}) = f_k(\mathbf{r}, t) + \frac{\mathbf{Dt}}{\tau} [f_k^{EQ}(\mathbf{r}, t) - f_k(\mathbf{r}, t)] \quad (2-5)$$

Equation (2-5) is called Lattice Boltzmann Equation (LBE). The Navier–Stokes equations for incompressible flow can be recovered from LBE at its low Mach number limit [Guo, et al., 2000, Regulski and Szumbarski, 2012]. To model a flow by LBM, the Reynolds number is conserved,

$$\text{Re} = \frac{UL}{\nu} = \frac{u_{\text{lattice}}N}{a} \quad (2-6)$$

where  $U$  and  $L$  are characteristic velocity and characteristic length in macro-scale;  $\nu$  is the kinetic viscosity of the fluid;  $u_{\text{lattice}}$  and  $N$  are the corresponding lattice characteristic velocity and number of lattices;  $a$  is the lattice viscosity, which has a correlation with the relaxation factor  $w$  as,  $a = (2 - w) / 6w$ .

The numerical error in LBM is in order of  $Ma^2$  [Mohamad, 2011]. Mach number is calculated as,  $Ma = (w - 0.5)\text{Re} / \sqrt{3}N$ . To minimize the numerical error, lattice number  $N$  and relaxation frequency  $w$  should be designated properly to ensure a sufficiently small Mach number. The pressure  $p$  in LBM is related to the density  $\rho$  as,  $p = c_s^2 \rho$ .

### 2.3.2 The MRT and TRT models

Although LBGK models are popular for their simplicity, the LBGK models suffer from deficiency of the instability with high Reynolds number [Chai, et al., 2011, Chai, et al., 2006, Lallemand and Luo, 2000, Luo, et al., 2011]. In this respect, Multiple-Relaxation-Time (MRT) models are developed to improve the LBGK scheme by

taking account of the kinetic theory [Lallemand and Luo, 2000, Luo, et al., 2011]. Numerical studies show that the MRT model performs better in stability to simulate lid-driven flow and other simple flows [Lallemand and Luo, 2000, Luo, et al., 2011]. In MRT modeling, collision item is treated differently. The general LBE is,

$$f(\mathbf{r} + \mathbf{c}_k \mathbf{D}t, t + \mathbf{D}t) - f(\mathbf{r}, t) = W \quad (2-7)$$

where for D2Q9 lattice arrangement,  $f$  is a nine-dimensional vector;  $W$  is a nine-dimensional collision vector, which is constructed as,

$$W = \mathbf{M} \times \mathbf{T} \times [\mathbf{m}^{EQ} - \mathbf{m}] \quad (2-8)$$

where  $\mathbf{M}$  is a 9-by-9 transformation matrix;  $\mathbf{T}$  is a non-negative diagonal relaxation matrix which contains 9 relaxation time factors in the diagonal positions;  $\mathbf{m}$ , a nine-dimensional vector, represents the 9 velocity modes (or moments) in the 9 streaming directions;  $\mathbf{m}^{EQ}$  is the equilibrium vector for the 9 modes.

The main principle of MRT lies in the kinetic theory, which states that the physical process in fluids, e.g. the viscous transport, involves interactions among different modes, and these modes are directly related to the moments [Lallemand and Luo, 2000].

In MRT, the 9 modes (moments) are defined as:  $r$ , density mode;  $e$ , energy mode;  $e$ , energy square mode;  $j_x$ , x-direction momentum mode;  $q_x$ , x-direction energy flux mode;  $j_y$ , y-direction momentum mode;  $q_y$ , y-direction energy flux;  $p_{xx}$ , normal stress tensor;  $p_{xy}$ , shear stress tensor. In LBM, if the fluid is assumed as athermal [Lallemand and Luo,

2000], only density and linear momentum modes are conserved and are not changed by the collision process.

The transformation matrix,  $M$ , is comprised by these 9 modes,

$$\begin{aligned}
 M = \begin{pmatrix}
 \rho & e & \varepsilon & j_x & q_x & j_y & q_y & p_{xx} & p_{xy} \\
 \rho & e & \varepsilon & j_x & q_x & j_y & q_y & p_{xx} & p_{xy} \\
 \rho & e & \varepsilon & j_x & q_x & j_y & q_y & p_{xx} & p_{xy} \\
 \rho & e & \varepsilon & j_x & q_x & j_y & q_y & p_{xx} & p_{xy} \\
 \rho & e & \varepsilon & j_x & q_x & j_y & q_y & p_{xx} & p_{xy} \\
 \rho & e & \varepsilon & j_x & q_x & j_y & q_y & p_{xx} & p_{xy} \\
 \rho & e & \varepsilon & j_x & q_x & j_y & q_y & p_{xx} & p_{xy} \\
 \rho & e & \varepsilon & j_x & q_x & j_y & q_y & p_{xx} & p_{xy} \\
 \rho & e & \varepsilon & j_x & q_x & j_y & q_y & p_{xx} & p_{xy}
 \end{pmatrix} = \begin{pmatrix}
 1 & 1 & 1 & 1 & 1 & 1 & 1 & 1 & 1 \\
 -4 & -1 & -1 & -1 & -1 & 2 & 2 & 2 & 2 \\
 4 & -2 & -2 & -2 & -2 & 1 & 1 & 1 & 1 \\
 0 & 1 & 0 & -1 & 0 & 1 & -1 & -1 & 1 \\
 0 & -2 & 0 & 2 & 0 & 1 & -1 & -1 & 1 \\
 0 & 0 & 1 & 0 & -1 & 1 & 1 & -1 & 1 \\
 0 & 0 & -2 & 0 & 2 & 1 & 1 & -1 & -1 \\
 0 & 1 & -1 & 1 & -1 & 0 & 0 & 0 & 0 \\
 0 & 0 & 0 & 0 & 0 & 1 & -1 & 1 & -1
 \end{pmatrix} \quad (2-9)
 \end{aligned}$$

The equilibrium vectors  $m^{EQ}$  is constructed by [Lallemand and Luo, 2000],

$$m^{EQ} = (\rho, e^{EQ}, \varepsilon^{EQ}, j_x, q_x^{EQ}, j_y, q_y^{EQ}, p_{xx}^{EQ}, p_{xy}^{EQ})^T \quad (2-10)$$

The diagonal relaxation matrix is  $T = diag(0, w_e, w_e, 0, w_q, 0, w_q, w_n, w_n)$ . Relaxation factors  $w_i$  correspond to the 9 velocity modes. Their values are in the range of  $0 \leq w_i \leq 2$ . Among these relaxation factors,  $w_n$  is the viscosity relaxation factor which is related to the shear stress tensor, thus the fluid shear viscosity  $\eta$ . The factor  $w_n$  is correlated with the lattice viscosity  $\nu$  as,  $\nu = (2 - w_n) / 6w_n = (2\tau - 1) / 6$ .

The other three relaxation factors ( $w_e, w_e, w_q$ ) are adjustable so that optimal numerical simulation results can be obtained. The SRT (LBGK) model is merely a special case of

MRT when all the three factors are set as  $w_e = w_e = w_q = w_n = 1/t$  [Lallemand and Luo, 2000]. The TRT model allows only two relaxation factors adjustable, as  $w_e = w_e = 1/t = w_n$ ,  $w_q = 8(2 - w_n) / (8 - w_n)$  [Ginzburg, 2005, Ginzburg, et al., 2008, Luo, et al., 2011]. The TRT model keeps the simplicity of LBGK models, while inheriting the benefits of the MRT model in terms of flexibility and stability [Ginzburg, 2005].

### 2.3.3 Conservation laws

By solving LBE numerically, the density functions  $f_k$  are obtained. The macroscopic parameters depicting the fluid properties are recovered from the density functions by following conservation equations. In D2Q9 scheme, by mass conservation, the flow density  $r$  is,

$$r = \sum_{k=0}^8 f_k \quad (2-11)$$

By momentum conservation, the fluid velocity  $u$  satisfies,

$$r u = \sum_{k=0}^8 c_k f_k \quad (2-12)$$

## 2.4 Numerical methods

The objective of this work is to use LBM models to simulate the flow pattern of the carrier gas (nitrogen) in ALD fabrication process. In this section, numerical models are constructed and developed based on actual ALD technical parameters and system characteristics. The



numerical simulations are implemented in two dimensions by comparing the two LBM models, as illustrated in the following.

#### 2.4.1 Two-dimensional geometry

The numerical LBM modeling is performed on the Cambridge Nanotech's Savannah S100 ALD system. The flow rate of carrier gas at the inlet is 20 sccm, and a vacuum pump is connected to the outlet. The ALD reactor is a low-vacuum system [Chun, et al., 2008], with only 0.39 Torr background pressure inside the chamber. Figure 2.3 is the numerical two-dimensional geometry of ALD vacuum reactor. The flow enters into the chamber via the inlet through the chamber. A wafer is located in the center of the chamber to be deposited.

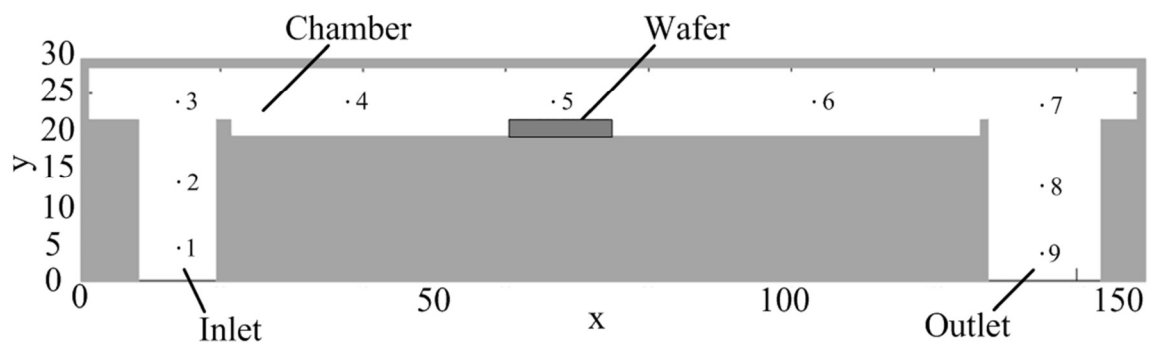


Figure 2.3 Two-dimensional geometry of ALD vacuum reactor based on Cambridge Nanotech's Savannah S100 ALD system. Grey area denotes the solid wall nodes, and white is the fluid domain. Chamber is connected with the inlet pipe and outlet pipe. Wafer is located in the center of the chamber.

## 2.4.2 Boundary conditions and initial conditions

### (1) Walls: bounce-back boundary condition

The grey nodes in Figure 2.3 represent solid walls in the ALD geometry, which are modeled by the bounce-back scheme. The main principle is that, every particle bounces back into fluid when they come across the liquid-solid interface. As illustrated in Figure 2.4, for the density functions at the interface which travel into the solid ( $f_1, f_5, f_8$ ), their values can be obtained by the streaming step from the previous nodes, while for  $f_3, f_6, f_7$ , which come from the solid side, their values are unknown. By applying the bounce-back scheme, they can be obtained as,  $f_3 = f_1; f_6 = f_8; f_7 = f_5$ .

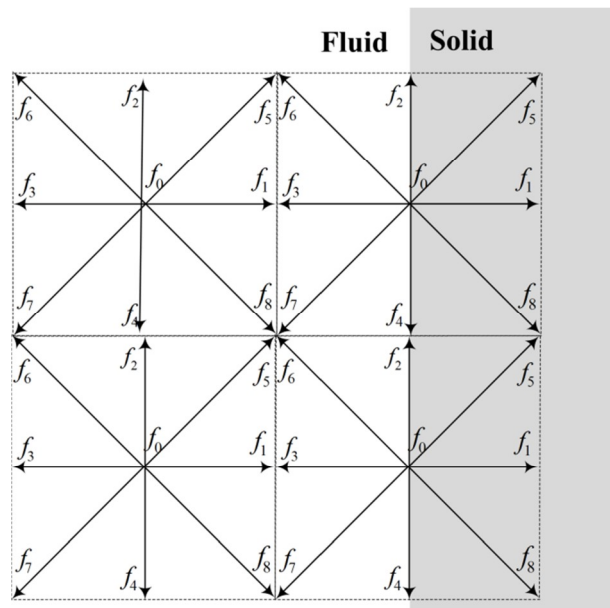


Figure 2.4 Scheme of bounce-back boundary condition for the solid wall nodes (grey) in the domain.

### (2) Inlet: velocity boundary condition

For velocity boundary condition, Zou and He proposed a method to calculate the unknown distribution functions based on the known distribution functions, specified macro values and

the conservation relations [Zou and He, 1997]. In our simulation, velocity boundary condition is applied at inlet, where the velocity vectors are specified at the boundary of ALD reactor. Shown in Figure 2.5, for all the lattice nodes along the inlet boundary line, density functions  $f_1, f_3, f_4, f_7, f_8$  in solid lines are known from the streaming step of neighboring nodes, while the functions  $f_2, f_5, f_6$  in dash lines are unknown.

Applying the conservation laws (mass and momentum) at the boundary nodes yields,

$$r = f_0 + f_1 + f_2 + f_3 + f_4 + f_5 + f_6 + f_7 + f_8 \quad (2-13)$$

$$r u = 0 = f_1 + f_5 + f_8 - (f_3 + f_6 + f_7) \quad (2-14)$$

$$r v = f_2 + f_5 + f_6 - (f_4 + f_8 + f_7) \quad (2-15)$$

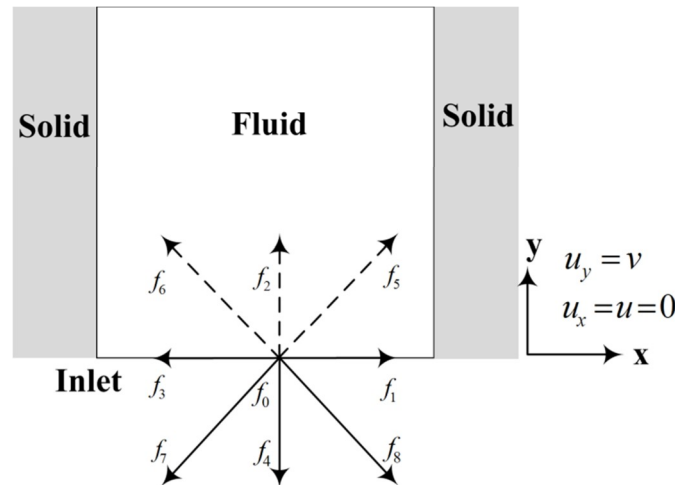


Figure 2.5 Scheme of velocity boundary condition which is applied at the inlet. Velocities in both x and y directions are specified.

In addition, proposed by Zou and He, the bounce-back rule is imposed for the non-equilibrium part of the particle distribution which is normal to the inlet boundary

[Gobbert, et al., 2002]. Then,

$$f_2 - f_2^{EQ} = f_4 - f_4^{EQ} \quad (2-16)$$

where, the local equilibrium functions are calculated as Eq.(2-3).

Solving the above 4 equations for the four unknown quantities, we get,

$$r = \frac{1}{1-\nu} [f_0 + f_1 + f_3 + 2(f_4 + f_7 + f_8)] \quad (2-17)$$

$$f_2 = f_4 + \frac{2}{3} r \nu \quad (2-18)$$

$$f_5 = f_7 - \frac{1}{2}(f_1 - f_3) + \frac{1}{6} r \nu \quad (2-19)$$

$$f_6 = f_8 + \frac{1}{2}(f_1 - f_3) + \frac{1}{6} r \nu \quad (2-20)$$

### (3) Outlet: pressure boundary condition

Pressure boundary condition is employed at the outlet. If the pressure (density) is specified at the boundary, the unknown quantities can be obtained by solving similar system of equations as Eq.[(2-13)-(2-16)] [Zhang and Kwok, 2006].

### (4) Initial conditions

The initial density for the fluid domain is set as unity, while the initial velocities are 0. If the condition of incompressible flow is considered, the initial outlet density is set the same as the initial density. In real cases, the pressure (density) is slightly decreased even in the incompressible flow, and then the compressibility should be taken into account. In this work, both of the two conditions are simulated.

### 2.4.3 Numerical parameters setup

LBM simulates the real flow with the same Re number calculated using Eq.(2-6). If the fluid has a higher viscosity, the friction effect is dominant and thus it takes more relaxation time for the particles to get back to the equilibrium status after collisions. Therefore, in a flow with a high Re number, the particles collide rapidly, so that it is inclined to form turbulences. In numerical methods, these phenomena may cause the computational instability.

From Eq.(2-6), lattice velocity and lattice number are both positively related to the lattice viscosity, while they have a negative relationship with each other. In LBM simulation, as long as the Re number is conserved, all these three parameters can be adjusted in certain ranges. To minimize the simulation error, a small lattice velocity value should be guaranteed to ensure a sufficiently small Ma number. The number of lattice determines the scale of numerical calculations, which are directly related to the computational efficiency. A smaller lattice viscosity leads to a bigger viscosity collision factor  $w_n$  which can only be adjusted in the range of 0~2. Too high collision frequency tends to cause the computations unstable. An effective way is to determine the lattice scale, and then make sure a small lattice velocity while ensuring a small lattice viscosity based on the available computational resources. In our simulation, inlet lattice number is set at 10, and the lattice velocity is tuned with viscosity relaxation factor.

#### 2.4.4 Relation of lattice and physical values

LBM is in essence a pseudo-particle dimensionless modeling method [Al-Jahmany, et al., 2004, Regulski and Szumbarski, 2012]. The bridge connecting to the physical world is the same Re number determined by Eq.(2-6). Hence, for Newtonian fluid, the derivation of physical values from the LBM simulation result is straight forward. The physical velocity is directly from Eq.(2-6),

$$U = \frac{u_{lattice} N \eta}{a L} \quad (2-21)$$

The relation of physical time step in seconds and lattice time steps (ts) is implicit. The lattice time is identical to physical time as,

$$\frac{N}{u_{lattice}} [ts] = \frac{L}{U} [s] \quad (2-22)$$

Considering the Re number is same for both systems, Eq.(2-22) becomes,

$$\frac{N^2}{a \text{ Re}} [ts] = \frac{L^2}{\eta \text{ Re}} [s] \quad (2-23)$$

Therefore, the physical time corresponding to one lattice time step is as following,

$$1[ts] = \frac{L^2 a}{N^2 \eta} [s] \quad (2-24)$$

## 2.5 Results and discussion

### 2.5.1 Simulations of gas flow in ALD: LBGK-D2Q9 vs. TRT

In this section, the numerical simulations of carrier gas flow in ALD system using LBGK-D2Q9 and TRT are compared in details. In our simulations, we consider both conditions of incompressible and compressible flows.

#### (1) Simulations of incompressible flow

In this simulation, the ideal incompressible flow is assumed first and the ratio of chamber average density to the outlet density is set as 1:1. The viscosity relaxation factor  $w_\eta$  varies from 1.95 to 1.99. The dimensionless simulation results of LBGK-D2Q9 and TRT are presented in Figure 2.6 and Figure 2.7, respectively.

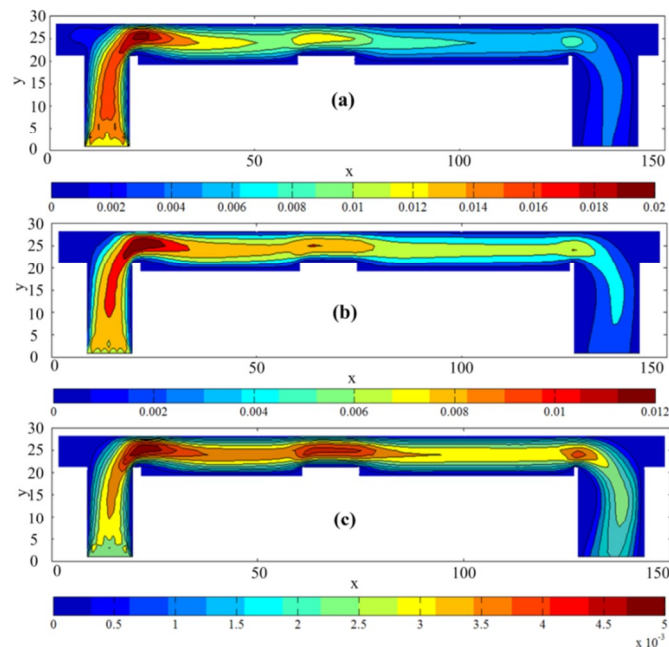


Figure 2.6 Dimensionless velocity magnitude contour plots of carrier gas in ALD for incompressible flow by D2Q9: (a) viscosity relaxation factor  $w_\eta = 1.95$ , (b)  $w_\eta = 1.97$ , (c)  $w_\eta = 1.99$ .

The two plots from D2Q9 in Figure 2.6 and TRT in Figure 2.7 with same viscosity relaxation factor are similar in the contour plots. The flows develop both in evident multiple layers as a laminar flow. Both contour plots show velocity concentrations at the corners and around the wafer area. The values of velocity magnitude are close to each other. However, D2Q9 displays unsteady flows in the inlet area as shown by the wavy contour lines. The irregular contour lines are the evidences of turbulence and numerical instability of D2Q9. The irregularity observed by D2Q9 simulations is even more severe at lower relaxation factors as shown in Figure 2.6 (a) and Figure 2.6 (b). For instance, when  $w_n = 1.95$ , the wavy contour lines are observed almost in the whole entrance area. On the contrary, TRT shows better stability with laminar flow features at the inlet.

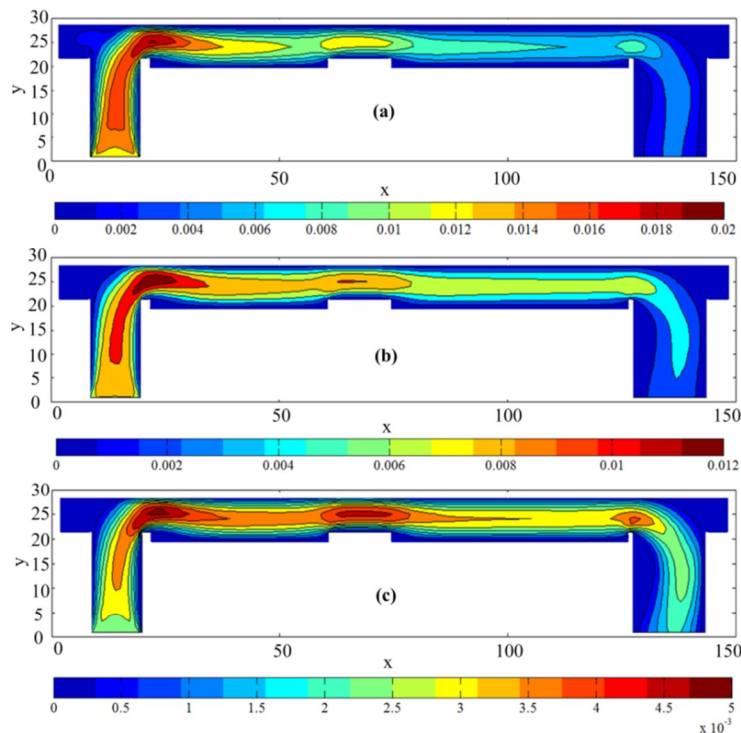


Figure 2.7 Dimensionless velocity magnitude contour plots of carrier gas in ALD for incompressible flow by TRT. (a)  $w_n = 1.95$ , (b)  $w_n = 1.97$ , (c)  $w_n = 1.99$ .



This is mainly attributed to the schemes of the two models. TRT assigns different values to the three adjustable relaxation factors, and thus the three corresponding modes are relaxed at different rates. This grants flexibility to the scheme and ability to overcome the instability. It is also observed that the flow develops more easily with a larger relaxation factor. From Section II, the lattice viscosity is related with the relaxation factor as,  $\alpha = (2 - \omega_n) / 6\omega_n = 1 / 3\omega_n - 1 / 6$ . A larger relaxation factor means a smaller viscosity, and hence the inertia effects are dominant in the flow. Figure 2.6 (c) and Figure 2.7 (c) are the cases of gas flow, which has very low viscosity.

For the computational efficiency, the curves in Figure 2.8 show that the running time for TRT to converge is nearly 20 times of D2Q9. The reason is that in each calculation cycle there are 9 modes relaxed and calculated in TRT, but only one in D2Q9. Overall, the TRT model performs better in stability than D2Q9 especially at the entrance and D2Q9 is superior to TRT in the aspect of computational efficiency.

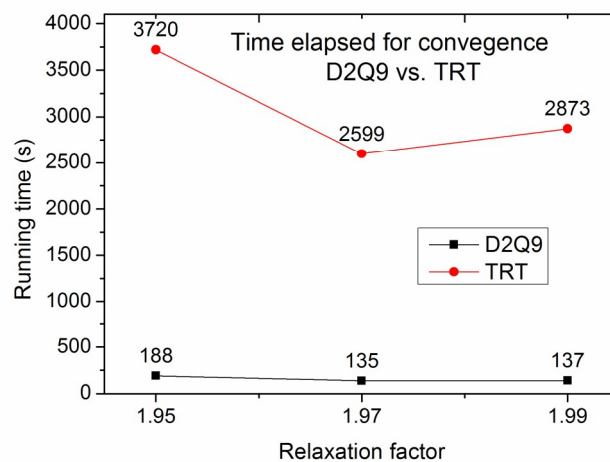


Figure 2.8 Computational efficiency: D2Q9 vs. TRT for incompressible flow simulations.

## (2) Simulations with compressibility

Actual gas flow is always not ideally incompressible, and then the compressibility must be considered with pressure or density variations in the flow domain. We set the compressible ratio as 1:0.96, and the viscosity relaxation factor  $w_n$  is changed from 1.74 to 1.89. The results are listed in Figure 2.9 and Figure 2.10.

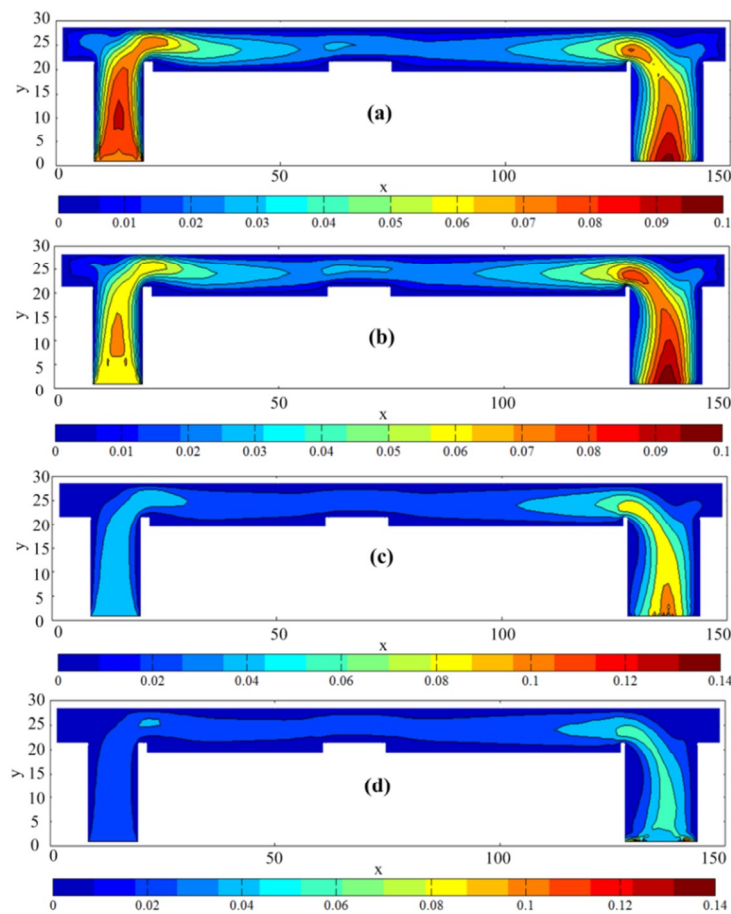


Figure 2.9 Dimensionless velocity magnitude contour plots of carrier gas in ALD with compressible ratio (1:0.96) by D2Q9. From (a), (b), (c) to (d):  $w_n = 1.74, 1.79, 1.84, 1.89$ .

When the viscosity relaxation factor is small, e.g., 1.74 and 1.79, D2Q9 and TRT yield similar velocity contour plots as presented in Figure 2.8 (a), (b), and Figure 2.9 (a), (b).

Both contour plots at same relaxation level display similar features of laminar flow. By

increasing the relaxation factor, the results from both D2Q9 and TRT start to deteriorate, but D2Q9 shows much more rapid deterioration than TRT as shown in Figure 2.8 (c) and Figure 2.9 (c) in which both models use  $w_\eta = 1.84$ . From the simulation, it is found that both simulations tend to diverge at  $w_\eta = 1.89$ . The results reveal that D2Q9 is less stable than TRT if the compressibility of flow is considered.

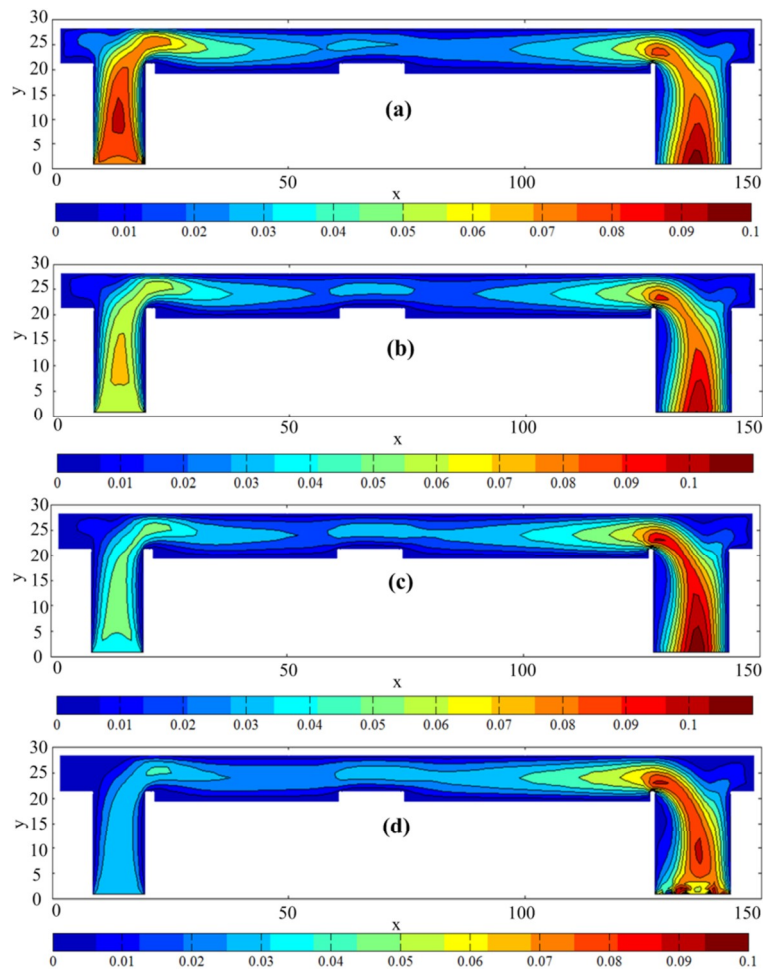


Figure 2.10 Dimensionless velocity magnitude contour plots of carrier gas in ALD with compressible ratio (1:0.96) by TRT. From (a), (b), (c) to (d): relaxation factor  $w_\eta = 1.74, 1.79, 1.84, 1.89$ .

With smaller relaxation factors, the flow has a higher viscosity, such as high viscous liquids,

the effect of inlet velocity boundary condition is dominant as show in figure (a) and (b) in both Figure 2.9 and Figure 2.10. For gas flow with lower viscosity (higher relaxation factor), the influence of compressibility is significant. TRT model shows more resistant to the deterioration caused by flow compressibility than D2Q9 model. In all, TRT shows better computational stability and reliability in both incompressible and compressible flow simulations than the D2Q9 model, though it is less advantageous in the computational efficiency.

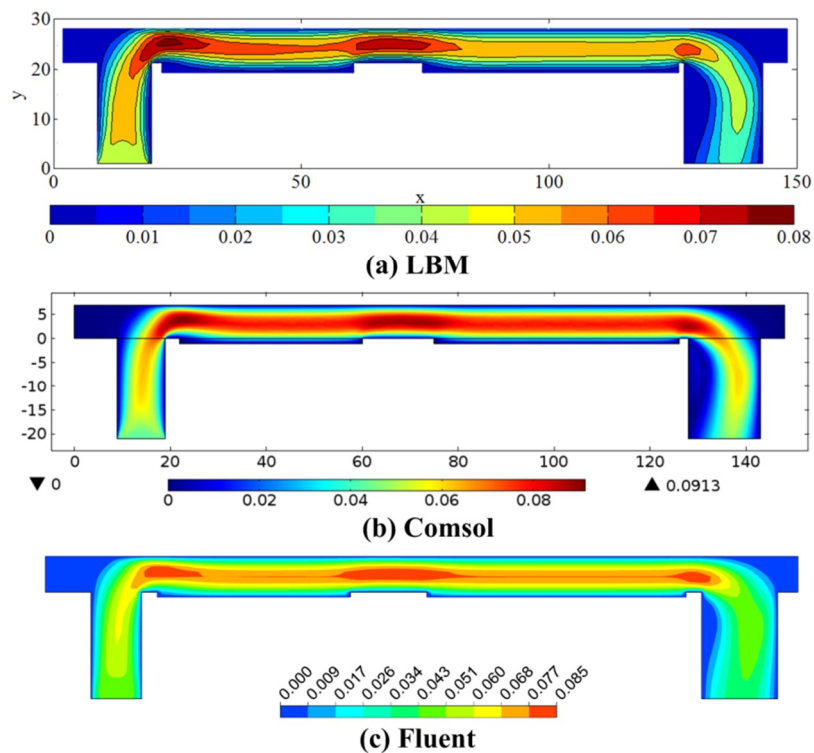


Figure 2.11 Comparison of velocity (m/s) contour plots by LBM-TRT with conventional continuum-based solver packages. (a) dimensional velocity (m/s) contour plots by LBM, (b) flow simulation result (m/s) by Comsol and Fluent, (c) flow simulation result (m/s) by Fluent.

### (3) Verification of LBM-TRT modeling results

To validate the LBM modeling results, in this section, the simulation result by LBM-TRT

model is compared with conventional continuum-based CFD solvers, Comsol and Fluent.

Figure 2.11 presents the modeling results from LBM, Comsol and Fluent, respectively.

Using Eq.(2-21) and Eq.(2-24), the dimensionless velocity contour plot for incompressible flow by TRT model at  $w_n = 1.99$  in Figure 2.7 (c) is converted to dimensional plot in

Figure 2.11 (a). By comparisons, it is found that LBM-TRT yields quite similar contour plot

as Comsol and Fluent. The velocity magnitude values are in the same range.

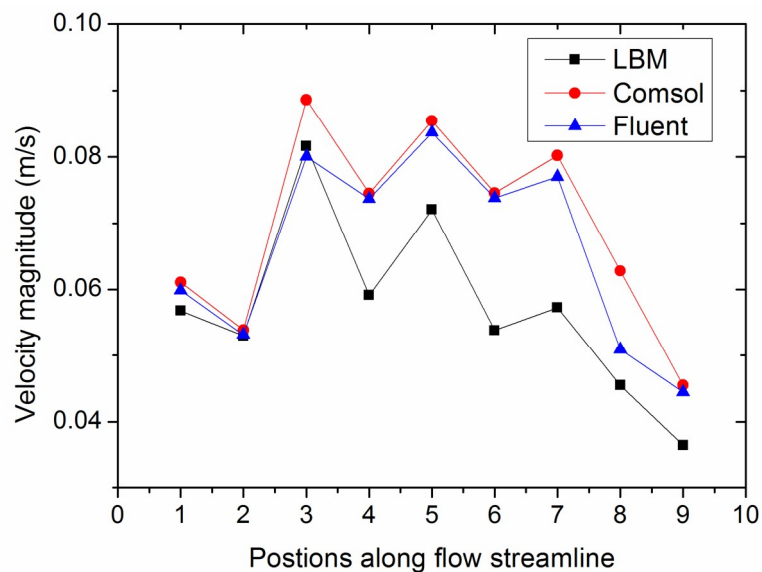


Figure 2.12 Plots of velocity variations along flow streamline by LBM, Comsol and Fluent, respectively. Position 1 and 2 are located in the inlet area, 3-7 in the chamber, 8 and 9 in the outlet field. It is shown that LBM repeats the velocity variations observed by Comsol and Fluent in the same way.

To further compare the results from the three methods, the velocity values along the flow streamline in the ALD system are achieved in Figure 2.12. As marked in Fig. 2.3, position 1 and 2 are located in the inlet area, 3-7 in the chamber, 8 and 9 in the outlet field. It is revealed that the result from LBM agrees well with the variations of velocity observed by

both Comsol and Fluent. It has been shown that LBM yields very similar results as the conventional CFD methods. LBM is verified as an effective mesoscopic method of modeling carrier gas flow in the ALD system.

### 2.5.2 ALD carrier gas flow characterization and discussion

With the velocity field obtained by TRT in Figure 2.11 (a), the carrier gas flow in the ALD vacuum reactor is recovered numerically by LBM. The flow is fully developed in the reactor and the flow pattern signifies evident laminar flow features. It is also observed that, the velocity is concentrated when the fluid domain experiences significant geometry changes, such as the inlet and outlet corners and the substrate area.

In ALD, precursors are stored in cylinders with control valves, and the precursor materials form a saturated vapor by evaporation and diffusion. The precursors are driven into the ALD system by the pressure difference inside and outside the cylinder in a very short time (~0.015s). The precursors enter into the inlet pipes first and then are delivered by the inertial carrier gas. Since the carrier gas flows continuously during ALD cycles, materials are mainly transported by the convection mechanism.

As shown in the velocity contour plot by LBM-TRT, the carrier gas flow is in a laminar steady state during the ALD procedure. The precursor molecules move together with the carrier gas owing to the convection effect and hence they transport faster in the areas where

carrier gas have larger velocities. As a result, precursors tend to be concentrated in lower-velocity areas. The precursor distribution is largely influenced by the velocity field of the carrier gas. In areas such as the corners and the substrate area presented in Figure 2.11 (a), the precursor has relatively low concentration.

Precursor materials get in contact with the substrate surface species as a result of material diffusion and the Brownian motion. The precursor materials will be absorbed and deposited more easily with more contacts. Therefore, in the areas where the effects of diffusion and random molecular motion are superior to the convection, the absorption and deposition is stronger. This can be realized by heating the ALD system to accelerate the molecular motions.

In general, a stable carrier gas flow with lower velocities will contribute to better depositions of materials on the wafer surface, especially when the convection effect is much weaker than the molecular diffusion effect. Fluctuations in the flow around the wafer area would make it more difficult for the precursor molecules to contact with the wafer surface. As shown by the simulation result in Figure 2.11 (a), high velocities and drastic changes of carrier gas flow velocity at the top of wafer area may deteriorate the deposition efficiency. Sudden geometric changes around the wafer should be avoided. The influence of flow field by wafers should also be considered.

## 2.6 Summary and conclusions

In this chapter, the carrier gas flow in ALD vacuum reactor was modeled numerically using two LBM models: LBGK-D2Q9 and TRT. Numerical modeling and simulations were implemented in 2D ALD geometry. The two models in both incompressible and compressible scenarios were compared between in the aspects of flow features, stability and efficiency.

The simulations show that, for the specific ALD reactor, TRT model generates better steady laminar flow features all over the domain with better stability and reliability than LBGK-D2Q9 model especially if the compressible effects of the gas flow are considered.

The LBM-TRT is verified with two conventional continuum-based computational fluid dynamics (CFD) solvers and it shows very good agreement with these conventional methods.

The flow in ALD is in a laminar steady state with velocity concentrated at the corners and around the wafer. Steady and evenly-distributed velocity field contribute to higher precursor concentration near the wafer, and lower velocities achieve better surface adsorption and deposition. The ALD reactor geometry needs to be considered with caution if a steady and laminar flow field around the wafer is desired for better surface deposition.



# **CHAPTER 3 A COMBINED NUMERICAL AND EXPERIMENTAL STUDY OF THE PHYSICAL AND CHEMICAL DETAILS OF $\text{Al}_2\text{O}_3$ ALD**

## **3.1 Introduction**

$\text{Al}_2\text{O}_3$  thin film is typically studied as a model ALD process due to its high dielectric constant, high thermal stability and good adhesion on various wafer surfaces. In despite of extensive applications of  $\text{Al}_2\text{O}_3$  ALD in microelectronics industries, details on the physical and chemical processes are not yet well understood. ALD experiments are not able to shed adequate light on the detailed information regarding the transient ALD process. Most of current numerical approaches lack detailed surface reaction mechanisms and their results are not well correlated with experimental observations. In this chapter, a combined experimental and numerical study on the details of flow and surface reactions in  $\text{Al}_2\text{O}_3$  ALD using TMA and water as precursors is present. Results obtained from experiments and simulations are compared and correlated.

## **3.2 Experiments**

The surface reaction process and  $\text{Al}_2\text{O}_3$  film growth rate are characterized by the Cambridge NanoTech Savannah 100 ALD system using TMA+ $\text{H}_2\text{O}$  reactions. The ALD system is shown in Figure 1.3.

In experiments,  $\text{Al}_2\text{O}_3$  thin films are deposited on substrates of crystal silicon 100 with dimensions of 10 mm by 10 mm, using 99.9% TMA as the metal provider and 99.0% distilled water as the oxidant. The wafers are prepared by firstly being immersed in 5% HF acid solution for five minutes, and rinsed in distilled water. With HF treatment, the layers of native oxide are removed [Kurhekar and Apte, 2013]. Then, the wafers are immersed in 30%  $\text{H}_2\text{O}_2$  and 70%  $\text{H}_2\text{SO}_4$  mixed acid solution for five minutes and washed by distilled water. For each experiment, five samples are placed inside the chamber, with one in the center, the other four around equilaterally. Specifically, substrate A is placed at the inlet, C at the outlet, B and D at the upper and lower positions, and E in the center of chamber.

Before depositions, each component of ALD system is heated to the prescribed temperature and the system is stabilized for 300 seconds. Pulsing time for both TMA and water vapor is 0.015 s, while purging time for both TMA and water vapor is tested with 8 s and 20 s, respectively. In ALD cycle, TMA is pulsed, and then purged in the first half cycle, and in the second half cycle, water is injected and purged. To be specific, the ALD cycle in 8 s purging experiment is TMA/Purge/Water/Purge=0.015 /8/0.015/8 s and in 20 s purging experiment, TMA/Purge/Water/Purge=0.015 s/20 /0.015/20 s. Nitrogen is flowing through the system at 20 sccm. A total of 60 cycles are deposited in the experiments. The accumulated film thickness by ALD is characterized by the UVISEL Spectroscopic Ellipsometer (HORIBA, Ltd.).

### 3.3 Mathematical modeling

ALD cycle can be decoupled into several physical and chemical procedures, such as momentum transport (material flow), convective heat transfer (system heating), mass transfer (species transport), as well as chemical reactions (surface species chemisorption). Each process is governed by corresponding PDEs which can be solved numerically on the defined domain. These PDEs are derived using the Finite Volume Method (FVM). The surface reaction kinetics and mechanisms are defined on surface sites to simulate the material deposition process.

#### 3.3.1 Fluid dynamics

The continuum-based Finite Volume Method assumes the concerned domain as a continuum.

The continuity equation conserves mass [Fox, et al., 2009, Munson, 2008],

$$\frac{\partial \rho}{\partial t} + \nabla \cdot (\rho \mathbf{V}) = S_m \quad (3-1)$$

where  $\rho$  is the density,  $\mathbf{V}$  is the velocity vector,  $S_m$  is a mass source term.

The flow in S100 ALD system was confirmed as a laminar flow as presented in Chapter 1 [Pan, et al., 2014]. The process of momentum transport within the laminar flow in the ALD chamber is governed by the momentum conservation equation [Fox, et al., 2009, Munson, 2008],

$$\frac{\partial}{\partial t} (\rho \mathbf{V}) + \nabla \cdot (\rho \mathbf{V} \mathbf{V}) = -\nabla P + \nabla \cdot \boldsymbol{\tau} + \rho \mathbf{g} + \mathbf{F} \quad (3-2)$$

where  $P$  is the static pressure;  $\mathbf{r} \cdot \mathbf{g}$  and  $\mathbf{F}$  are the gravitational body force and external body forces, respectively;  $\mathbf{t}$  is the stress tensor which is defined as [Fox, et al., 2009, Munson, 2008],

$$\mathbf{t} = \mu(\tilde{\mathbf{N}}\mathbf{V} + \tilde{\mathbf{N}}\mathbf{V}^T) - \frac{2}{3}\tilde{\mathbf{N}}\nabla\cdot\mathbf{V}\mathbf{I} \quad (3-3)$$

where  $\mu$  is the fluid dynamic viscosity,  $\mathbf{I}$  is the unit tensor, and the term  $\frac{2}{3}\tilde{\mathbf{N}}\nabla\cdot\mathbf{V}\mathbf{I}$  is the effect of volume dilation.

To model the species transport in ALD system, the convection-diffusion equation is adopted. In ALD system, the two-component gaseous mixture is concerned: (1) water vapor and nitrogen; (2) TMA vapor and nitrogen. The convection-diffusion equation for species  $i$  takes the following form [Mills, 2013],

$$\frac{\partial}{\partial t}(\rho c_i) + \tilde{\mathbf{N}}\nabla(\rho c_i\mathbf{V}) = -\tilde{\mathbf{N}}\nabla\cdot\mathbf{J}_{m,i} + R_i + S_i \quad (3-4)$$

where  $c_i$  is the local molar fraction of species  $i$ ,  $R_i$  is the net rate of production of species  $i$  by chemical reaction and  $S_i$  is the source of species  $i$ .

The diffusion flux,  $\mathbf{J}_{m,i}$ , is the mass diffusion due to the gradients of concentration and temperature. In a mixture, when concentration of one species is much lower than the major component, the dilute approximation is satisfied, and Fick's law is used to model mass diffusive flux of the dilute species [Mills, 2013]. In ALD system, although each precursor is pulsed in a very short time (e.g., 0.015 s), the amount of precursor injection is shown large in our numerical flow characterization and experimental observations. The dilute

approximation does not hold in our case, so the Maxwell-Stefan equation for full multi-component diffusion is more appropriate [Mills, 2013],

$$\mathbf{J}_{m,i}^{\mathbf{v}} = - \mathring{\mathbf{a}} \cdot \mathbf{r} \sum_{j=1}^{N-1} D_{ij} \tilde{N} c_j - D_{T,i} \frac{\tilde{N} T}{T} \quad (3-5)$$

where  $D_{ij}$  is the binary Maxwell–Stefan diffusive coefficient of species  $i$  and  $j$ ;  $N$  is the total number of species in the mixture.

### 3.3.2 Heat transfer

In ALD process, heat transfer is in forms of conduction between chamber and pipe, and convection between wall and gaseous mixture. Also, there is heat transfer by species diffusion, e.g., heat transfer because of mass diffusion caused by material concentration gradients [Bergman and Incropera, 2011, Kays, et al., 2005, Mills, 2013].

With the very small portion of radiation between chamber and gases neglected, the overall heat transfer within ALD chamber is governed by the energy equation,

$$\frac{\partial}{\partial t} (\mathbf{r} E) + \tilde{N} \mathbf{v} \cdot \nabla (\mathbf{r} E + P) = \tilde{N} \nabla \cdot [k \tilde{N} T - \mathring{\mathbf{a}} \cdot \sum_i h_i \mathbf{J}_{h,i}^{\mathbf{v}} + (\mathbf{r} \cdot \mathbf{v})] + S \quad (3-6)$$

where  $k$  is the material thermal conductivity, and  $h_i$  is the enthalpy of mixture species  $i$ ;  $\mathbf{J}_{h,i}^{\mathbf{v}}$  is the diffusion heat flux of mixture species  $i$ .  $S$  is the source term of heat which is due to chemical reaction or other heat sources. The term  $E$  is defined as [Bergman and Incropera, 2011, Kays, et al., 2005],

$$E = h - \frac{P}{\mathbf{r}} + \frac{V^2}{2} \quad (3-7)$$

In summary, precursor distribution in the ALD system is achieved by solving the species transport Eq.(3-4) with incorporation of the momentum conservation Eq.(3-2) and energy Eq.(3-6).

### 3.3.3 Chemical kinetics

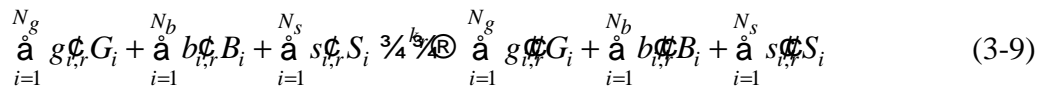
Because gas flow in the concerned ALD system is shown as laminar, a laminar finite-rate method is adopted to couple the surface reactions with species transport. In laminar finite-rate model, the effect of turbulent fluctuations is ignored and the finite reaction rates are determined by Arrhenius expressions. To model the reactions accompanying species transport in ALD chamber, the production rate of species  $i$  by chemical reactions,  $R_i$  in Eq.(3-4) is calculated through the laminar finite-rate model using Arrhenius expressions,

$$R_i = M_{w,i} \sum_{r=1}^{N_r} \hat{R}_{i,r} \quad (3-8)$$

where  $M_{w,i}$  is the molecular weight of species  $i$  and  $\hat{R}_{i,r}$  is the Arrhenius molar rate of creation or destruction of species  $i$  in reaction  $r$ .

In actual ALD system, there are two kinds of reactions involved: gaseous volumetric reaction and solid surface reaction. However, in alumina ALD, gaseous volumetric reactions happen only when the two gaseous precursors (TMA and water) coexist in ALD chamber.

The general form of the  $r$ th irreversible surface reaction in ALD chamber takes the form as,



where G, B, and S denote gaseous species, bulk (solid) species, and surface species, respectively;  $N_g$ ,  $N_b$  and  $N_s$  are the total number of the corresponding gaseous, bulk and surface species;  $g_{i,r}^{\mathcal{C}}$ ,  $b_{i,r}^{\mathcal{C}}$  and  $s_{i,r}^{\mathcal{C}}$  are the stoichiometric coefficients for each reactant species  $i$ ;  $g_{i,r}^{\mathcal{P}}$ ,  $b_{i,r}^{\mathcal{P}}$  and  $s_{i,r}^{\mathcal{P}}$  are the stoichiometric coefficients for each product species  $i$ ; the rate constant  $k_r$  is evaluated by the Arrhenius expression,

$$k_r = A_r T^{b_r} \exp\left(-\frac{E_r}{RT}\right) \quad (3-10)$$

where  $A_r$  is the pre-exponential factor;  $b_r$  is the temperature exponent;  $E_r$  is the activation energy;  $R$  is the universal gas constant.

The reaction rate of surface reaction,  $\hat{A}_r$ , represented by Eq.(3-9) is calculated as,

$$\hat{A}_r = k_{f,r} \prod_{i=1}^{N_g} [G_i]_w^{g_{i,r}^{\mathcal{C}}} \prod_{j=1}^{N_s} \theta_j^{s_{j,r}^{\mathcal{C}}} \quad (3-11)$$

where, for gaseous species,  $[ ]_w$  represents molar concentrations on wall surfaces and for surface species,  $[ ]_w$  is the surface coverage. The bulk species are not included, because reaction rate is independent of bulk species. The net molar rate of production or consumption of each species is given by,

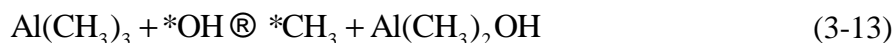
$$\begin{aligned} \hat{R}_{i,g} &= \sum_{r=1}^{N_R} (g_{i,r}^{\mathcal{P}} - g_{i,r}^{\mathcal{C}}) \hat{A}_r, i = 1, 2 \dots N_g \\ \hat{R}_{i,b} &= \sum_{r=1}^{N_R} (b_{i,r}^{\mathcal{P}} - b_{i,r}^{\mathcal{C}}) \hat{A}_r, i = 1, 2 \dots N_b \\ \hat{R}_{i,s} &= \sum_{r=1}^{N_R} (s_{i,r}^{\mathcal{P}} - s_{i,r}^{\mathcal{C}}) \hat{A}_r, i = 1, 2 \dots N_s \end{aligned} \quad (3-12)$$

where  $N_R$  represents the total number of surface reactions in ALD chamber. By substituting Eq.(3-12) into Eq.(3-8), the production (or destruction) rate of species  $i$ ,  $R_i$  in Eq.(3-4) can be

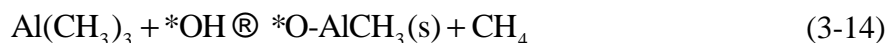
evaluated.

### 3.3.4 Surface reaction mechanisms

The surface deposition mechanisms of alumina ALD are quite complicated. In a theoretical model by Puurunen, two possible chemisorption mechanisms of ALD surface reactions were proposed: “ligand exchange” and “dissociation and association” [Puurunen, 2003, Puurunen, 2005]. Delabie et al. studied the pathways of TMA and H<sub>2</sub>O surface reactions using DFT method [Delabie, et al., 2012]. ALD surface reactions are accomplished through two possible mechanisms, namely, “ligand exchange reaction” and “chemisorption reaction” [Delabie, et al., 2012]. At the initial state, wafer surface is covered by hydroxyl group. In the ligand exchange mechanism, surface species \*OH sites are exchanged with a methyl group of TMA,



For the chemisorption reaction type, the H atom from the surface sites is transferred to one of the methyl groups of TMA, resulting in gaseous CH<sub>4</sub> and Al-O bond,

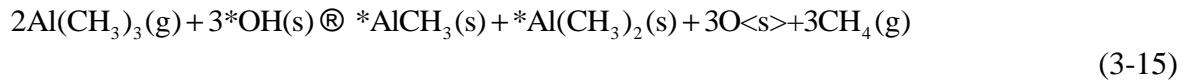


It was shown by the DFT calculations the chemisorption reactions are strongly favored kinetically over the ligand exchange reactions [Delabie, et al., 2012]. Therefore, in this study, the chemisorption reaction mechanism is adopted to study the reactions in TMA and water pulsing steps. The corresponding complete surface reactions are formulated by two

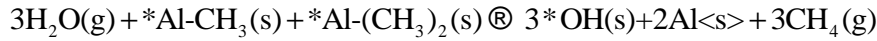


half reactions as,

TMA pulse :



Water pulse :



where  $\langle\text{s}\rangle$  denotes solid(or bulk) species; g stands for the gaseous species. The two half reactions involve two gaseous species, three surface species and two bulk species. These processes are also illustrated in Figure 3.1. The first half reaction represents TMA pulse, and the second half reaction for water pulse shown by Figure 4.3 (a) and (b), respectively.

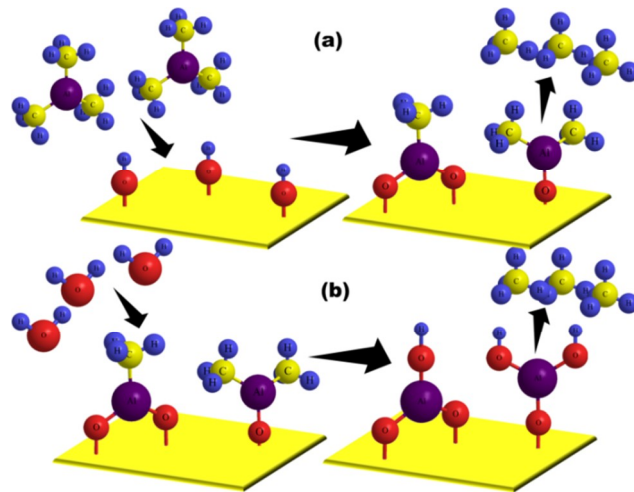


Figure 3.1 Illustrations of surface chemisorption reaction mechanism for: (a) TMA pulse; and (b) water pulse.

Besides, for the numerical model in this study, the following assumptions are presumed for the reaction mechanisms: (1) Only surface reactions are considered; (2) Both half surface reactions are irreversible considering generations of gaseous methane; (3) At the initial state, full coverage of hydroxyl group on wafer surfaces is assumed.

### 3.4 Numerical methods

A transient 3D numerical model based on the Cambridge Nanotech S100 ALD system is created and solved under the framework of ANSYS Fluent. The computational domain is shown in Figure 3.2.

The boundary condition for carrier gas nitrogen is volumetric flow rate, e.g., 20sccm. By continuous operations of vacuum pump, the background pressure of the ALD chamber is maintained at  $\sim 0.30$  torr. Precursors are stored in cylinders at room temperature, and precursors are injected into the system by their vapor pressure. In the numerical model, pressure boundary conditions are imposed on the two precursor inlets: 9.43 torr for TMA vapor, and 23.68 torr for water vapor, which are both assumed as saturated vapor pressure at  $25^{\circ}\text{C}$ . The outlet is connected with a vacuum pump and boundary condition for the outlet is pressure boundary and set as background pressure, which is also the full-load working pressure of the vacuum pump. By doing so, the steady flow field is actually presumed.

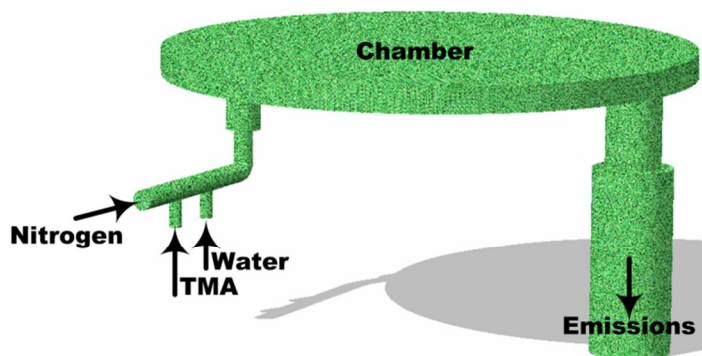


Figure 3.2 3D computational domain in the numerical model is based on S100 ALD reactor system. There are three inlets, one outlet and surface reactions are enabled only on the chamber bottom wall.

Materials are deposited on the inner surfaces of the whole ALD system in actual ALD process, but in numerical modeling, for computational simplicity, deposition reactions are only enabled on the bottom wall of chamber, where the wafers are placed. Boundary conditions for any other inner walls are assumed no-slip, no-flux of mass, but their temperature is maintained at certain levels.

Using the numerical model, a full cycle of precursor pulsing and purging process is investigated to retrieve the information regarding flow field and material distribution. Mechanisms of surface reactions formulated in Eq.(3-15) are enabled on the chamber bottom wall surface to study the surface deposition process. Numerical simulation is implemented on the 3D domain (Figure 3.2.) with a non-structural meshing scheme by the commercial solver package of ANSYS Fluent. Second-order upwind method is adopted for spatial discretization and approximation of the continuity equation, energy equation and species transport equations. By FVM with a pressure-velocity coupled scheme, the values at each domain node are calculated. Second-order implicit method is used for the time discretization and approximation. The second order numerical methods are adopted in our simulation to ensure a sufficient computational accuracy.

### **3.5 Results and discussion**

#### **3.5.1 Experiments: effects of purging time and process temperature**

Alumina thin film is deposited at four levels of chamber temperature: 100°C, 150°C, 200°C

and 250°C, each with five wafer samples. The deposited Al<sub>2</sub>O<sub>3</sub> film thickness in 60 cycles is measured using a spectroscopic ellipsometer (Horiba UVISEL model).

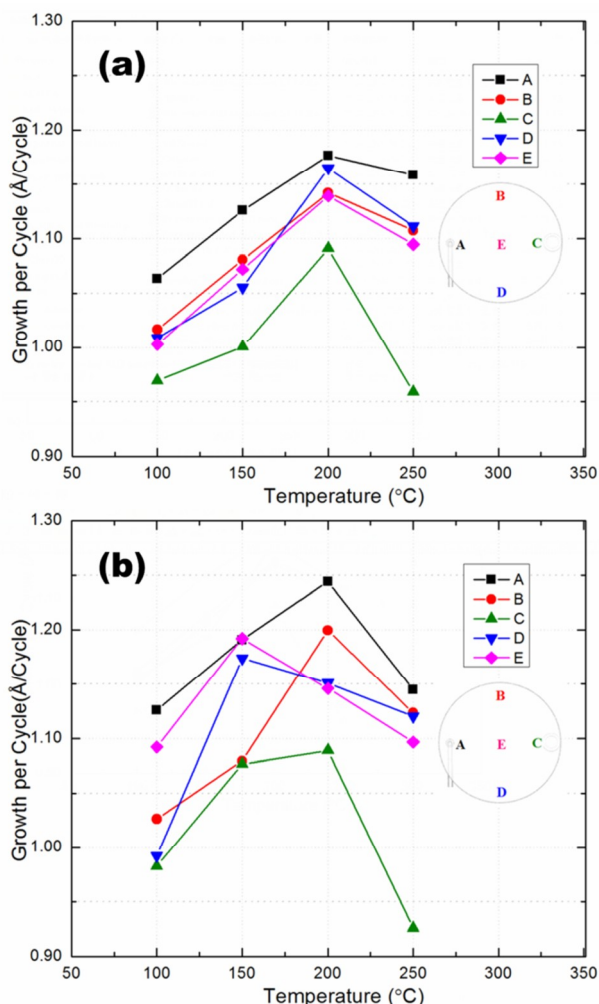


Figure 3.3 Al<sub>2</sub>O<sub>3</sub> film growth rate in Å/cycle for: (a) 8s purging experiments; (b) 20s purging experiments. Sample A is located in the inlet area, and sample C in the outlet area.

Figure 3.3 presents film growth per cycle (GPC) in Å/cycle at each temperature for 8s and 20s purging time, respectively. To be more specific, purging time is defined as the time between two precursor injections, and in one purging period, both precursor stop valves are closed, and carrier gas is flowing through the system continuously with the vacuum pump working. All the five samples have similar dependence on process temperature. Specifically,

for 8s purging experiments as indicated in Figure 3.3 (a),  $\sim 0.06 \text{ \AA}$  of GPC is increased with every  $50^\circ\text{C}$  increase of process temperature below  $200^\circ\text{C}$ . A slight decrease ( $< 0.02 \text{ \AA/cycle}$ ) for sample A is seen from  $200^\circ\text{C}$  to  $250^\circ\text{C}$ , but a larger decrease is shown from the outlet sample C. In the case of 20s purging time as presented in Figure 3.3 (b), the turning temperature for sample D and E is lowered to  $150^\circ\text{C}$  and other three samples have same turning temperature as seen in 8s purging process.

From these experimental results, film growth rate varies greatly at different chamber positions. This is due to the surface saturation conditions. Generally, as surface reactions get saturated, growth rate reaches its peak. As long as the surface saturation is not achieved, more seconds it takes in the purging step, more likely precursor molecules collide with the reactive surface species on wafer surfaces and thus more materials are deposited. To be specific, the highest growth rate for inlet sample A is  $\sim 1.18 \text{ \AA/cycle}$  at  $200^\circ\text{C}$  with 8s purging time. The reactive surface species is not saturated under this condition. With extra 12s purging time, its growth rate reaches to its peak of  $\sim 1.24 \text{ \AA/cycle}$  at same temperature in the case of 20s purging time. For the sample at outlet (sample C), surface reaction has been already saturated in 8s purging process, and hence its highest growth rate is kept at  $\sim 1.09 \text{ \AA/cycle}$  in 20s purging.

The possible reason for different turning temperature observed in sample D and E is that collision probabilities are increased by the extra time in 20s purging, and the surface

deposition process is expedited so that surface species have been saturated at lower temperature (150°C). The slightly increased peak growth rate (sample D from 1.16 Å/cycle to 1.18 Å/cycle; sample E from 1.15 Å/cycle to 1.19 Å/cycle) is also due to the longer contacting time of precursor molecules with wafer surfaces.

The overall temperature effect on GPC presented in Figure 3.3 can be well interpreted by the concept of “ALD window” [George, 2010]. At lower temperature, e.g., 100°C, the growth rate is low because the precursor would condense on the surface in liquid state or there is no sufficient thermal energy to enable and finish the surface reactions [George, 2010]. The decreased growth rate at higher temperature (250°C) is attributed to the enhanced desorption of the formed surface species at higher temperature [George, 2010].

Another interesting feature exposed by the growth rate experiments is that at each deposition temperature, materials are deposited faster on inlet wafers than outlet substrates. In 8 s purging time, growth rate of outlet sample is ~0.10 Å/cycle lower than the inlet sample. The lower deposition rate on sample C is possibly attributed to the following facts: (1) The outlet sample C is close to the vacuum pump, and the flow at outlet is much faster than at inlets. The convective effect on precursor transport is much stronger at outlet, and consequently, weaker diffusive effect decreases the deposition rate; (2) For the sample C, although all the precursor molecules gather at outlet, most precursor molecules are consumed in the surface reactions on the wafers and also the system inner surfaces. In fact,

the amount of precursor molecules reaching at outlet would be much smaller than the inlet area. Furthermore, precursors are diluted by the resultant gas product  $\text{CH}_4$ , and hence its concentration is largely decreased at the outlet. Therefore, lower GPCs are observed at outlet sample. Additional light is also shed on this observation in the aspect of unevenness of precursor distributions inside the chamber by simulations and numerical analysis in the following section.

Surface-averaged growth rates from both experimental and numerical investigations are demonstrated in Figure 3.4. Deposition rates obtained from numerical simulation are close to the experimental results. The numerical alumina growth rate is achieved by considering the resulted bulk species from both half reactions described in Eq.(3-15) and is averaged for the five sample surfaces. The numerical GPC increases from  $\sim 1.10 \text{ \AA/cycle}$  at  $100^\circ\text{C}$  to  $\sim 1.22 \text{ \AA/cycle}$  at  $200^\circ\text{C}$ . A slight decrease is also seen at  $250^\circ\text{C}$  as the experimental curves.

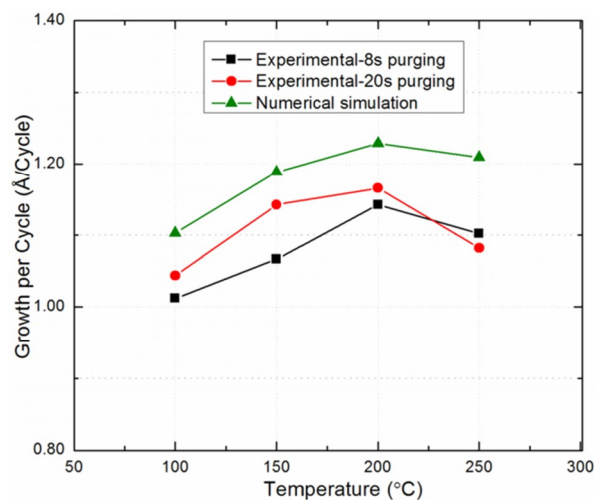


Figure 3.4 Comparisons of surface-averaged  $\text{Al}_2\text{O}_3$  film growth rates in  $\text{Å/cycle}$  by experimental and numerical investigations.

The numerical GPC is  $\sim 0.05 \text{ \AA/cycle}$  larger than the experimental results averagely. The larger values are mainly due to the presumed assumptions in numerical modeling. The theoretical modeling process has simplified the actual process with several assumptions listed in the previous section, while in experiments several factors are involved to hinder the deposition process. For instance, at the initial state, hydroxylation of the wafer surfaces cannot be perfectly 100% (which is assumed in numerical modeling). Also, calculations based on DFT showed that complex intermediate products are generated in ALD reactions [Delabie, et al., 2012]. However, for computational feasibility and simplicity, numerical model neglects these intermediate species. The involvement of intermediate reactions is difficult to be predicted without actual experimental conditions, because they are heavily dependent on precursor dosage, purging time, local precursor concentration, surface species coverage, and local temperature, etc.[Cheng, et al., 2005, King, et al., 2011, Krajewski, et al., 2009, Kukli, et al., 2002, Puurunen, 2005, Rai, et al., 2012, Wind and George, 2010]. The agreement of GPC between experimental and numerical results confirms the validity of our numerical model, which are used for further exploration of ALD process in detail.

### 3.5.2 Numerical investigations

#### (1) Full cycle flow simulation: effect of carrier gas flow rate

To correlate the growth rate observed in experiments (Figure 3.3) with material distributions, precursor concentrations are obtained by solving the species transport Eq.(3-4) with incorporation of the momentum conservation Eq.(3-2) and the energy Eq.(3-6). The



numerical study is implemented by running a full cycle of ALD simulation.

Molar concentrations of TMA and water are probed during the transient calculations at five spots corresponding to the samples in experiments. Figure 3.5 (a) and (b) show TMA distribution for purging flow rate 20 sccm and 200 sccm, respectively. At the initial state, only N<sub>2</sub> exists in chamber. TMA vapor is injected into the system by opening the ALD stop valve for 0.015s. The inlet sample (point A) responds much faster than any other samples. TMA at both point C and E reach to the highest concentration within the pulsing step, but the peak molar fraction at B and D is only ~60%.

In the following 10 s precursor purging step, TMA is diluted in chamber by the continuously incoming carrier gas and purged by the vacuum pump. TMA concentration at point A decreases dramatically from its peak value, but molar fractions at B and D increase to nearly 80% at the end of purging process (10.015 s) after a slight decrease. In the first half ALD cycle (0.015/10 s), TMA at point A remains at higher concentration level for longer time than any other samples. Higher concentration increases the collision probabilities of precursor molecules with the surface sites and results in higher deposition rates in the inlet area observed in experimental GPC results (Figure 3.3). On the other hand, the lower deposition rates at sample B and D are due to the lower precursor concentration levels.

By comparing Figure 3.5 (a) and (b), it is concluded carrier gas flow rate exerts little influence on pulsing step, but it largely determines precursor distributions during purging step. In the case of 20sccm flow rate, TMA concentrations remain high in the most area of chamber (at B, D, and E > 50%), while much lower concentrations (all the samples < 20%) are observed for 200 sccm flow rate.

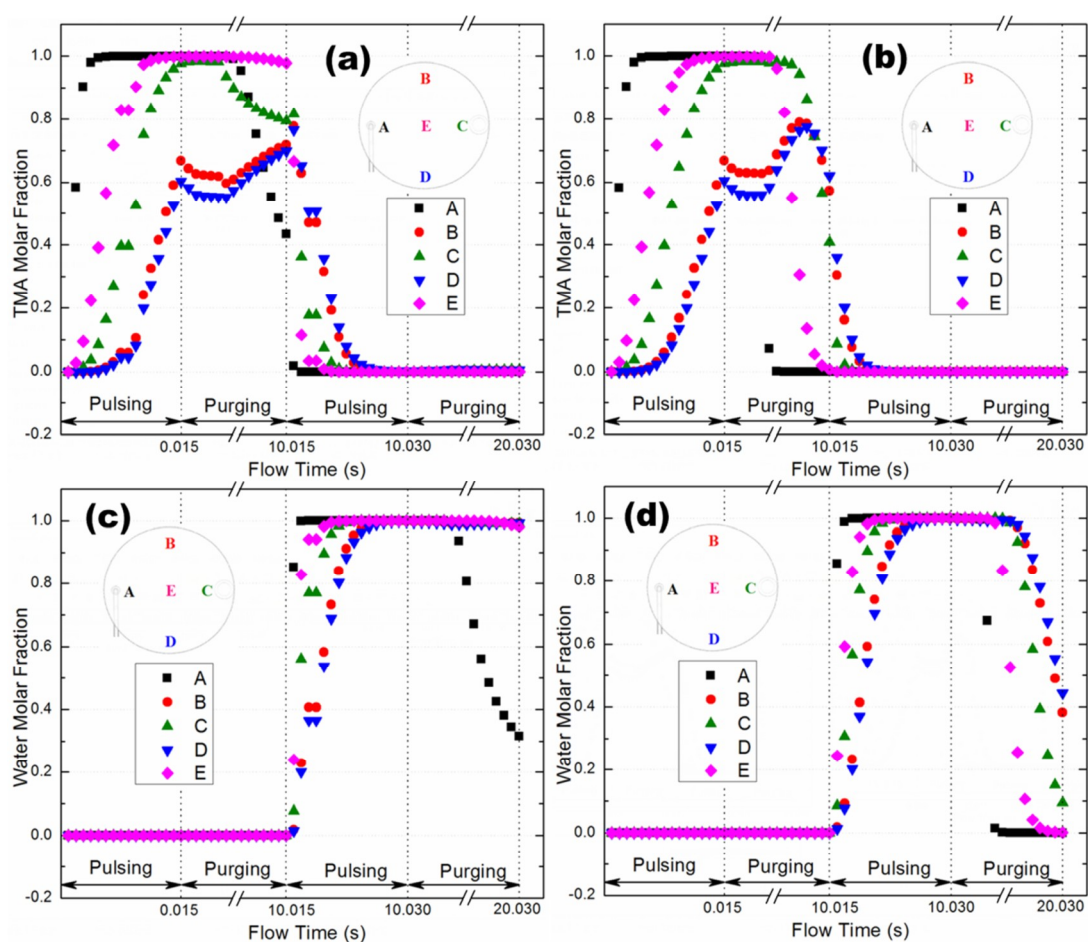


Figure 3.5 Precursor distributions during the full cycle of flow simulations for: (a) TMA molar fraction for carrier gas flow rate of 20sccm; (b) TMA molar fraction for carrier gas flow rate of 200sccm; (c) Water molar fraction for carrier gas flow rate of 20sccm; (d) Water molar fraction for carrier gas flow rate of 200sccm. A is located in inlet area, and C in the outlet area.

In the second-half cycle, water vapor is introduced into chamber. Figure 3.5 (c) and (d) demonstrate water vapor distribution for carrier gas flow rate of 20sccm and 200sccm, respectively. Comparing with TMA, water vapor molecules take the whole chamber space much faster. Different purging gas flow rate makes no difference on water distributions in the pulsing step, neither. However, for 20 sccm flow rate as shown in Figure 3.5 (c), precursor concentrations at the four samples except A are kept at higher levels through the 10s purging step. This implies that 20sccm flow rate is not sufficient to purge all the precursor material out of ALD system. By 200sccm flow rate, the situation is much improved as shown in Figure 3.5 (d).

From simulations, it has been shown the driving force to inject precursors into ALD system is mainly due to the relatively strong flow field caused by high precursor vapor pressure, but after the very rapid pulsing (0.015s) process, precursor molecules are mainly driven by the relatively weak flow field formed from carrier gas. During the slow purging procedure, precursor molecules still have chances to collide and react with the reactive surface sites. This is why longer purging time slightly increases the growth rate as seen in experiments.

Increasing carrier gas flow rate will speed up the purging procedure, but this will also shorten collision time of precursor molecules with surface species which hence will result in lower deposition rate. An alternative way is to increase the purging time. However, this implies longer ALD cycle time, which is usually unfeasible in real applications considering

hundreds of cycles needed to deposit a film.

(2) Surface chemistry simulation: effect of process temperature

To further study the surface reaction details numerically, ALD surface chemical kinetics modeled by Eq.(3-12) and Eq.(3-8) is integrated into species transport and flow simulation by evaluating the production or destruction rate of species  $i$ ,  $R_i$  in Eq.(3-4).

Figure 3.6 shows the correlations of surface deposition rate of  $O_{<s>}$  and TMA molar fraction with surface coverage of  $*Al(CH_3)_2(s)$  for TMA pulsing step at 100°C, 150°C, 200°C and 250°C, respectively. Coverage of species  $*Al(CH_3)_2(s)$  increases in the first 0.005s, and  $O_{<s>}$  deposition rate reaches its peak. When  $*Al(CH_3)_2(s)$  is saturated to 50% [another half is taken by  $*AlCH_3(s)$ ], the deposition rate declines drastically. Thereafter, despite the increasing TMA concentration, the surface coverage and deposition rate remain unchanged.

The grey dot lines indicated in Figure 3.6 show temperature effect on surface reactions. The mass deposition rate increases with temperature from 100°C to 250°C in the first 0.004s. However, at 0.004 s, deposition rate of 250°C is seen slightly lower than that of 200°C. The reason can be found by observing  $*Al(CH_3)_2(s)$  surface coverage at 250°C. At 0.004 s, surface species has already been saturated at 250°C, compared to an unsaturated condition at 200°C. This implies that surface deposition is highly dependent on surface coverage

conditions.

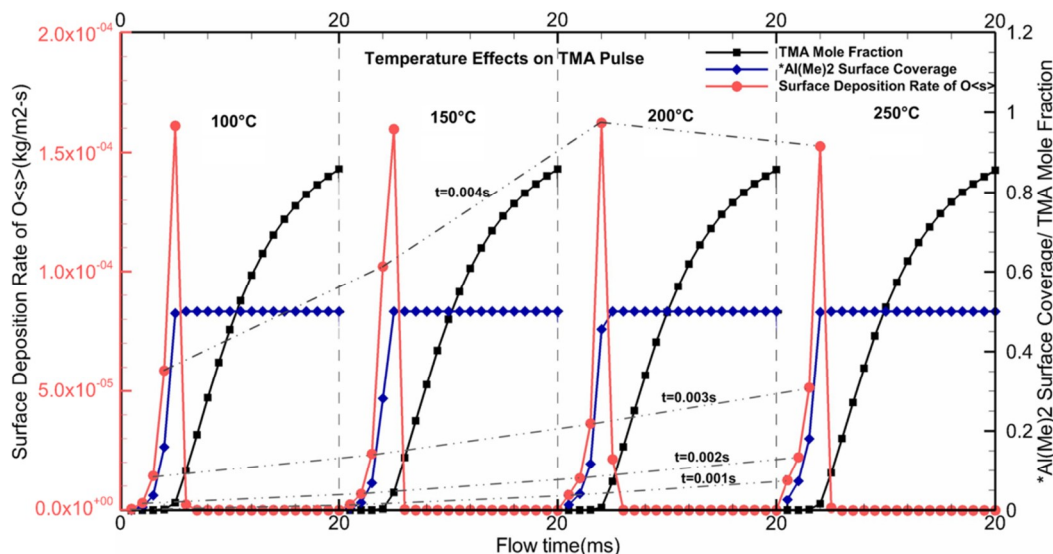


Figure 3.6 Correlations of surface deposition rate of  $O_{(s)}$  and TMA molar fraction with coverage of  $*Al(CH_3)_2(s)$  for TMA pulsing step at 100°C, 150°C, 200°C and 250°C, respectively. The grey dot lines show the temperature effect on surface deposition.

It is also worthwhile to point out that the peak deposition rate is independent of process temperature. With temperature changing from 100°C to 200°C, the peak values of deposition rate are mostly the same. However, higher temperature indeed accelerates the deposition process before surface species get saturated.

Figure 3.7 presents the relation of mass deposition rate of  $Al_{(s)}$  with  $H_2O$  concentration and surface coverage of species  $*OH$  during water pulsing step. As water vapor is injected into the system, water concentration is increased and  $*OH$  coverage is approaching its saturation status. The mass deposition rate increases and then is restrained as surface sites are saturated with  $*OH$ .

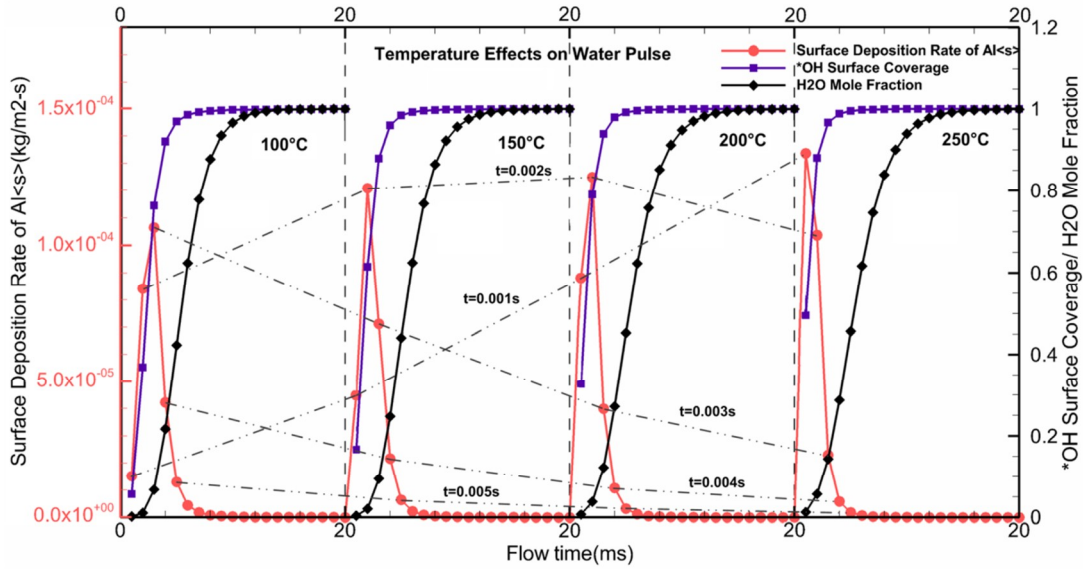


Figure 3.7 Relation of surface deposition rate of Al<sub>s</sub>, H<sub>2</sub>O molar fraction and coverage of species \*OH for water pulsing step at 100°C, 150°C, 200°C and 250°C, respectively. The grey dot lines show the process temperature effect on surface deposition.

Temperature effect on the second half surface reaction shows more complicated features. Surface deposition rate is increasing with temperature only in a very short time, and after 0.003 s, the surface deposition becomes hindered by higher temperature. This could be explained by surface species coverage in Figure 3.7. With increasing temperature, higher deposition rate corresponds to higher coverage (~50%) of \*OH at 250°C. Surface species \*OH at 250°C gets saturated much faster than other temperature conditions. Decreased deposition rates are resulted from smaller coverage of reactive species \*Al(CH<sub>3</sub>)<sub>2</sub>(s) and \*AlCH<sub>3</sub>(s). However, the peak value of surface deposition rate in pulsing process is increased by higher temperature.

Figure 3.8 presents bulk Al<sub>2</sub>O<sub>3</sub> mass deposition rate in pulsing step at five probed points for

the four temperature treatments. Bulk  $\text{Al}_2\text{O}_3$  growth rate is obtained from summation of the resulted bulk species  $\text{O}_{\langle s \rangle}$  and  $\text{Al}_{\langle s \rangle}$  in the two half reactions. Inlet sample (point A) is shown having a quicker and larger response of surface deposition rate.

These observations are consistent with the flow simulation results shown in Figure 3.5: the sample which has a quicker and larger response to the precursor flow has a quicker and larger response to the surface reactions. Flow impacts the deposition process through material distributions. This also agrees with the experimental observations presented in Figure 3.3 in which the highest deposition rate is observed at the inlet sample.

To summarize, both our experimental and numerical investigations on alumina ALD process show that the film deposition rate is dependent on process temperature. Higher temperature accelerates surface deposition processes, but surface reactions also heavily depend on the surface conditions, such as precursor concentration, precursor contacting time with the wafer surface and surface species saturation status. Before surface species get saturated, deposition rate is increasing with precursor concentration and the rate is largely restrained once the surface sites are fully taken by non-reactive surface species. Surface reactions are strictly self-terminated after reactive surface species are totally substituted, even though precursor concentration is still being increased. This is the self-limiting nature of ALD operations, which ensures the uniformity and accurate thickness controllability of deposited films.

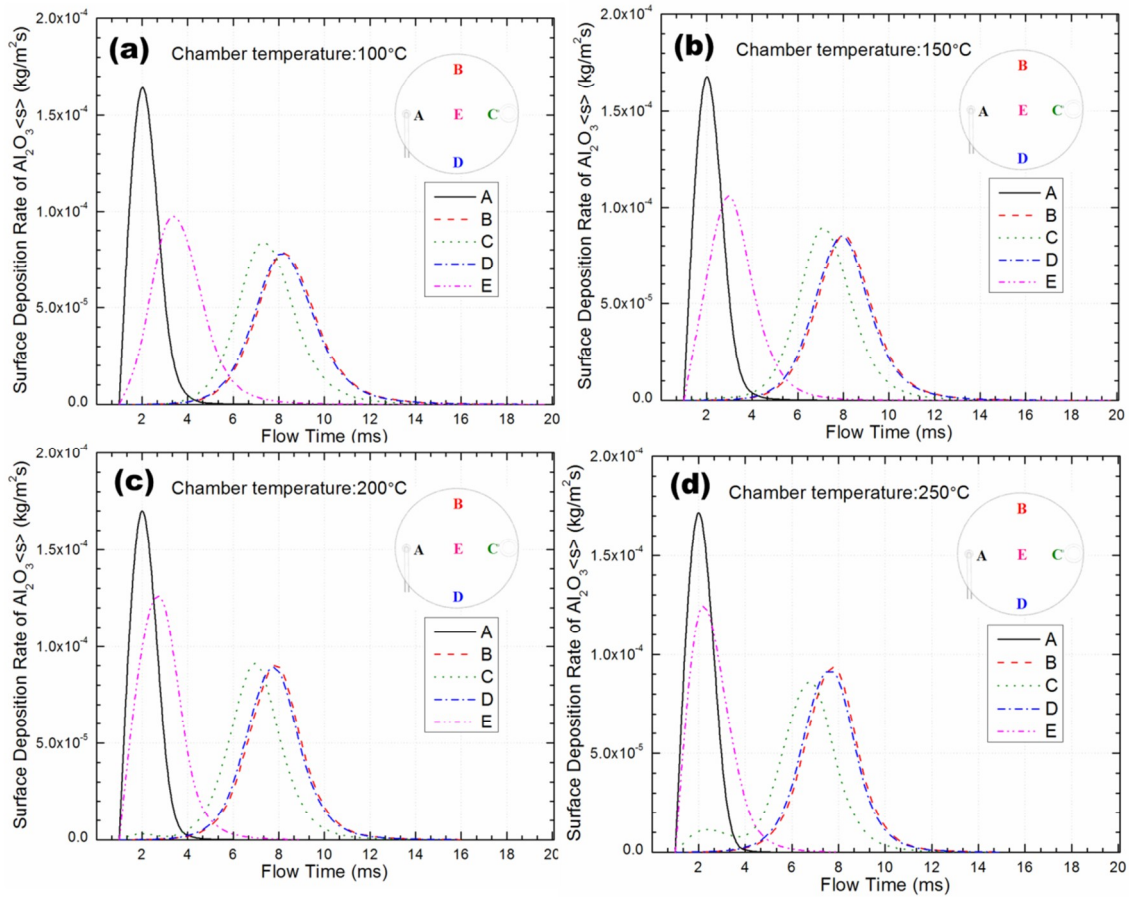


Figure 3.8 Surface deposition rate of bulk  $\text{Al}_2\text{O}_3<sub>s</sub>$  at five different positions in TMA pulsing step for 100°C, 150°C, 200°C and 250°C, respectively. Point A is located in the inlet area, and point C in the outlet area.

### 3.6 Summary and conclusions

This chapter presented a combined numerical and experimental study on the physical and chemical details of  $\text{Al}_2\text{O}_3$  ALD using TMA and water. It's been found in our experiments that the film deposition rates of all the five samples are positively dependent on temperature below 200°C. The growth rate is seen increasing with process temperature, but declines at higher temperature, e.g., 250°C for 8 s purging time. The inlet sample has higher growth rate than other samples. Longer purging time slightly increases the surface-averaged growth



rate, but specific sample responds differently.

By numerical simulations, several insightful observations were made to better understand the ALD process. The discrepancies revealed among the five samples in experiments were correlated with precursor distributions during pulsing and purging processes. Higher GPC observed at inlet sample in experimental treatments is mainly due to the longer and larger precursor concentrations. Pulsing is a quite rapid procedure in milliseconds, but purging is a relative slow procedure during which precursor materials also react with the reactive surface sites. This was confirmed by the increased growth rate with extra purging time observed in the experiments.

By tuning the carrier gas flow rate from 20 sccm to 200 sccm, it was observed the flow rate has little influence on pulsing process. However, the amount of residual precursors left in the system after purging procedure is largely determined by carrier gas, because purging process is mainly driven by the flow field formed from carrier gas. The purpose of introducing inert gases such as nitrogen and argon into ALD system is more to “purge” the precursor out of ALD system than to “carry” the precursor molecules into the chamber.

The results from numerical chemistry simulations confirmed the self-limiting feature of ALD cycles. Surface deposition was seen a strictly self-limited process: surface deposition reactions are restrained once the surface species get saturated, even though the precursor

material is still being introduced into the system. By the transient numerical simulations, effect of chamber temperature was shown to increase the deposition rate, but this effect is confined by the saturation conditions of surfaces sites. The differences of surface reactions among the five samples are consistent with the observations from experiments. The ALD process is a complex strong-coupled fluid, thermal and chemical process which is not only heavily dependent on the chemical kinetics and surface conditions but also the flow and material distributions.

# **CHAPTER 4 EXPERIMENTAL AND NUMERICAL INVESTIGATIONS OF MULTI-WAFER BATCH ALD FOR THROUGHPUT IMPROVEMENT**

## **4.1 Introduction**

In order to achieve higher throughput for fabrication of ALD thin films with hundreds of nanometers, in early 1970s batch reactors were already utilized, for example, to manufacture flat panel displays [Haukka, 2007]. At the very initial stage of ALD research for semiconductor applications, most ALD studies were conducted in single-wafer ALD systems, and at that time, throughput and other economic considerations were the secondary concern to devise and develop ALD equipment [Granneman, et al., 2007]. As the semiconductor industries are seeking higher volume manufacturing techniques, the cost of ALD process becomes more sensitive in today's business decisions. As a result, batch-type ALD systems are being introduced in cost-sensitive fields such as DRAMs and flash memories [Granneman, et al., 2007].

Batch ALD reactors can be largely divided into two categories: multi-wafer and spatial ALD. Figure 4.1 shows the schematics for the two types of batch ALD systems. Multi-wafer ALD reactor as presented in Figure 4.1 (a) is a traditional technique in which multiple wafers are coated simultaneously, and the substrates remain stationary in the pulse-purge sequence [Granneman, et al., 2007, Johansson, et al., 2010]. Multi-wafer ALD systems have already been made commercially available by a number of ALD manufacturers, such as Cambridge

Nanotech (Phoenix series), Picosun (SUNALE P-series), BENEQ (TFS series), etc. Spatial, or continuous ALD system as shown in Figure 4.1(b), is based on a brand new concept [Johansson, et al., 2010]. With the spatial concept, the ALD cycles occur in the spatial domain, and materials are deposited continuously on the wafer [Delft, et al., 2012]. As shown in Figure 4.1 (b), the wafer is moving under the precursor containers and contacting with the precursors one after another. It's been widely accepted that scaling up from single-wafer ALD to the batch-type ALD process can largely increase the throughput of ALD cycles [Delft, et al., 2012].

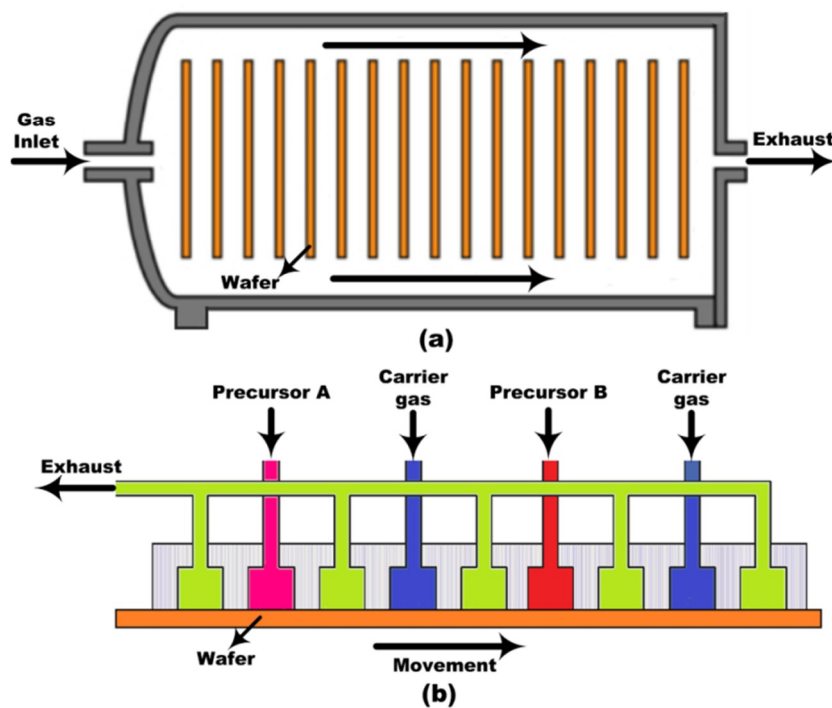


Figure 4.1 Schematics of the two main categories of batch ALD systems: (a) vertical stack-type multi-wafer ALD reactor [Granneman, et al., 2007]; and (b) in-line spatial ALD reactor [Johansson, et al., 2010, Poodt, et al., 2012].

Currently, various multi-wafer ALD systems have been already developed, but meanwhile

most efforts are being made in designing various structures of multi-wafer reactor systems. The complex physical and chemical processes in multi-wafer ALD, however, remain not well understood [Granneman, et al., 2007, Hirvikorpi, et al., 2014, Johansson, et al., 2010, Maydannik, et al., 2011, Okuyama, et al., 2005, Owyang and Bartholomew, 2005, Poodt, et al., 2012, Poodt, et al., 2010, Puurunen, 2005]. In fact, ramping-up from single-wafer to multi-wafer system is not straightforward. Due to the larger volume and presence of multiple wafers, the gas flow field in multi-wafer ALD chamber is altered, e.g., in the stack-type multi-wafer reactors as illustrated in Figure 4.1 (a), the gas flow is blocked by the rows of wafers inside the chamber. Consequently, precursor exposure and purging times may need to be prolonged in multi-wafer ALD reactors [Delft, et al., 2012]. Meanwhile, the process pressure and process temperature need to be re-evaluated for multi-wafer ALD process.

Because of these issues, detailed knowledge on the ALD process is crucial to search for the optimal operation parameters to ensure an excellent film deposition uniformity, high deposition rates and high material utilization efficiency. Experimental trial-and-error methods are always time-consuming and expensive. To better serve this purpose, researchers resort to numerical methods instead of experimental trials to study the physical and chemical procedures both in atomic and reactor level. Numerous publications on single-wafer ALD process are available both in atomic and chamber scale [Adomaitis, 2011, Afshar and Cadien, 2013, Delabie, et al., 2012, Dkhissi, et al., 2008, Elliott and Greer, 2004,

Gilmer, et al., 2000, Gou, et al., 2008, Holmqvist, et al., 2013, Hu, et al., 2009, Mazaleyrat, et al., 2005, Pan, et al., 2015, Pan, et al., 2014, Puurunen, 2003, Xie, et al., 2015].

Unfortunately, the literatures regarding multi-wafer ALD process are very limited. Lankhorst et al. presented their numerical studies by transient, three-dimensional, multi-scale simulations on the precursor pulse step during the HfO<sub>2</sub> ALD process, and identified several time scales in multi-wafer vertical batch ALD process [Lankhorst, et al., 2007]. Granneman et al. analyzed several configurations of single-wafer reactors and multi-wafer batch reactor systems from an industrial perspective [Granneman, et al., 2007]. It is worthwhile to be noted that the available numerical models on multi-wafer ALD process lack detailed surface reaction kinetics and mechanism information, or the numerical results are not well validated and correlated with the experimental observations [Pan, et al., 2015].

In this chapter, the transient multi-wafer batch ALD process of depositing Al<sub>2</sub>O<sub>3</sub> thin films on silicon wafers using TMA and water is studied by both experimental and numerical approaches. To find the influence of wafer layout on the deposition process, two types of wafer arrangements, i.e., vertical and horizontal multi-wafer ALD, are specifically investigated. In particular, the two arrangements are compared in terms of alumina thin film growth rate. Further investigation on the detailed knowledge of the precursor transient pulsing process is carried out by 3D numerical simulations.

## 4.2 Experiments

Experimental characterizations of the  $\text{Al}_2\text{O}_3$  film growth rate for vertical and horizontal multi-wafer batch ALD are performed on the Cambridge Nanotech Savannah 100 ALD reactor with a dome lid using TMA+ $\text{H}_2\text{O}$  reactions. The Savannah 100 ALD reactor with a flat lid is shown in Figure 4.2 (a) and consists of precursor cylinders, precursor delivery manifold, carrier gas manifold, chamber, outlet pipe and a vacuum pump. TMA and water are stored in separate precursor cylinders, and the pulsing (in milliseconds) process of precursors is controlled by ALD stop valves. Nitrogen is flowing through the system continuously as a carrier gas. A vacuum pump is connected with outlet pipe to maintain the low vacuum pressure ( $\sim 10^{-1}$  Torr) in chamber. The ALD system can be equipped with a dome lid as presented in Figure 4.2 (b) to enable multi-wafer batch depositions.

In the study, experiments of two types of multi-wafer arrangements are implemented. Figure 4.2 (c) presents the vertical multi-wafer experimental setup, in which 27 silicon wafer samples are processed simultaneously. In the experiments, alumina films are deposited on wafers of crystal silicon 100 with dimensions of  $15 \times 20$  mm approximately, using 99.9% TMA as the metal provider and 99.0% distilled water as the oxidizer. The wafers are prepared by being washed in 99.9% acetone solution in an ultrasonic cleaning machine for five minutes, and then washed in 99.5% ethanol solution for five minutes. Finally, the wafers are rinsed and cleaned by 99.0% distilled water using the ultrasonic cleaning

machine for five minutes. The wafers are attached to the wafer tape frame after cleaned.

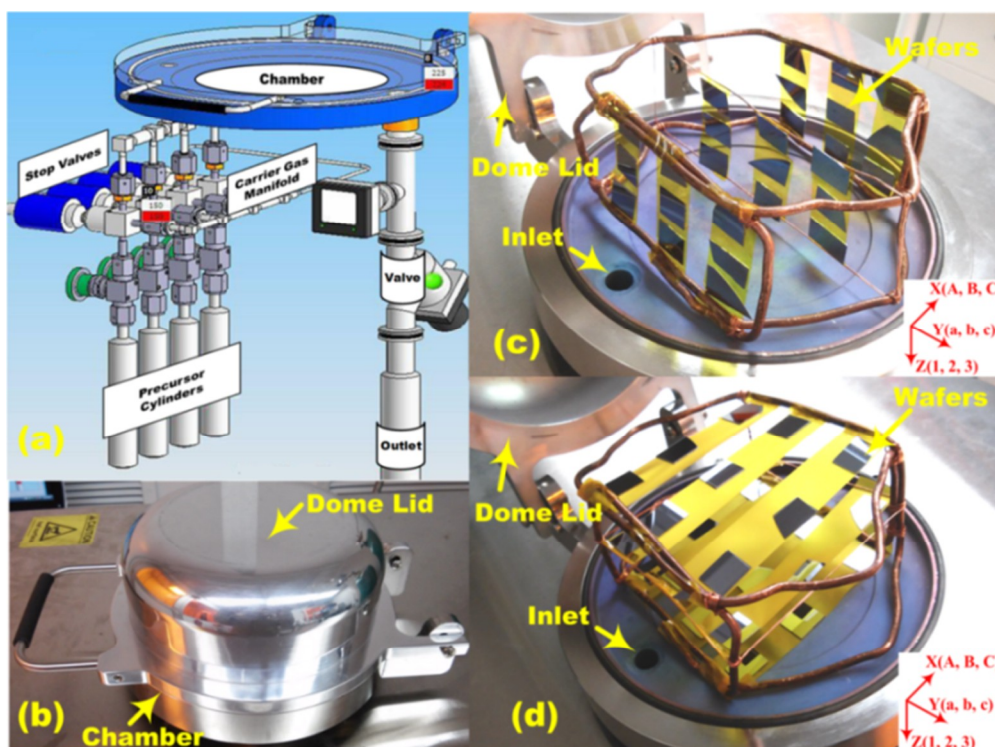


Figure 4.2 (a) Cambridge Nanotech Savannah S100 ALD reactor with a flat lid consists of precursor cylinders, precursor manifold, carrier gas delivery manifold, chamber, outlet manifold and a vacuum pump (not shown in the figure); (b) S100 equipped with dome lid for batch ALD; (c) vertical multi-wafer batch ALD setup with 27 silicon wafer samples; and (d) horizontal multi-wafer batch ALD setup with 27 silicon wafer samples.

By vertical arrangement, it means the wafer surfaces are perpendicular to the flow direction. Similarly, the horizontal multi-wafer arrangement as shown in Figure 4.2 (d) also process the same number of wafer samples simultaneously. The wafer surfaces in horizontal arrangement are parallel with the gas flows. To compare the two arrangements of wafer configurations in the aspect of film deposition rate, the wafers are placed on the same locations. To be convenient, each wafer is labeled by letters or numbers in three



dimensional coordinates, as illustrated in both Figure 4.2 (a) and (b). Each wafer sample is uniquely marked by a combination of the above three letters or numbers. A, B, and C are used for X direction, a, b, and c for Y direction, and 1, 2, and 3 for Z direction. For instance, the center wafer is labeled as B-b-2. This labeling method is used through the entire chapter.

Before deposition process begins, the ALD system is heated to the targeted temperatures (chamber: 200°C, inlet and outlet manifolds: 150°C) and stabilized for 3600 s. Pulsing time for water is set at 0.015 s, and for TMA is 0.03 s. The purging time for both TMA and water is 30 s. Hence, an ALD cycle in our experiments is TMA/purge/water/purge= 0.03/30/0.015/30 s. Nitrogen is flowing through the system at 20 sccm. A total of 100 cycles are deposited for both vertical and horizontal multi-wafer arrangements. The deposited alumina film thickness on the silicon wafers is characterized by a spectroscopic ellipsometer (HORIBA, UVISEL).

### **4.3 Model equations**

ALD modeling involves decoupling and coupling steps. First, ALD is decoupled into several physical and chemical processes, namely, momentum transport (gas flow), convective heat transfer, species transport, and surface reactions. Each process is represented by corresponding partial differential equations (PDEs). These PDEs can be solved numerically on the defined nodes in meshed domains. Second, to obtain solutions to the entire numerical ALD process, the system of PDEs must be coupled together by taking

interactions between each physical and chemical process into account. The mathematical modeling process and assumptions are described in detail in Chapter 3 [Pan, et al., 2015]. In this chapter, we focus on applying the model to simulate the deposition process in the multi-wafer batch ALD system. The chemisorption reaction mechanism is adopted to model the reactions in  $\text{Al}_2\text{O}_3$  ALD process [Delabie, et al., 2012, Pan, et al., 2015]. The surface reactions are formulated by the same half reactions as presented in Eq.(3-15).

#### 4.4 Numerical solutions

Three-dimensional numerical domains based on the Cambridge Nanotech S100 ALD reactor with the dome lid are presented in Figure 4.3 (a) and (b). The domains include the main parts of the ALD system, including chamber, wafers, inlet pipes, and outlet. To compare and validate the numerical solutions with experiments, the domains are created accurately according to the two experimental setups shown in Figure 4.2 (c) and (d).

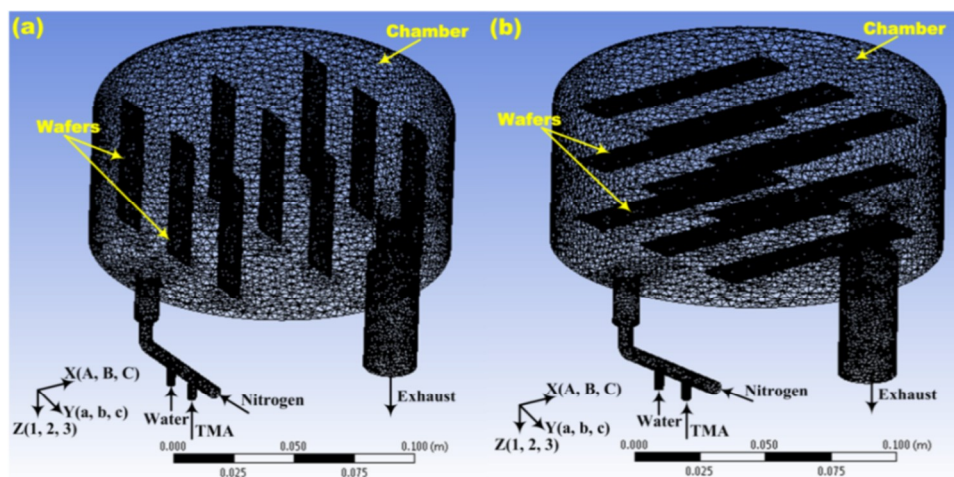


Figure 4.3 3D computational domains in the numerical model are based on S100 ALD reactor with the dome lid: (a) vertical multi-wafer arrangement; and (b) horizontal multi-wafer arrangement.

Numerical solutions to the model equations are obtained under the framework of ANSYS Fluent using the method of Finite Volume Method (FVM). The 3D domains are processed with a non-structural meshing scheme as shown in Figure 4.3. The model equations are first discretized in space by the second-order upwind method. By FVM with a pressure-velocity coupled scheme, the values at each domain node are calculated. Second-order implicit method is used for the discretization of time domain. The choice of the implicit method is to ensure computational stability, and the second-order method is for a sufficient computational accuracy.

Boundary conditions are essential in numerical solutions. In our models, the boundary conditions at inlets, outlet, wall and wafer surface sites are specified according to the actual experimental conditions. For carrier gas inlet, volumetric flow rate is set at 20 sccm. The chamber is maintained in low pressure ( $\sim 10^{-1}$  torr) by a vacuum pump which is connected with the outlet pipe. Since precursors are stored in separate cylinders as shown in Figure 4.2 (a) at room temperature and injected into the system by the pressure difference with the chamber, pressure boundary conditions are enforced on the two precursor inlets. The outlet is connected with the pump and the system background pressure is assigned, which is also the full-load working pressure of the vacuum pump.

In actual process, materials are deposited on the entire inner surface of the ALD system, but in numerical solutions, for computational simplicity without losing its accuracy, we only

calculate depositions on the wafers. Any other inner wall surfaces are assumed non-slip, non-flux of mass. At the initial state, full coverage of hydroxyl group on wafer surfaces is assumed for both vertical and horizontal multi-wafer arrangements. Thermal boundary conditions are enforced on the walls. Temperature at wafer surfaces is maintained at 200°C, and other parts of the system are 150°C.

## **4.5 Results and discussion**

### 4.5.1 Experimental and numerical characterizations of film deposition rate

In this section, material deposition rate is characterized by both experimental and numerical approaches. In both vertical and horizontal multi-wafer experiments, Al<sub>2</sub>O<sub>3</sub> film thickness is measured using the Horiba UVISEL spectroscopic ellipsometer after 100 cycles of depositions. Since the flow domains are symmetric with respect to the flow direction (X direction), material distributions are similar at the two sides of the center line of chamber. Hence, to simplify our data analysis, 18 wafers from b and c in Y direction labeled as A (B, C)-b (c)-1 (2, 3) are considered. The experimental results are presented in Figure 4.4, which are obtained by averaging two measurement data points for each wafer sample.

To obtain bulk Al<sub>2</sub>O<sub>3</sub> deposition rate from numerical simulations, mass deposition rates of species O<s> and Al<s> in the two half reactions [Eq.(3-15)] are integrated over pulsing time, i.e., for TMA pulse, 0.03s, and water pulse, 0.015s. The resulted mass deposition is finally converted to film thickness by introducing alumina film density [Groner, et al.,

2004]. The data of film thickness in one cycle for the 18 wafers from both vertical and horizontal simulations are also demonstrated in Figure 4.4.

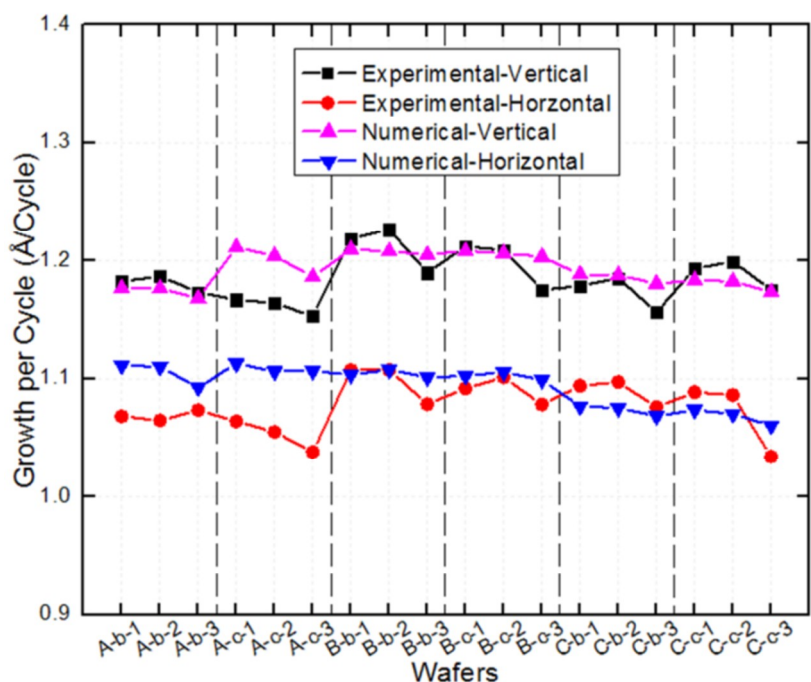


Figure 4.4  $\text{Al}_2\text{O}_3$  film growth rate in  $\text{\AA}/\text{cycle}$  for vertical and horizontal multi-wafer arrangements obtained from both experiments and simulations. The 18 wafers are labeled in three directions using A, B, C for X direction, b, c for Y direction, and 1, 2, 3 for Z direction.

As demonstrated in Figure 4.4, the data of film growth rate from numerical simulations match well with the experiments both in vertical and horizontal multi-wafer ALD processes. This agreement validates our numerical solutions. In Figure 4.4, vertical arrangement is clearly shown having higher film deposition rate than the horizontal arrangement from both experimental and numerical results. In the horizontal multi-wafer arrangement, the growth rates are  $\sim 1.1 \text{ \AA}/\text{cycle}$  from both experiments and simulations. The increase of growth per cycle (GPC) in vertical multi-wafer ALD is  $\sim 0.1 \text{ \AA}/\text{cycle}$  on average. This improvement is significant considering that hundreds of cycles are required to deposit a thin film. The

deposition results signify that the wafer layout is a significant influential factor in the deposition process of multi-wafer batch ALD. Apparently, vertical multi-wafer process is shown superior to the horizontal arrangement in film deposition rate.

This phenomenon is mainly attributed to the collision conditions between precursor molecules and wafer surfaces. In the vertical arrangement, collisions are greatly enhanced, because the wafer surfaces in this case are confronting the material flow directly. By gas flow, precursor material is transferred in the way of convection which results in strong interactions between precursor molecules and wafers.

Further information on the flow field verifies the above statement. Figure 4.5 shows the numerical velocity contour plots and the mass fluxes to the wafer surface during TMA pulsing process on wafer B-b-2. As presented in Figure 4.5 (a) and (b), the velocity for both vertical and horizontal arrangements are quite similar in magnitude. However, because of the different wafer arrangements, precursor flow velocity normal to the wafer surface varies dramatically from one to another. This is also confirmed by the mass fluxes to the wafer surface presented in Figure 4.5 (c) and (d) for vertical and horizontal arrangement, respectively. Mass flux is obtained from the velocity field and precursor density as,

$$J_m = \Gamma_p u_n \quad (4-1)$$

where  $\Gamma_p$  is the precursor density, and  $u_n$  is the normal component of velocity to the

wafer surface.

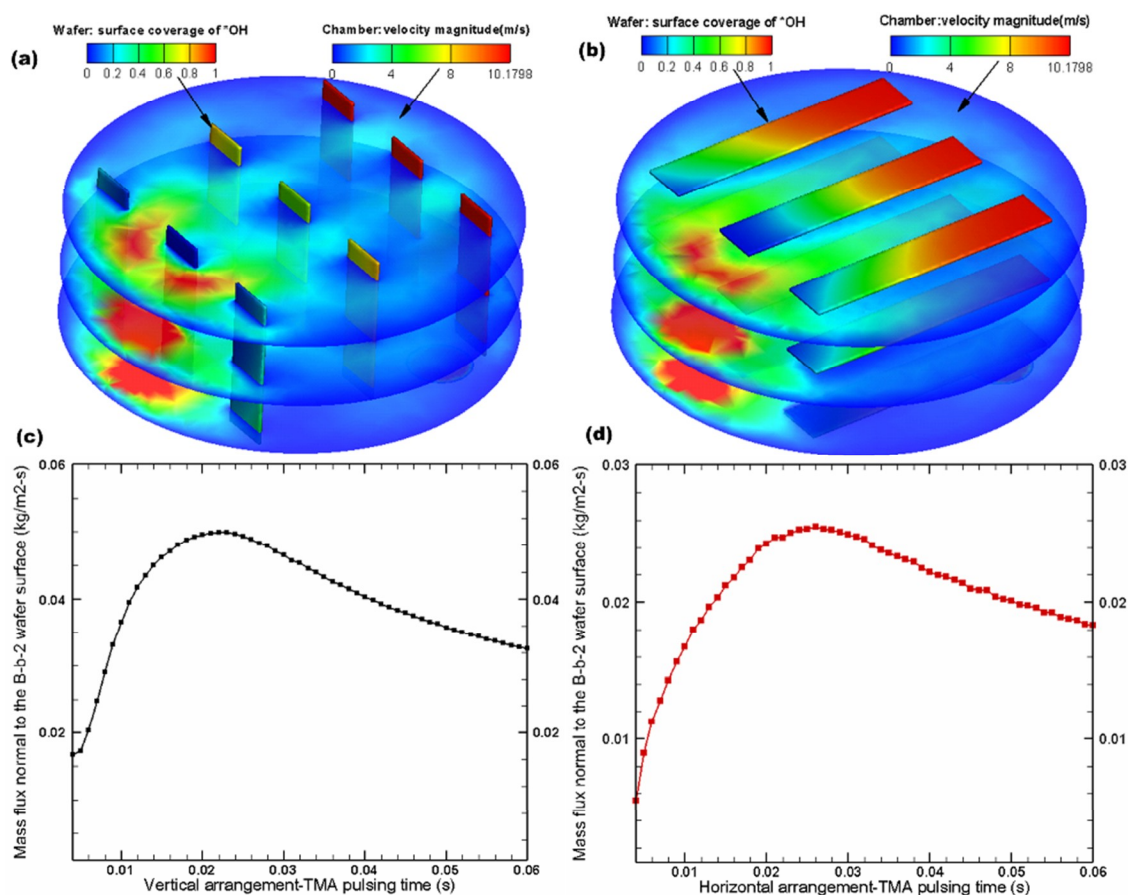


Figure 4.5 Numerical velocity contour plots and mass fluxes normal to the wafer (B-b-2) surface during TMA pulsing process: (a) and (b) velocity contour plots for vertical and horizontal arrangement at 0.015 s, respectively; (c) and (d) mass flux normal to the wafer surface for vertical and horizontal arrangement, respectively.

By comparing Figure 4.5 (c) and (d), the normal mass flux to B-b-2 wafer surface in vertical arrangement is much larger than in horizontal arrangement during TMA pulsing process. In horizontal arrangement since the wafer surfaces are parallel with the flow direction, material transportation to the surface sites are mainly driven by a diffusive effect, which is much weaker than the convection [Mills, 2013]. On the other hand, due to the larger normal velocity, the mass transfer process to the wafer surface is significantly strengthened by

convective flow in vertical arrangement, and thus the contacting and collision probabilities are increased, which leads to more surface reactions on the surfaces, and therefore higher film growth rates as shown in Figure 4.4.

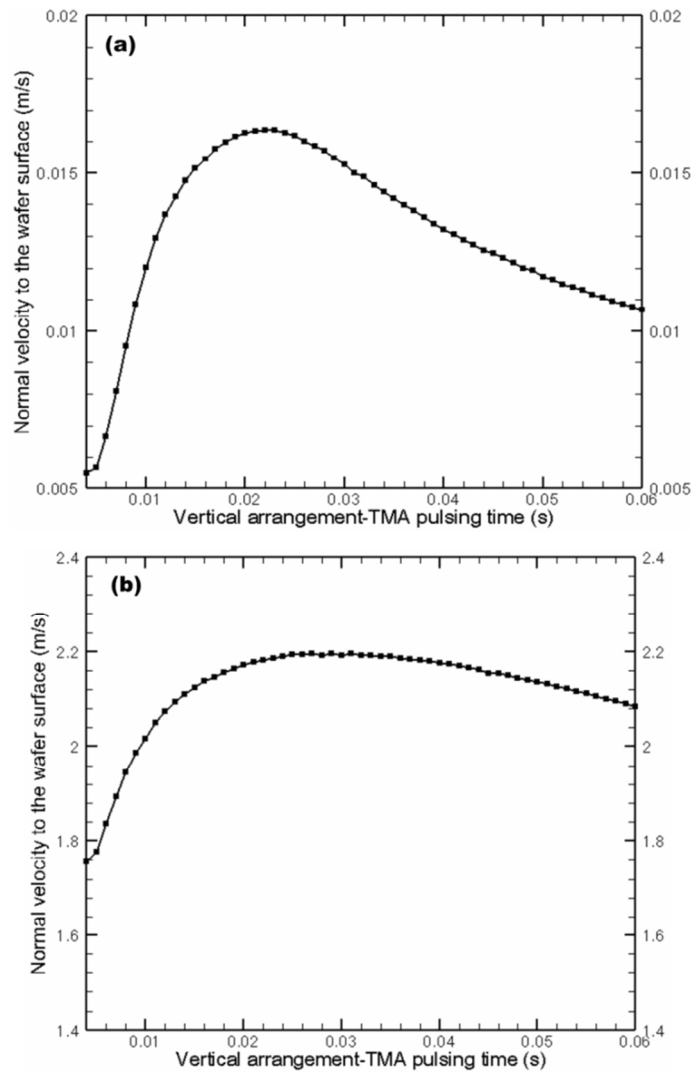


Figure 4.6 Transient normal velocity at (a) B-b-2 wafer, and (b) the space between B-b-2 and B-c-2 in TMA pulsing process for the vertical arrangement.

It is also expected that the surface deposition process in vertical arrangement could be further accelerated if the wafers are placed in such an interlined way that the wafers in the second row align to the interspace between the two wafers in the first row. This is verified



by the comparison of normal velocity at the B-b-2 wafer and the space between B-b-2 and B-c-2 in the vertical arrangement as shown in Figure 4.6. It is found that the normal velocity is much higher in the space between the two wafers.

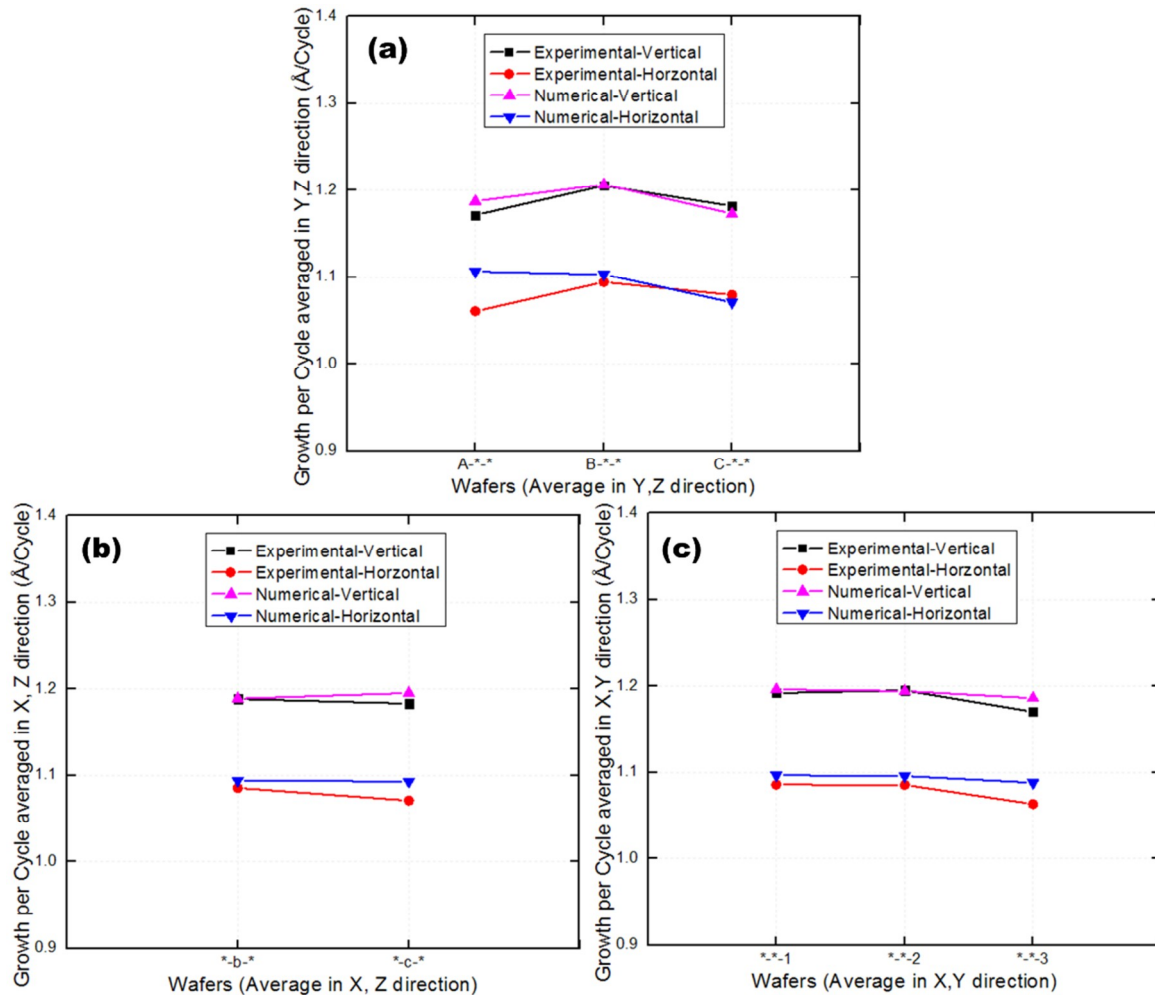


Figure 4.7 Averaged  $\text{Al}_2\text{O}_3$  film growth rates for the three directions from both experimental and numerical investigations: (a) averaged GPCs of the wafers in Y, Z direction; (b) averaged GPCs of the wafers in X, Z direction; and (c) averaged GPCs of the wafers in X, Y direction.

From Figure 4.4, the wafer position dependence of deposition rates is shown very weak by both experimental and numerical results. Further analysis of this observation is performed by taking average of the deposition rates for the three directions. The results are presented

in Figure 4.7. It is again shown that numerical data agree well with the experimental results. By Figure 4.7 (a), it is found that wafers located on the middle row (row B in X direction) have higher GPCs than those located on the other two rows. Shown in Figure 4.7 (b) and (c), little difference of deposition rates is seen in wafers located on the side column (c in Y direction) and bottom layer (layer 3 in Z direction).

#### 4.5.2 Numerical investigations of ALD transient deposition process

To further study the physical and chemical details in multi-wafer batch ALD, the transient deposition process is studied using the numerical model. To be specific, TMA and water pulsing processes are simulated with the vertical multi-wafer arrangement. In this part, the pulsing times are doubled in order to observe the entire pulsing processes, i.e., for TMA pulse, 0.06 s, and water pulse, 0.03 s. Precursor concentration, surface species coverage, methane generation and bulk material deposition rate in the transient pulsing processes are correlated in Figure 4.8. The data are extracted at the center wafer (B-b-2) for both TMA and water pulses.

It is observed in Figure 4.8 (a) that surface deposition rate increases with TMA concentration from the very beginning of pulsing step, and as the deposition continues, surface coverage of the initial species, i.e., \*OH, declines. The gaseous product, methane is generated once the reaction is activated. In the first 0.006 s, deposition rate is increasing slowly, and meanwhile hydroxyl coverage experiences a slow decline. Thereafter, the

process is expedited as TMA concentration is increasing steadily. As a result, methane-terminated species ( $*AlMe$  and  $*AlMe_2$ ) coverage is increasing quickly.

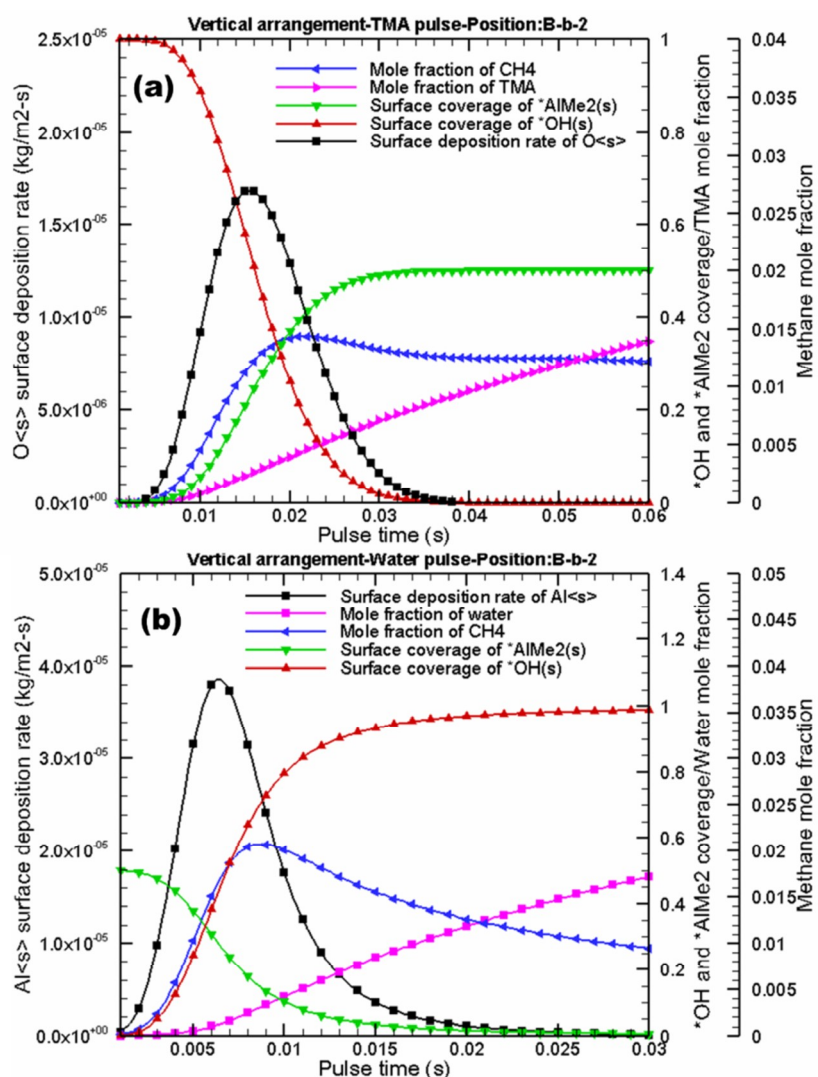


Figure 4.8 Correlations of precursor concentration, surface species coverage, methane generation and bulk material deposition rate in the transient pulsing processes by vertical multi-wafer ALD simulation: (a) TMA pulse; and (b) water pulse. Data are extracted from the center wafer (B-b-2) for both TMA and water pulses. The pulsing times are doubled from experiments in order to observe the entire pulsing processes.

At about 0.015 s, the deposition rate reaches its peak and then declines steadily despite the precursor concentration is still increasing. As the surface reaction continues, the available

reactive hydroxyl sites become scarce, and most of the hydroxyl surface species are converted to methane-terminated species. Accompanying this process, more methane is generated. At about 0.034 s, hydroxyl coverage declines to zero, and \*OH species is no longer available on wafer surfaces, and consequently surface deposition process is terminated. Nevertheless, it is noted that the precursor concentration is still increasing to higher levels. Methane generation becomes steady as the deposition process is approaching its end, and slightly declines after the reaction is terminated. Finally, \*AlMe<sub>2</sub> surface species becomes saturated to 50% (another half is taken by \*AlMe). In the process, hydroxyl-terminated surface sites are completely converted to methane-terminated species as described in Figure 4.8 (a). Precursor pulse, in essence, is a surface species conversion process, during which materials are being deposited.

In comparison with TMA pulse process, similar phenomena are observed in water pulse as presented in Figure 4.8 (b). In water pulse, however, the deposition process happens much faster. The reaction reaches its peak in only 0.006 s, and is completely terminated at ~0.02 s. This reveals the huge difference of chemical kinetics in the two half deposition processes. By Figure 4.8 (b), water pulse is shown kinetically faster than TMA pulse. This also validates the choice of shorter pulse time (0.015 s) for water pulse in the experimental treatments. The information of this critical pulse time is essential to improve the sustainability performances, such as deposition efficiency and material utilization in ALD, since any longer precursor pulsing will be a waste of time and materials once the deposition

process is terminated. In water pulse process, methane-terminated species are converted to hydroxyl-terminated surface sites, which are prepared for the next TMA pulsing step. Bulk species Al<s> is deposited in water pulse, and since it is heavier than O<s> in mass, the mass deposition rate in water pulse is higher than in TMA pulse as given in Figure 4.8.

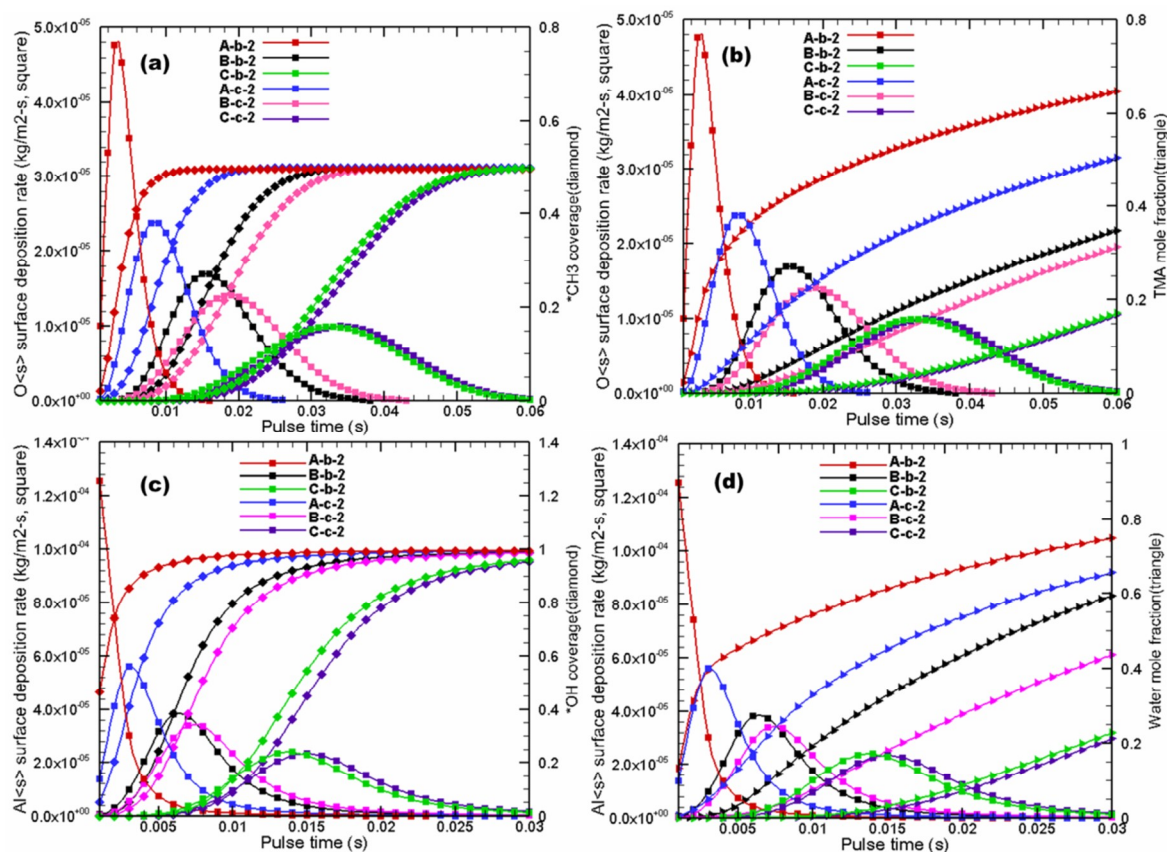


Figure 4.9 Correlations of precursor concentration, surface species coverage, and bulk material deposition rate in the transient pulsing processes by vertical multi-wafer ALD simulation for the 6 wafers located on the middle layer: (a) and (b) TMA pulse for the 6 wafers; (c) and (d) water pulse for the 6 wafers. Data are extracted from the middle wafers (layer 2 in Z direction), A (B, C)-b (c)-2, for both TMA and water pulses. The pulsing times are doubled from experiments in order to observe the entire pulsing processes.

Further data are extracted from various wafers on the middle layer (layer 2 in Z direction) and presented in Figure 4.9 to study position dependence of the deposition process. Figure

4.9 shows that in X direction (from A, B to C), precursor concentration at each wafer experiences different process in both TMA and water pulsing processes, and consequently the deposition process varies differently. The wafers located near the inlet area (row A) gain high precursor concentration first (red and blue curves), and their deposition rates reach peaks much faster than those on the other two rows.

In Y direction, wafers on column b experience faster deposition processes than those on column c, although this difference decreases from row A, B to C. Nevertheless, faster deposition process does not necessarily result in higher material deposition rate, because the final material deposition rate is achieved by integrating deposition rate over pulse time. Considering that at last all the deposition processes is completed as shown in Figure 4.9 (a) and (b), the time integration for different wafers exposes little difference on film deposition rate, which is also seen in Figure 4.4 and Figure 4.7.

The experimental results given in Figure 4.4 also indicate that no evident pattern could be identified regarding the position dependence of deposition rate. Considering the fact that the experiments only take half of the pulsing time in simulations, from Figure 4.9 the wafers located on row C have a little lower deposition rate than those on the other rows because their deposition processes are not finally terminated within the pulsing step. As a result, deposition rate of wafers on row C is a little lower as indicated in Figure 4.7 (a). Row B, however, yields the highest deposition rate. This is mainly attributed to the longer time these

center wafers have experienced with higher deposition rate, although their peaks are not the highest compared to the first row wafers.

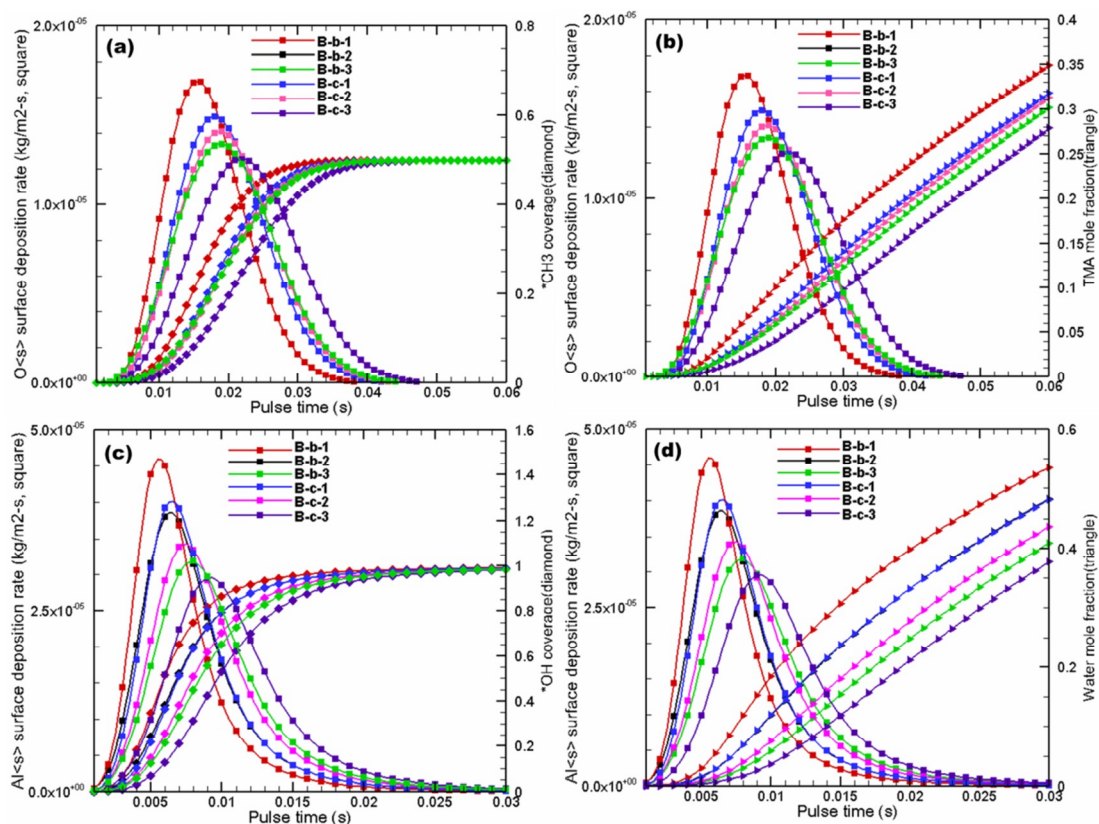


Figure 4.10 Correlations of precursor concentration, surface species coverage, and bulk material deposition rate in the transient pulsing processes by vertical multi-wafer ALD simulation for the six wafers located on the middle row: (a) and (b) TMA pulse; (c) and (d) water pulse. Data are extracted from the middle wafers (row B in X direction), B-b (c)-1 (2, 3) for both TMA and water pulses.

Figure 4.10 compares the deposition processes of the six wafers located on the middle row (row B in X direction) for both TMA and water pulses. These wafers are located in the similar distance from the inlet, and thus, they have very similar precursor distributions as shown in Figure 4.10. Hence, their depositions also experience the similar process from 1, 2 to 3 in Z direction. This is confirmed by the experimental results given in Figure 4.7 (c) that the differences of film deposition rate in Z direction are negligible. In fact, as presented in

Figure 4.4, with numerical integration of the deposition rate curves over time, the resultant overall deposition rates make no evident difference.

Therefore, it is concluded that, in general, the position dependence of deposition rate in multi-wafer ALD process is very weak and negligible, and the wafer positions make no evident difference in film growth rate. This makes great sense in large-area wafer ALD coating applications. Even on very large-area wafers, the ALD fabricated films can still be highly uniform.

To summarize the information on the transient ALD deposition process, it is concluded that the surface deposition rate is heavily dependent on precursor concentrations in the first half of deposition process, and declines steadily as the surface species conversion approaches its end. In both TMA and water pulsing processes, as the precursor molecules are being introduced into chamber, surface reactions are initiated and then speeded up with more precursor molecules. As the reactions continue, the available reactive species are consumed and converted to the product surface species. In this process, the deposition rate reaches its peak.

After the peak, the surface reaction rate is largely determined by the availability of reactive surface species. Since wafers that are located in different areas of the space, they experience high precursor concentration at different times, resulting in the different deposition



processes. To be short, in the first half pulsing process, precursor concentration is dominant in determining the reaction rate, and in the second half, deposition rate depends more on the available reactive surface species. Process deposition is under a joint influence of both precursor concentration and number of reactive surface species.

#### **4.6 Summary and conclusions**

This chapter compared the two different wafer arrangements in multi-wafer batch ALD process both experimentally and numerically. It's seen from both experiments and simulations that the wafer layout indeed influences the deposition rates significantly. The vertical multi-wafer arrangement is superior to the horizontal one in film growth rate. An increase of  $\sim 0.1 \text{ \AA/cycle}$  in deposition rate is observed from our experimental and numerical results. This is mainly attributed to the enhanced convective effect of chemical species transport to wafer surfaces in the vertical multi-wafer batch ALD process.

By 3D modeling of multi-wafer batch ALD, the transient deposition process including fluid dynamics and surface reaction kinetics was studied in detail for vertical multi-wafer arrangement. The numerical results revealed the self-limiting details of the flow and surface reaction processes. Deposition process is under a joint influence of precursor concentration and surface site saturation status. In the first half reaction before the deposition rate reaches its peak, precursor distribution is dominant to determine the bulk material deposition rate, whereas film growth rate is largely confined by the available coverage of surface reactive

sites in the second half reaction. Finally, the reaction is terminated due to no more presence of reactive surface species. The ALD deposition process is, in essence, a conversion of surface species. This is the basic chemical kinetics behind the ALD process.

By transient simulations, the deposition process is shown highly “self-limited”: surface reactions in ALD are completely terminated once the surface species conversion is finished, even though precursor molecules are still being introduced into the ALD system. This feature confirms the advantages of this thin film fabrication technique: ALD is perfect to produce highly uniform films, and the film thickness can be accurately controlled in an atomic level. Further data from the transient simulations also showed that the deposition rate is not sensitive to the wafer positions, although the time-dependent deposition process varies differently from wafers. The overall position dependence of deposition rate in multi-wafer ALD process is weak and negligible.

## CHAPTER 5 EFFECTS STUDY OF IN-LINE SPATIAL ALD FOR THROUGHPUT IMPROVEMENT

### 5.1 Introduction

ALD has a serious low-throughput limitation especially in the industrial level applications [Haukka, 2007, Suh, et al., 2012]. The conventional single wafer ALD, for instance, can only achieve 1.1~1.3 Å/cycle growth rate, that is a few nm per min for deposition of Al<sub>2</sub>O<sub>3</sub> [Poodt, et al., 2013]. The multi-wafer batch ALD still adopts the original conventional ALD philosophy of separating the two half ALD reactions in time.

Spatial ALD, however, as illustrated in Figure 5.1 (b), is totally based on a brand new concept [Johansson, et al., 2010]. In conventional ALD, the precursors are dosed one by one, and separated in time by a purging step, but with the spatial idea, the ALD surface reactions are separated in space other than in time, and precursors are dosed simultaneously and continuously with the relative movement of wafer belt [Poodt, et al., 2013]. Particularly, as shown in Figure 5.1 (b), the precursors are introduced at different positions on the wafer surface to enable the corresponding half ALD surface reactions. By introducing a pumping system and an inert separating gas, e.g., nitrogen or argon, the precursors and the reactions are separated in space. A complete full cycle of ALD is achieved by the relative movement of wafer belt. This continuous dosing process makes the spatial ALD system highly superior in film grow rate. It is demonstrated the spatial ALD can achieve as high as a few nm/s deposition rate, compared to a few nm/min in the conventional ALD system [Poodt, et al.,

2010, Poodt, et al., 2013].

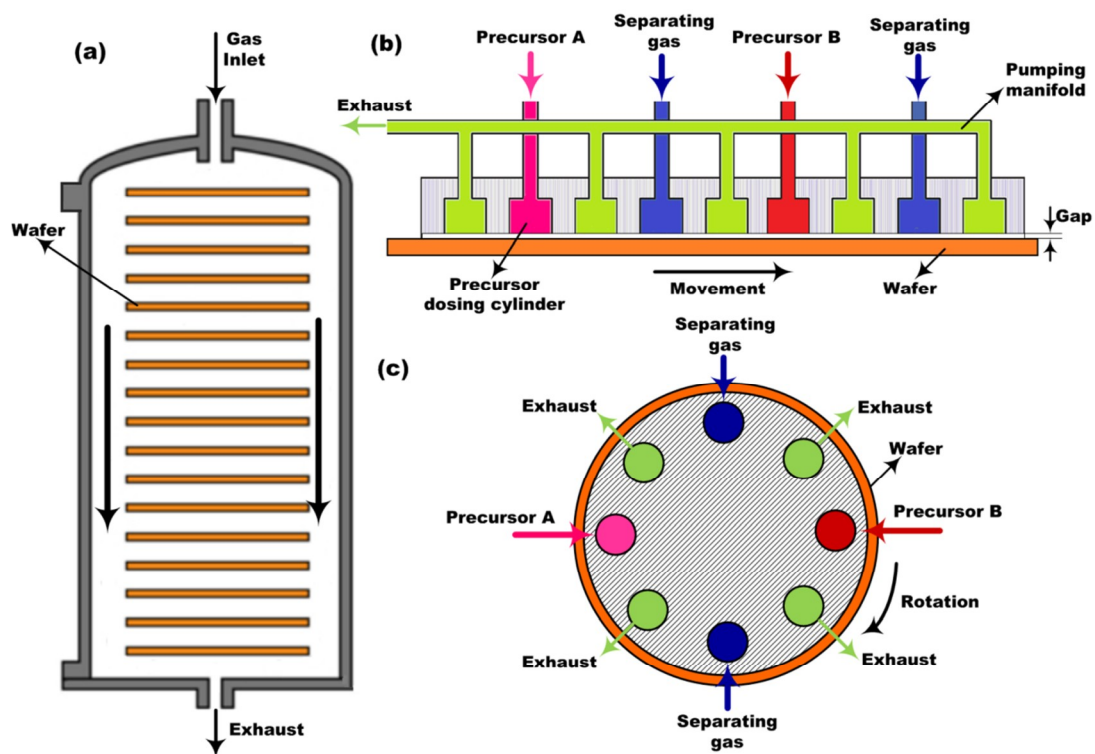


Figure 5.1 (a) stack-type multi-wafer batch ALD reactor [Granneman, et al., 2007]; (b) in-line spatial ALD reactor [Johansson, et al., 2010, Poodt, et al., 2012]; and (c) rotary spatial ALD reactor.

Following the same idea, spatial ALD reactors have two variations in structure: in-line spatial ALD as illustrated in Figure 5.1 (b), and rotary spatial ALD in Figure 5.1 (c). A typical thermal spatial ALD system (in-line or rotary) includes a wafer belt driving system, a heating unit, an exhaust pumping system, and a gas delivery system, which consists of precursors and separating gas injecting pipelines, the precursor dosing cylinders, and separating gas injecting cylinders. The pumping system is to maintain a relatively low pressure ( $\sim 10^{-1}$  torr) in the system, and to purge the residual gases. A gap must be kept between the gas cylinders and the wafer belt to allow gas flow development and the wafer-cylinder relative movement.

Choice of gap size is a critical issue in designing spatial ALD reactors, because inappropriate gap size may result in intermixture of precursor gases, and hence intermixing reactions [Suh, et al., 2012]. To investigate the influence of the gap on the flow fields, Suh *et. al.* performed gas flow simulations and Al<sub>2</sub>O<sub>3</sub> deposition experiments for a rotary spatial ALD reactor with a gap of 5 mm [Suh, et al., 2012]. Generally, too big gaps (> 5 mm) will inevitably cause precursor gases intermixing, whereas too smaller gaps (<1 mm) will hinder the gas flow, and thus the deposition process. Smaller gaps also pose a practical problem of wafer movement in massive production when the large wafer size and uneven wafer surfaces are considered [Suh, et al., 2012].

Besides, the deposition process in a thermal spatial ALD system is also highly dependent on a variety of process factors, such as temperature, precursor surface concentration, system pressure, and the precursor exposure time [Poodt, et al., 2013]. Since the chemical kinetic information involved in the ALD deposition process is highly temperature-dependent, the deposition rate is largely affected by the deposition temperature [George, 2010]. Precursor concentration on the wafer surface is determined by the mass flow field, which is influenced by the precursor and pumping pressures, and the gap size as well. The exposure time is determined by the configuration of spatial ALD reactors (e.g., size of dosing cylinders, gap size, etc.) and the relative movement speed of the wafer belt.

Due to the above complexity, studying these influential factors is crucial in designing spatial ALD systems, not only avoiding unnecessary long cycle time but also the non-uniform depositions due to the fluctuations in deposition temperature, gas flows and exposure times [Poodt, et al., 2013]. Poodt *et. al.* carried an experimental study on the chemical kinetics of depositing  $\text{Al}_2\text{O}_3$  in a rotary spatial ALD system at atmospheric pressure [Poodt, et al., 2013]. The effects of deposition temperature, precursor pressures, and precursor exposure times were investigated and discussed for a rotary spatial ALD system in this cited work. As an important factor in gas flow development and deposition process, the gap size, however, is not included in their studies. Furthermore, the results obtained from the rotary spatial reactor may not apply to the in-line ALD system.

To better serve the purpose of investigating the effects of the geometric and process parameters on the in-line spatial ALD process, in this chapter we have implemented a systematic study using an experimentally-verified fluid dynamic and chemical kinetic model for an in-line spatial ALD system. To be specific, the transient spatial ALD process of depositing  $\text{Al}_2\text{O}_3$  films on a silicon wafer belt using trimethylaluminum (TMA) and water is studied numerically. Three geometric and process factors (gap size, deposition temperature, and pumping pressures) are considered in two essential aspects of flow field and surface chemical deposition kinetics. Their influences on the fluid dynamics and surface chemical kinetics are explored and discussed in the following sections.

## 5.2 In-line spatial ALD process modeling

ALD is a strongly coupled process, but mathematical modeling is more feasible for the weakly-coupled or uncoupled process. Therefore, modeling spatial ALD firstly involves decoupling of the ALD processes. In a word, the mathematical modeling requires separating or decoupling the actual processes, but seeking solutions to the targeted system from mathematical models requires integrating and coupling each specific process.

Particularly, in the concerned in-line spatial system, ALD can be dissociated into several physical and chemical processes. ALD is a dry film fabrication technique, and the materials interact with solid surfaces in gaseous states, so the process is firstly decoupled into gas dynamics (momentum transport). ALD process involves two or more precursor species, e.g., TMA and water in  $\text{Al}_2\text{O}_3$  ALD, and hence it is also a multi-species transport process. To activate the surface chemistry in ALD process, the system is heated to certain temperature, and thus heat transfer is also considered. The knowledge in these fields is well-established, and the individual mathematical model is readily available.

The precursor materials in ALD react with the ligand-terminated surface sites, and thus, the surface chemical kinetics is considered for the deposition process. Owing to the complexity of ALD actual reaction mechanisms, detailed chemical modeling of ALD still remains a big challenge [Pan, et al., 2015]. The main reason is that few experimental studies can be found on the detailed information of the ALD chemical kinetics and side reactions. Theoretical

studies regarding ALD surface reaction mechanisms and chemical reaction pathways are mainly based on the first principle methods, such as density functional theory (DFT) method [Afshar and Cadien, 2013, Delabie, et al., 2012, Elliott and Greer, 2004, Puurunen, 2003]. The detailed modeling process can be found in our previous chapters.

### **5.3 Numerical implementations**

#### **5.3.1 System boundary definition**

The system boundary is firstly defined to model the spatial ALD process. The spatial ALD cycle is defined in space, and therefore the system boundary is determined by relevant components. Figure 5.2 illustrates the 3D computational domain of in-line spatial ALD reactor. A complete inline spatial ALD cycle of  $\text{Al}_2\text{O}_3$  goes through half reactions. Since a specific position on wafer can only complete a half reaction at one time experiencing one precursor material flow under the dosing cylinder, a complete cycle requires the position move to the second precursor dosing cylinder. Consequently, the system includes two precursor cylinders in order to model a complete spatial ALD cycle. Additionally, between water and TMA dosing cylinders, separating gas (nitrogen) is introduced to separate the two precursors. Besides, two exhaust cylinders are connected to a vacuum pump as shown in Figure 5.2 (a). The system boundary is presented as the three-dimensional domain in Figure 5.2.



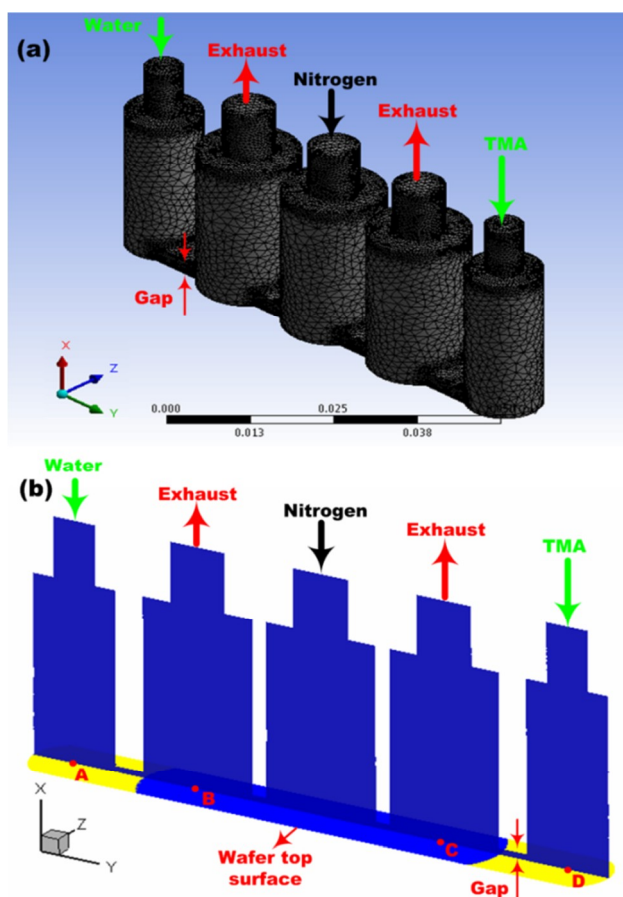


Figure 5.2 3D computational domain of in-line spatial ALD reactor: (a) fluid domain in the two precursor dosing cylinders, one separating gas injecting cylinder, two exhaust cylinders, and the gap spaces between each arrangement, dimension scale in meters, and (b) center slice of the 3D domain, A, B, C and D are the probing points for the flow or chemical deposition analysis.

### 5.3.2 Boundary conditions

Boundary conditions are the physical (fluid, thermal, etc.) and chemical constraints (concentration, surface coverage, etc.) defined on each boundary of the fluid domain, such as inlets, outlets, walls, and reactive surfaces in the spatial ALD domain [Chapra, et al., 2010, Hoffman and Frankel, 2001]. Water/TMA inlets are defined as the vapor partial pressure entering the system with room temperature (25°C). The actual partial pressure is

determined by the saturated precursor vapor pressure and the background pressure in the ALD system. Separating gas is fed at a certain flow rate to ensure proper separation of the precursor gases.

The spatial ALD reactor is driven by a vacuum pump with base pressure as low as 0.22 torr. The high vacuum environment is desirable for better surface reactions and gas separation. The exhaust outlet is the pumping pressure which can be adjusted from 0.22 to 0.32 torr. When assigning a pressure boundary condition, for an incompressible flow, it implies the flow velocity can be computed via Bernoulli's equation as following [Fox, et al., 2009, Munson, 2008],

$$p = p_0 + \frac{1}{2} \rho V^2 \quad (5-1)$$

where  $p$  is the boundary partial pressure,  $p_0$  is the base pressure,  $V$  is the gas flow velocity. With the equation, the boundary mass flow rate and fluxes of momentum, energy, and species can then be computed from the velocity information.

The system wall (cylinder and pipe wall) is treated as stationary wall boundary conditions with no mass transfer but only heat transfer across the boundary. Thermal constraint for the wall is a certain maintained temperature condition. To prevent precursor vapors from condensing, 150°C is maintained on these walls. The moving wafer belt usually has relative higher temperature, e.g., 200°C, to activate the surface reaction.

For computational simplicity, the shear effect caused by the moving wafer is neglected without influencing the accuracy of simulations. The shear stress is mainly determined by the fluid viscosity and the velocity gradient in the perpendicular direction as shown in following equation, and the reason is two-fold.

$$\tau = \mu \frac{du}{dy} \quad (5-2)$$

where  $\tau$  is the shear stress,  $\mu$  is the fluid dynamic viscosity,  $u$  is the fluid velocity along the boundary, and  $y$  is the direction perpendicular to the boundary.

Firstly, the spatial ALD system is in vacuum with  $\sim 0.22$  torr background pressure, gaseous mixture viscosity is much smaller compared to the case of atmospheric pressure. Furthermore, as revealed in our numerical flow field, the velocity is highly concentrated in the gap area, and hence the velocity gradient is small near the wafer surface. As a result, the viscous drag effect by the moving wafer surface is considered to be too small to affect the precursor distributions as well as the surface reactions. Hence, the wafer belt is assumed stationary in our numerical treatment. The wafer top surface is defined as reactive sites, where there are both heat and mass transfers.

### 5.3.3 Initial conditions

For a transient system, numerical methods are approaching to the analytical solutions iteratively starting from the initial values, and hence the fluid, thermal and chemical initial

numerical values need be assigned before calculations [Chapra, et al., 2010, Hoffman and Frankel, 2001]. Specifically, in actual spatial ALD applications, the separating gas is firstly injected into the system for a few minutes to purge the air out and stabilize the system to the prescribed base pressure. The system domain is fully taken by the separating gas, nitrogen before depositions. Therefore, in our simulations, the pressure, velocity, concentration values of nitrogen are adopted as the initial conditions.

For chemical initial values, full coverages of hydroxyl and methanl group are assumed on the wafer surfaces under TMA and water dosing cylinder, respectively. Three levels of gap size (1, 1.5, and 2 mm), temperature (150°C, 200°C and 250°C), and pumping pressure (0.22, 0.27 and 0.32 torr) are simulated to study their effects on the flow and suface deposition process.

#### 5.3.4 Numerical calculations

Numerical calculations of the model equations are carried out within the framework of ANSYS Fluent using the Finite Volume Method (FVM). The 3D domain is firstly divided into numerous finite volumes with a non-structural tetrahedron meshing scheme as shown in Figure 5.2 (a). The actual meshing size is finally decided by a compromise between calculation accuracy and computational cost.

The model equations are then discretized in space by the second-order upwind method and

the values at each domain node are calculated by FVM with a pressure-velocity coupled scheme. The second-order implicit method is used for the discretization of the model equations in time domain. The implicit method is to ensure computational stability, and the second-order method is for a sufficient computational accuracy. As shown in Figure 5.2 (b), during the calculations, transient values at the four points on the wafer top surface are probed for species concentrations (position B and C) and surface depositions (position A and D). With species concentration information, flow and intermixing of precursor materials are investigated, and with surface reactions, the film deposition process is studied.

## **5.4 Results and discussion**

### **5.4.1 Effects on the in-line spatial ALD flow field**

In this section, effects of the three factors on the spatial ALD flow field are characterized numerically, including gap size, temperature and pumping pressure. The main concern of precursor intermixture in in-line spatial ALD is paid special attention in this part, because the intermixture would deteriorate the film deposition quality by enabling the chemical vapor deposition (CVD)-type reactions in the system. Figure 5.3 shows the transient process during the dosing steps for different gap sizes.

The precursor concentrations at point B and C are shown in Figure 5.3 (a) and (b), respectively. It's seen that TMA material is indeed present at the water side for all the gap sizes, and water is detected at the TMA side. Both precursor concentrations are increasing

until the steady states are achieved during the 0.1 s dosing process. TMA concentration level (in  $10^{-5}$  mol/m<sup>3</sup>), however, is much lower than water concentration (in  $10^{-3}$  mol/m<sup>3</sup>) as shown in Figure 5.3 (a).

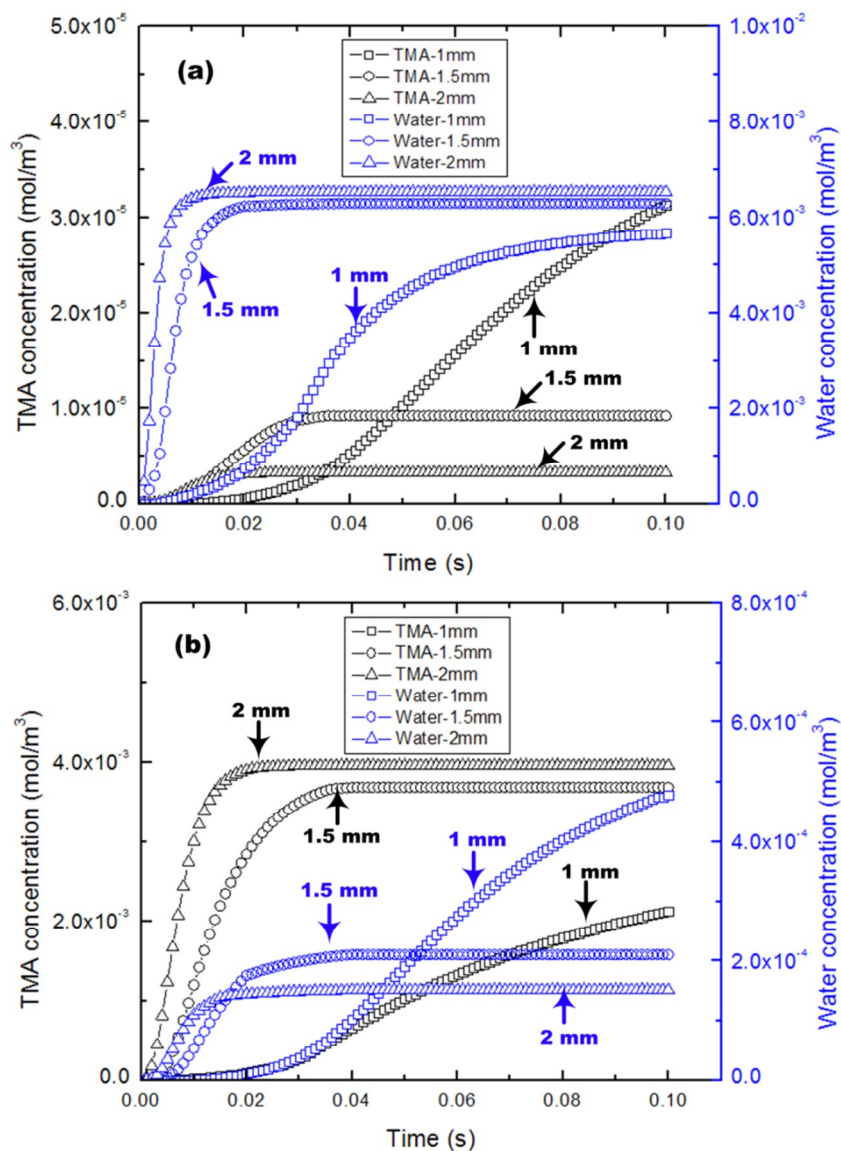


Figure 5.3 The effects of gap size on precursor intermixing with ideal pumping condition (0.22 torr) and 200°C deposition temperature: (a) TMA and water concentration in mol/m<sup>3</sup> at water side (position B) with gap size 1, 1.5, and 2 mm, and (b) at TMA side (position C) with gap size 1, 1.5, and 2 mm.

Comparing the steady concentration levels, it is found that gap size influences the precursor

distributions significantly. In Figure 5.3 (a), 1.5 mm and 2 mm gap sizes both result in lower TMA concentration levels ( $<10^{-5}$  mol/m<sup>3</sup>), and 1 mm gap yields the highest level ( $>3\times 10^{-5}$  mol/m<sup>3</sup>). Together with Figure 5.3 (b), it is found that intermixing is reversely related to the gap size from 1 mm to 2 mm. Bigger gap spatial ALD reactor has less intermixing, and smaller gap makes the dosing process much longer. As indicated by both figures, it takes much longer time for the spatial ALD process with 1 mm gap to reach the steady state.

The observations are mainly due to the weaker convective mass transfer in smaller gap spatial ALD reactor. With 1 mm gap, for instance, the gas flow is largely hindered by the narrow gap. Considering the fact that in-line spatial ALD is a high vacuum system (0.22 torr), the material transport in such cases is mainly driven by mass and thermal diffusions other than convection. Because mass diffusive effect is much weaker compared to convection, the mass transfer process is much prolonged. These diffused molecules are accumulated in the exhaust cylinder due to lack of convective forces, and consequently a relative higher concentration is resulted in 1 mm gap in-line spatial ALD reactor as shown in Figure 5.3. However, in the case of large gas size, e.g., 5 mm, stronger convective mass transport also increases the intermixing.

At TMA side (position C) as shown in Figure 5.3 (b), a relatively higher intermixing is observed, especially for 1 mm gap size compared to the water side. Water concentration is  $\sim 5\times 10^{-4}$  mol/m<sup>3</sup> at position C. As a comparison, TMA concentration is  $\sim 2\times 10^{-3}$  mol/m<sup>3</sup> with

a relative intermixing ratio (defined as the concentration ratio of the foreign gas to the home gas) 1:4 for 1 mm gap size. This is owing to the fact that water has a relative higher inlet vapor pressure resulting stronger water diffusive process. This is further confirmed by Figure 5.4, which compares the relative intermixing ratio at both sides. As revealed in both Figure 5.3 and 5.4, intermixing is weaker at water side. At both sides, increasing gap size from 1 mm to 2 mm decreases the intermixing.

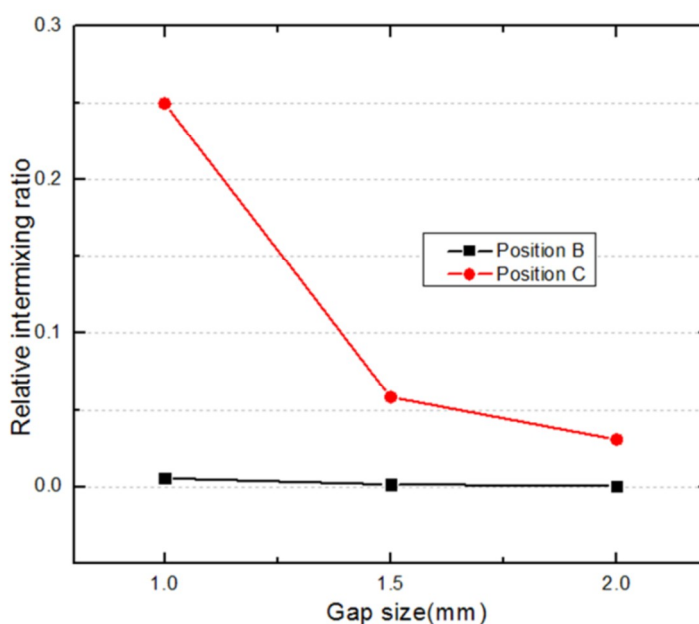


Figure 5.4 Comparison of relative intermixing ratios for position B (water side) and C (TMA side) with different gap sizes, and the relative intermixing ratios is defined as the concentration ratio of the foreign gas to the home gas.

The effect of pumping pressure on material transport is examined by changing the relative pressure (to the base pressure) from 0, 0.05, to 0.1 torr, while the gap size and wafer temperature are fixed at 0.15 mm and 200°C. The values are consider no less than the base pressure because in actual in-line spatial ALD system the pumping pressure is usually a



little higher than the stable base vacuum pressure due to the imperfection of vacuum pump.

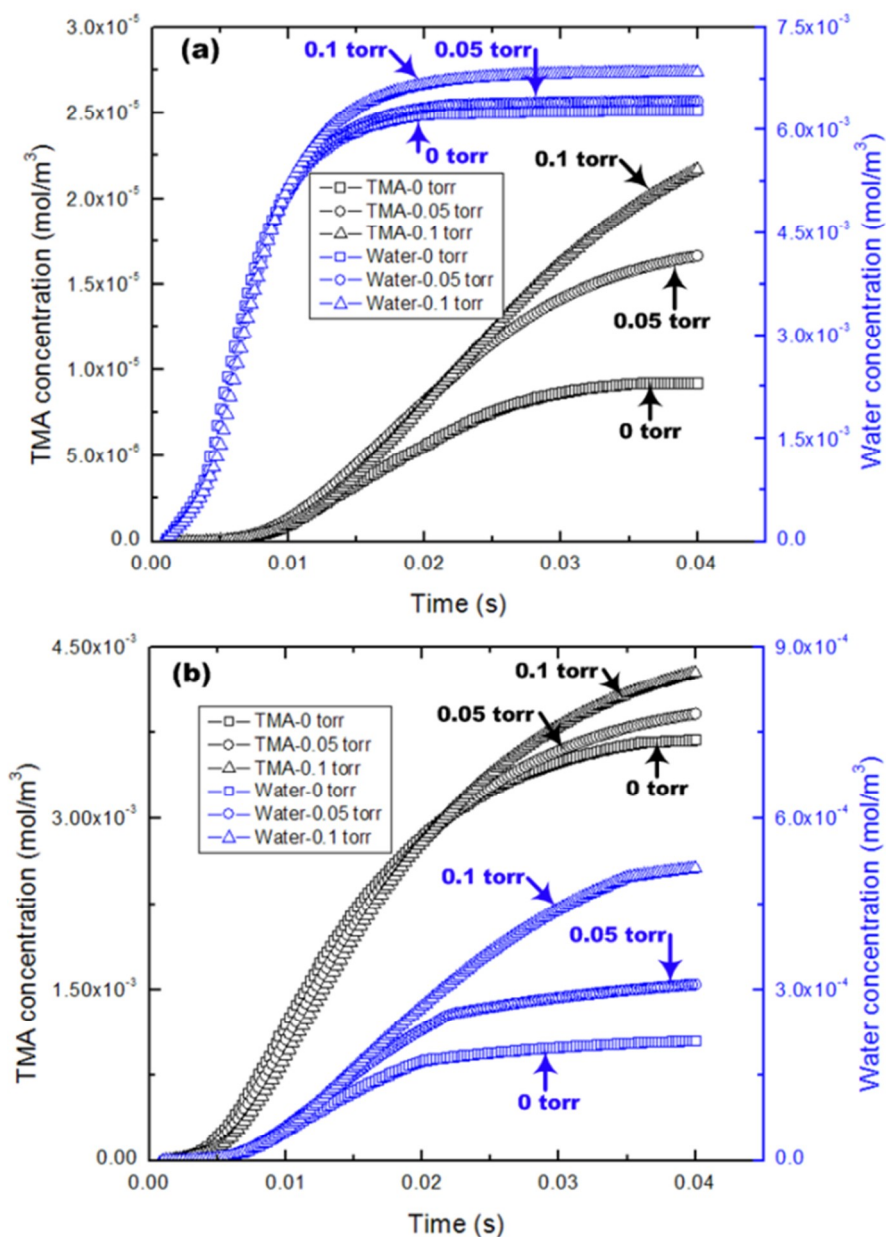


Figure 5.5 The effects of relative pumping pressure (0, 0.05, to 0.1 torr) on the precursor intermixing with gap size and wafer temperature fixed at 1.5 mm and 200°C: (a) TMA and water concentration in mol/m<sup>3</sup> at water side (position B), and (b) at TMA side (position C). The simulation time is 0.04 s with 1.5 mm gap size.

Figure 5.5 presents the effects of pumping pressure on precursor distribution and intermixing for position B and C. It is found that higher pumping pressure (e.g., 0.1 torr)

results in higher TMA concentration at water side (position B) and higher water concentration at TMA side (position C). For instance, water steady concentration level is  $\sim 2 \times 10^{-4}$ ,  $3 \times 10^{-4}$ , and  $5 \times 10^{-4}$  mol/m<sup>3</sup> for 0, 0.05 and 0.1 torr pumping pressure at position C (TMA side), respectively. Hence, properly maintained pumping and base pressure in ALD reactor is crucial to avoid precursor intermixing.

Wafer temperature effects on the flow field and precursor intermixing in in-line spatial ALD reactor are investigated numerically with 1.5 mm gap and 0.22 torr pumping pressure. The results presented in Figure 5.6 show that at both sides higher wafer temperature yields higher precursor concentration level from the other side. With the wafer temperature as high as 250°C, the mass diffusive process is accelerated, and hence higher TMA concentration level is seen at water side (position B) as Figure 5.6 (a), and higher water concentration level at TMA side (position C) as Figure 5.6 (b).

From the above flow and species transport simulations, it's concluded that in the high vacuum in-line spatial ALD system, diffusive mass transfer is the major reason for precursor intermixing, especially in scenarios of very small gap size. As demonstrated by the numerical studies, 1 mm gap size yields highest intermixing level because of the dominant mass diffusive effect. Higher pumping pressure decreases the pressure difference from inlets to outlets, and thus weakens the flow convective effect. The intermixing concentration level is seen lower if the low pumping pressure is well maintained. Because

higher temperature increases the mass diffusion process, it results in higher intermixing concentration level.

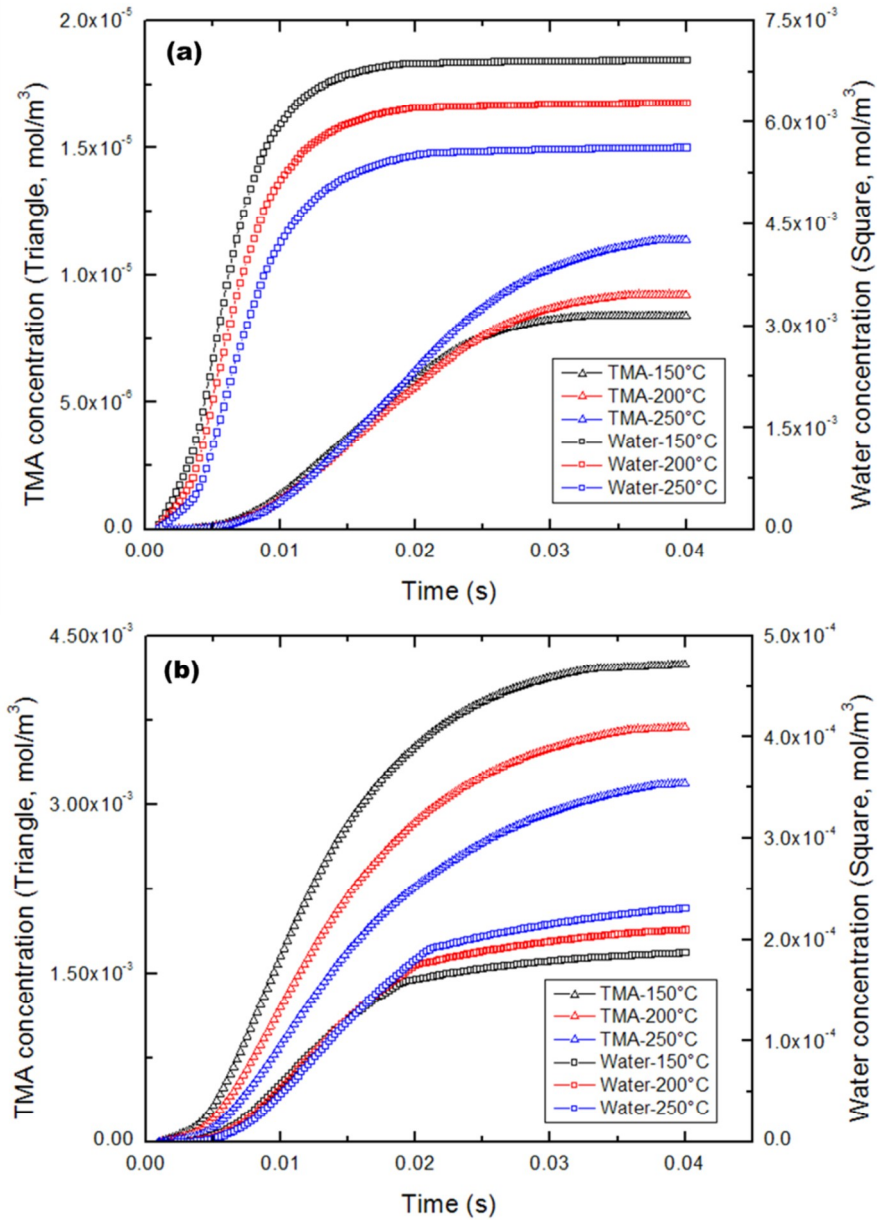


Figure 5.6 The effects of wafer temperature (150°C, 200°C and 250°C) on the precursor intermixing with gap size and pumping pressure fixed at 1.5 mm and 0.22 torr: (a) TMA and water concentration in mol/m<sup>3</sup> at position B (water side), and (b) at position C (TMA side). The simulation time is 0.04 s with 1.5 mm gap size.

In summary, bigger gap (~2 mm), lower pump pressure, and lower wafer temperature are

desirable to minimize the intermixing level in the concerned in-line spatial ALD system. However, the optimal choices of these factors must also be reconsidered in terms of chemical deposition process. For example, lower wafer temperature is beneficial for avoiding intermixing, but it is not favorable for material deposition process, because lower temperature may decrease the film deposition rate. Further numerical investigations on material deposition process are presented in the following section.

#### 5.4.2 Effects on the in-line spatial ALD chemical depositions

The effects of the three factors on the chemical depositions of bulk  $\text{Al}_2\text{O}_3$  in the in-line spatial ALD reactor is studied numerically in terms of growth per cycle (GPC) of thin films on the silicon wafer belt. Bulk  $\text{Al}_2\text{O}_3$  mass growth rate is obtained from integral of the resulted bulk species  $\text{O}(\text{b})$  and  $\text{Al}(\text{b})$ . Thickness growth per cycle in  $\text{\AA}/\text{cycle}$  is then determined by introducing alumina thin film density [Groner, et al., 2004].

Figure 5.7 presents  $\text{Al}_2\text{O}_3$  deposition GPCs under different deposition temperature conditions from 150, 200 to 250°C. The gap size and pumping pressure are set as 1.5 mm and 0.22 torr. From the GPC curves, material depositions are saturated at about 0.015 s dosing time, or the critical dosing time. This critical dosing time is shown sufficient to complete the surface reactions, which completely consume all the reactive surface sites. In this case beyond the critical dosing time, the GPC remains unchanged even if the precursor is still being dosed. This is the very desirable self-limiting feature of ALD process. However,

if dosing is shorter than the critical time, the deposition rate increases rapidly with the precursor dosing time. This is called the unsaturated growth period.

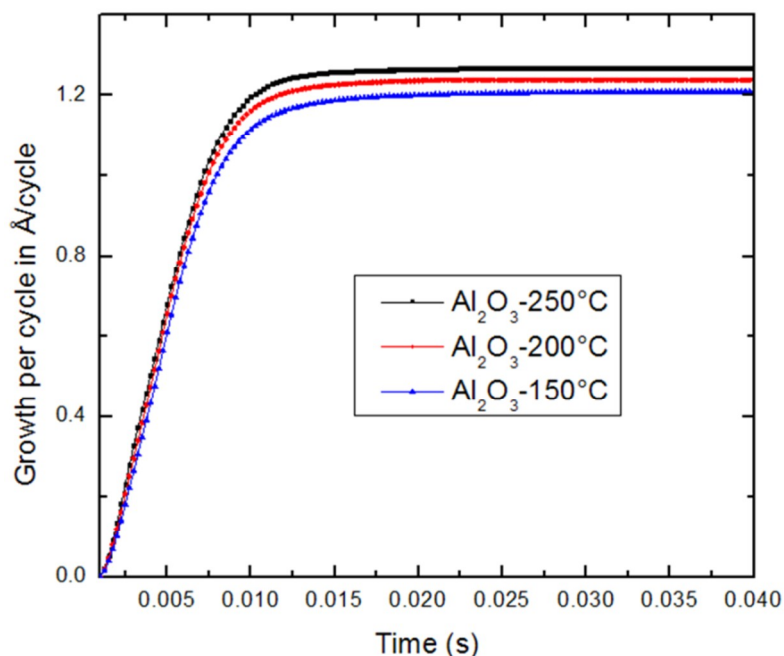


Figure 5.7 Growth per cycle of bulk Al<sub>2</sub>O<sub>3</sub> thin films with different deposition temperatures, 150°C, 200°C and 250°C with 1.5 mm gap size and the ideal pumping condition (0.22 torr).

With the critical dosing time, the wafer belt moving speed is readily to be defined. For a specific point on the wafer belt, it takes 0.015 s to complete the half surface reactions contacting with the precursor molecules under the dosing cylinders. The diameter of precursor dosing cylinder in our in-line spatial ALD reactor is 1 cm, and hence the wafer belt movement speed is promptly calculated as ~0.67 m/s.

The overall throughput of the in-line spatial ALD system can also be achieved from the critical dosing time. For example, as shown in Figure 5.7, GPC at 200°C is ~1.2 Å/cycle, and the critical dosing time is ~0.015 s. Since an ALD cycle takes two half reactions, the

growth thickness per second is calculated using the total cycle time, which is 0.03 s.

$$\text{GPC} = 1.2\text{\AA} / \text{cycle} = 1.2\text{\AA} / 0.03\text{s} = 4\text{nm} / \text{s} \quad (5-3)$$

The overall throughput is significantly improved compared to a few nanometers per minute of growth rate in the conventional ALD system [Poodt, et al., 2010, Poodt, et al., 2013].

By Figure 5.7, it is seen higher temperature does increase the saturated GPC, but the increment is much smaller and even negligible during the unsaturated growth period, i.e., 0 ~ 0.015 s. The numerical simulation results have an excellent agreement with the experimental results of cited work as presented in Ref. [Poodt, et al., 2013]. The temperature effects reveal the chemical kinetic information on the surface reactions. During the surface reactions, the introduced thermal energy has to overcome the reaction barrier (activation energy) to enable the reactions. Higher temperature increases the reactivity of surface species as well as the species molecule kinetic energy, and hence increases the collision probabilities, which finally results in a higher reaction rate.

The effects of gap size on the chemical deposition process are presented in Figure 5.8. It takes much longer dosing time for GPC to get saturated for smaller gap size spatial ALD process. For instance, with 1mm gap size, ~0.025 s dosing is required for GPC to get saturated, compared to ~0.01 s for 2 mm gap. This is mainly attributed to the slower mass transportation process caused by the narrower gap as illustrated in Figure 5.3. From the GPC curves in Figure 5.8, however, 1 mm gap size has a relatively higher saturated GPC

level. Spatial ALD process with 1.5mm gap size has a saturated GPC level as high as 1mm gap size, and requires shorter dosing time ( $\sim 0.012$  s) to get saturated. This shows that the depositions process is highly affected by the flow and mass transfer process.

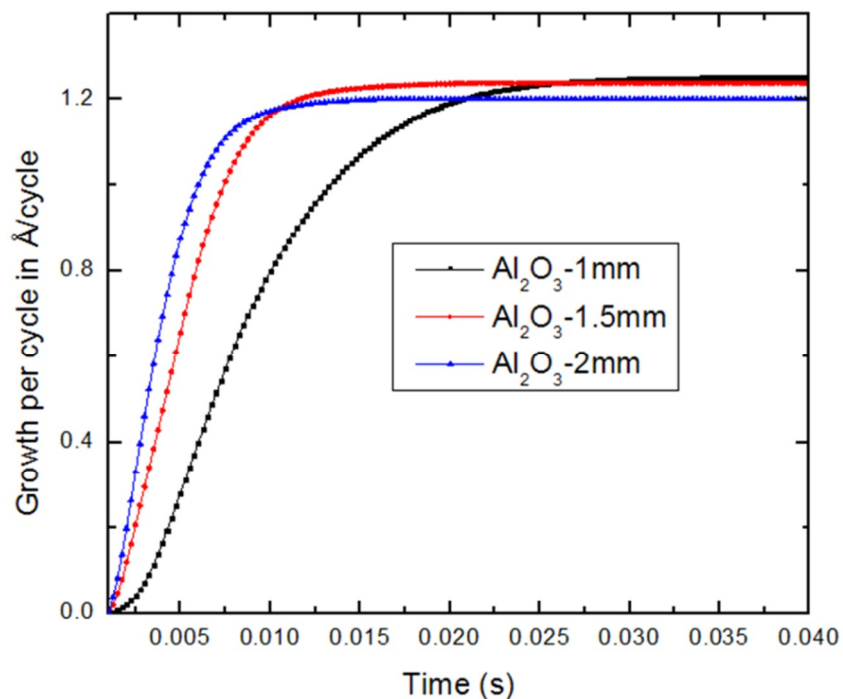


Figure 5.8 Growth per cycle of bulk Al<sub>2</sub>O<sub>3</sub> thin films with different gap sizes 1, 1.5 and 2 mm with ideal pumping condition (0.22 torr) and 200°C wafer temperature.

The effect of pumping pressure on the surface deposition process is shown relatively weaker in Figure 5.9. During the unsaturated growth period before 0.015 s, smaller pumping pressure increases the film deposition rate slightly. Once saturated, they have the same level of GPC. With different pumping conditions on the outlet boundaries, as given by Figure 5.5 the precursor intermixing is altered, but the dominant precursor concentrations are comparable for all the pumping cases. For instance, water concentration difference as shown in Figure 5.5 (a) is within  $1 \times 10^{-3}$  mol/m<sup>3</sup> from 0 to 0.1 torr relative pumping pressure.

This is well correlated with the similar thin film deposition rate as illustrated in Figure 5.9.

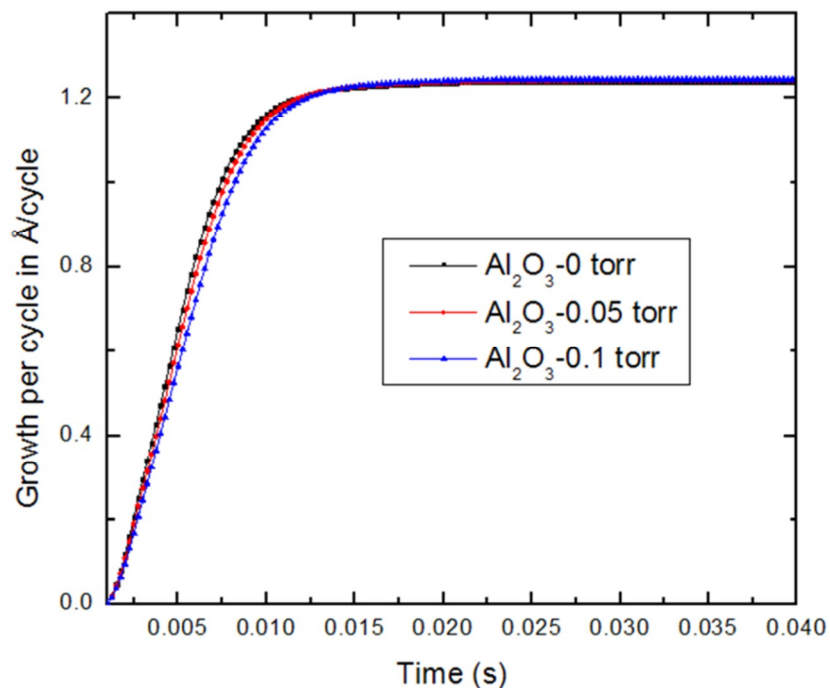


Figure 5.9 Growth per cycle of bulk Al<sub>2</sub>O<sub>3</sub> thin films with different relative pumping pressure (to the base pressure, 0.22 torr) 0, 0.05 and 0.1 torr with 1.5 mm gap size and 200°C wafer temperature.

To depict the overall transient flow and reaction process, Figure 5.10 presents the slice contours of transient flow and deposition process in the in-line spatial ALD reactor at 0.005, 0.015, 0.025 and 0.035 s, respectively for 1 mm gap size, 0.22 torr pumping pressure, and 250°C deposition temperature. The most left cylinder is for water dosing, and the right one for TMA. The left wafer surface under water dosing cylinder shows the half reaction of water dosing, and the right for TMA dosing. At the initial state, the system is full of the separating gas, nitrogen. With dosing proceeds, precursor molecules gradually fill the dosing cylinders. The middle three slice contours show methane generation and distribution in the system. Methane is generated from the both half reactions on the wafer surfaces, and is purged out through the two pumping cylinders. Very few methane can be detected in the



middle separating cylinder during the whole process as shown in Figure 5.10 (c) and (d).

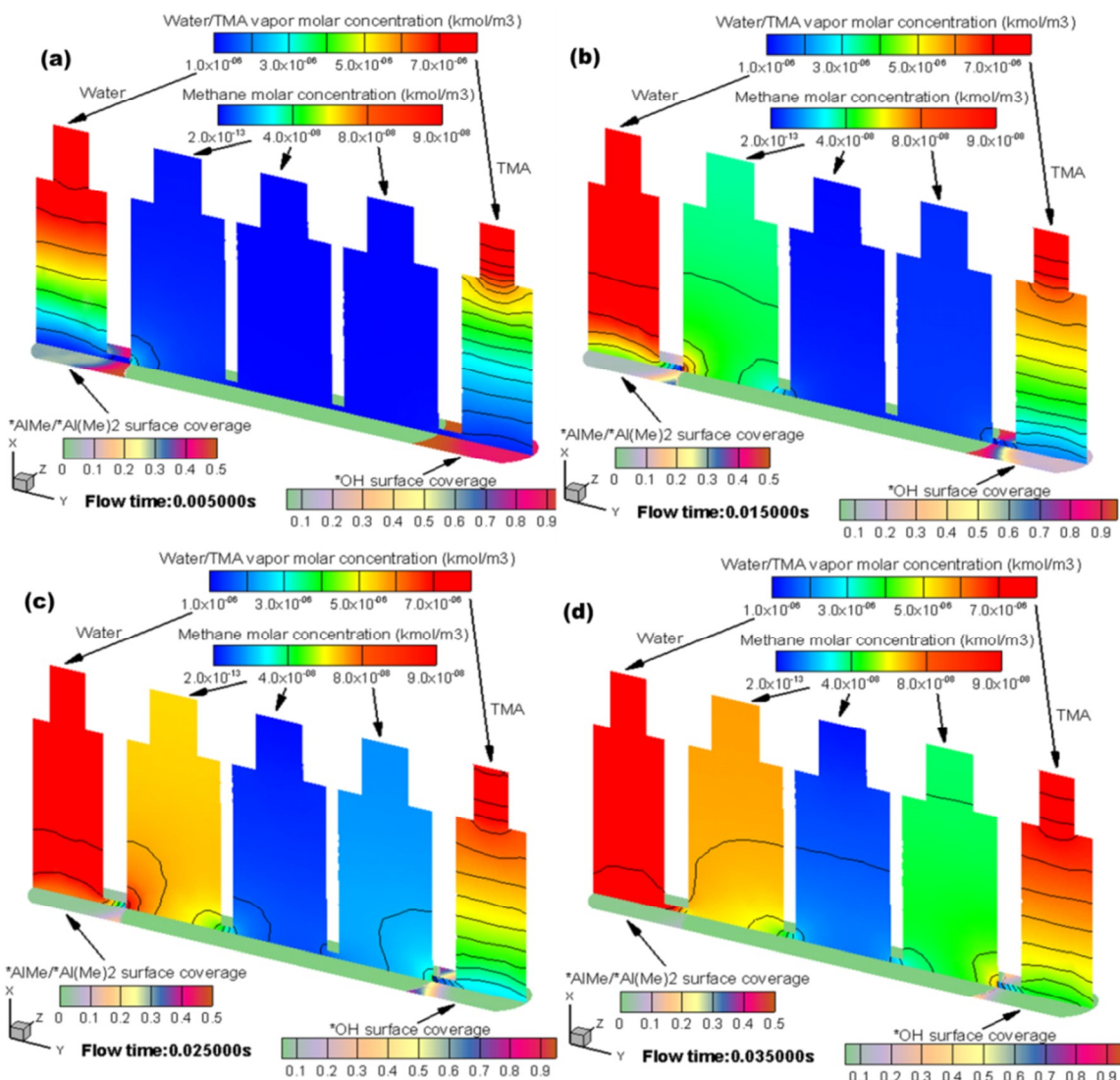


Figure 5.10 Slice contours of transient flow and deposition process in the in-line spatial ALD reactor at 0.005, 0.015, 0.025, and 0.035 s for 1 mm gap size, 0.22 torr pumping pressure, and 250°C wafer temperature.

To summarize the information on the in-line spatial ALD growth process, the deposition is a strictly self-limiting process depending on the reactive surface site status. The film growth is saturated to certain levels within different critical dosing times under different deposition conditions. Demonstrated by the simulation results, the saturated GPC level is heavily

dependent on the wafer temperature, gap size, but rarely on pumping pressure. To be specific, higher wafer temperature (e.g., 250°C), a slightly smaller gap size (e.g., 1.5mm) and better maintained pumping condition (e.g., 0.22 torr) are desirable to achieve higher film growth rate. It is also revealed that the chemical deposition process is highly affected by the flow and concentration conditions of precursors. Surface chemical kinetics of the in-line spatial ALD is a function of deposition temperature, flow conditions, reactive surface sites, and precursor distributions.

## **5.5 Summary and conclusions**

This chapter systematically studied an in-line spatial ALD system by numerical investigations of the gas flow and surface chemical deposition processes in ALD of  $\text{Al}_2\text{O}_3$ . The effects of three geometric and process parameters, namely, gap size, temperature, and pumping pressure, were considered with three levels, respectively. The information on the fluid dynamics in spatial ALD system is crucial to avoid the precursor intermixing. By simulations, it's found that bigger gap (e.g., 2 mm) results in less precursor intermixing. However, when it comes to the surface chemistry, larger gap size generates slightly lower saturated deposition GPC level, despite the critical dosing time is shorter. The optimal gap size is heavily dependent on the geometrical and process parameter setup, as well the trade-off between precursor intermixing and deposition rate.

Wafer temperature is a significant factor in both flow and surface deposition processes.

Higher temperature, 250°C for example, accelerates the diffusive mass transport which largely contributes to the precursor intermixing. However, high temperature also increases the film deposition rate and results in a higher saturated GPC level. Well-maintained pumping pressure is beneficial to decrease the concentration of precursor from the other side, but its effect on the deposition process is seen very weak.

It is also concluded that the time scale of in-line spatial ALD process is only in tens of milliseconds. As demonstrated in our study, the typical critical dosing time of a half cycle in in-line spatial ALD system is  $\sim 0.015$  s, and it only takes 30 milliseconds for a specific point on the moving wafer belt to complete a full deposition cycle. With this critical dosing time, it is possible to define the wafer belt moving speed as  $\sim 0.67$  m/s. Considering the in-line spatial ALD is a continuous process without purging step, the ALD cycle time is greatly shortened, and the overall throughput is shown as high as  $\sim 4$  nm/s, which is much higher compared to the conventional sing-wafer ALD with several nanometers growth in a minute.

# CHAPTER 6 NUMERICAL MODELING AND EXPERIMENTAL INVESTIGATION OF ALD WASTES AND EMISSIONS FOR SUSTAINABLE NANO-MANUFACTURING

## 6.1 Introduction

The serious sustainability issue of the negative environmental impacts of ALD is largely due to the highly toxic chemicals used in the process, greenhouse gas emissions and nano-particle generations [Ma, et al., 2015, Yuan and Dornfeld, 2008, Yuan and Dornfeld, 2010]. Taking  $\text{Al}_2\text{O}_3$  ALD as an example, one of the common precursors, TMA, is extremely flammable and highly toxic, and can cause severe skin and eye damage [Yuan and Dornfeld, 2008, Yuan and Dornfeld, 2010]. The un-reacted TMA molecules are purged out of the ALD system as one of the toxic wastes that pose a high risk to the public health and environment. The by-product, methane, is one of the major greenhouse gases [Yuan and Dornfeld, 2010]. Nano-particles can also be formed in ALD chamber, and the nano-particle emissions might be more hazardous to human health. These wastes and emissions may not be significantly noticeable in a few hundred deposition cycles in lab scale, but considering the large amount of dielectric materials demanded in the semiconductor industry, the amount of ALD wastes and emissions and their potentials to impact the environment can be seriously significant [Yuan and Dornfeld, 2010].

The previous studies show that ALD process features low material utilization efficiency. For instance, in  $\text{Al}_2\text{O}_3$  ALD, only 50.4% of TMA is deposited on wafers by experiments [Yuan

and Dornfeld, 2008, Yuan and Dornfeld, 2010]. ALD process is also shown highly energy-intensive. In  $\text{Al}_2\text{O}_3$  ALD process,  $\sim 4.09\text{MJ}$  energy is consumed for deposition of a 30 nm film [Yuan and Dornfeld, 2010]. Our experimental study on nano-particle emissions in  $\text{Al}_2\text{O}_3$  ALD process show that the total nano-particle emissions with diameter less than 100 nm are in the range of  $6.0 \times 10^5$  and  $2.5 \times 10^6$  particles in 25 cycles of  $\text{Al}_2\text{O}_3$  ALD [Ma, et al., 2015].

This chapter focuses on the gaseous material wastes and emissions in the process of  $\text{Al}_2\text{O}_3$  ALD. To be specific, the deposition process is characterized, and methane emissions in the process are investigated numerically and experimentally. The previously-established ALD numerical model is improved with detailed surface chemical kinetics and reaction mechanisms achieved from DFT calculations [Pan, et al., 2015]. The effects of four process parameters including temperature, pulse time, purge time, and carrier gas flow rate on deposition and material wastes and emissions are investigated systematically using the improved numerical model.

## **6.2 $\text{Al}_2\text{O}_3$ ALD modeling with detailed chemical reaction mechanisms**

### **6.2.1 Physical process modeling**

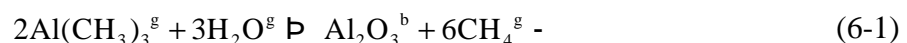
The physical thermal-fluid process of ALD includes momentum transport, mass transport and heat transfer, and the modeling process is described in great detail in our previous chapters. In this chapter, more modeling endeavors are invested in the improvement of

reaction mechanisms and chemical kinetic models.

### 6.2.2 Detailed surface reaction mechanism

The surface chemical kinetics of ALD is of critical importance to characterize the film deposition process, emissions and wastes. However, it is extremely challenging to obtain the detailed information regarding the surface reactions in atomic level by in-situ experimental characterizations [Remmers, et al., 2015]. With great capabilities to obtain the energetic and structural information about the molecular interactions that are essential to understand chemical reactions, computational quantum chemistry approaches such as DFT method provide a satisfactory alternative to study the ALD surface reaction mechanisms and pathways [Remmers, et al., 2015]. Quite a few studies regarding the molecular interactions of Al<sub>2</sub>O<sub>3</sub> ALD using DFT methods have been reported [Delabie, et al., 2012, Elliott and Greer, 2004, Halls and Raghavachari, 2004, Halls and Raghavachari, 2003, Hass, et al., 1998, Remmers, et al., 2015, Widjaja and Musgrave, 2002]. This chapter takes advantage of these DFT reaction calculations and chemical kinetic data to improve our numerical ALD model.

The overall Al<sub>2</sub>O<sub>3</sub> ALD using TMA and water can be expressed as,



where superscripts g and b represent gas and bulk (solid) species, respectively. This overall reaction equation cannot be directly used in the chemical kinetic model because it reveals

nothing regarding the actual ALD pulse process in Al<sub>2</sub>O<sub>3</sub> ALD.

A more complex chemisorption reaction mechanism in Al<sub>2</sub>O<sub>3</sub> ALD depicting the actual sequential ALD pulse and reaction steps is modeled by following two half reactions:



where superscripts \* represents surface site species. These two irreversible equations reveal the actual Al<sub>2</sub>O<sub>3</sub> ALD reaction sequences, and with sufficient chemical kinetic information, this mechanism is proper to simplify and approximate the actual surface reaction and material deposition processes in ALD reactors [Pan, et al., 2015]. However, the above two half reactions hardly include the knowledge regarding the elementary reaction steps as well as the kinetic information of ALD process, which are specially important to model the process wastes and emissions.

With the aid of detailed DFT quantum chemistry calculations, much more detailed chemical deposition mechanisms and pathways of Al<sub>2</sub>O<sub>3</sub> ALD are proposed as illustrated in the following section [Delabie, et al., 2012, Elliott and Greer, 2004, Halls and Raghavachari, 2004, Halls and Raghavachari, 2003, Hass, et al., 1998, Remmers, et al., 2015, Widjaja and Musgrave, 2002].

For the substrate surface initiations, in both our numerical and experimental settings, we use

silicon as substrate, and materials are deposited on the Si (100) surface. In DFT studies, Si<sub>9</sub>H<sub>12</sub> cluster is used to investigate the chemical reactivity and vibrational properties of the Si (100) surface [Halls and Raghavachari, 2004].

Regarding the the initial surface species in Al<sub>2</sub>O<sub>3</sub> ALD, Delabie et al. studied the possible CH<sub>3</sub> and OH terminated surface species on silicon surface using DFT approach [Delabie, et al., 2012]. The cited work shows that the hydrolysis of the SiCH<sub>3</sub> is kinetically unfavorable due to the five coordinated Si atoms in the transition state structure, which makes the following surface reaction with water extremely difficult [Delabie, et al., 2012]. Their studies imply that in actual Al<sub>2</sub>O<sub>3</sub> ALD, it is unlikely to have methyl-covered surface on Si (100) surface. Meanwhile, OH-terminated Si (100) surface reacting with TMA results in experimentally-consistent results. It is reasonable to presume that the silicon surface is hydroxylated with OH groups initially.

In TMA pulse step, with OH-terminated silicon surface, the ALD deposition begins by interacting with gaseous TMA molecules forming a bond between O and Al atoms [Halls and Raghavachari, 2004, Remmers, et al., 2015, Widjaja and Musgrave, 2002]. The formation is reversible and generates an intermediate surface species as shown in Reaction R1.

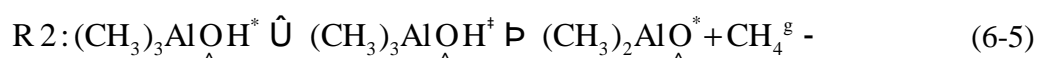


where f and b represent the forward and backward reactions, respectively, and the symbol  $\wedge$



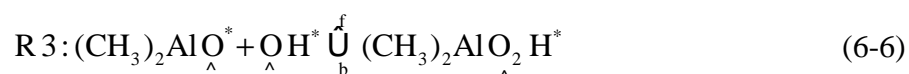
denotes the surface bond linkage with surface group.

The above intermediate surface group  $(\text{CH}_3)_3\text{Al}\overset{\wedge}{\text{O}}\text{H}^*$  further proceeds to a transition state structure by forming a bond between the O atom and an H atom from one of the three methyl ligands, and finally evolves to a more stable structure with two methyl-terminated ligands by releasing a methane molecule. This process is represented by Reaction R2.

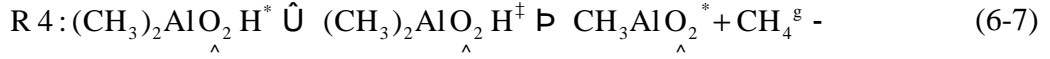


where the superscript  $\ddagger$  represents the transition state. The energy profiles of these two reactions can be found in the cited paper [Halls and Raghavachari, 2004]. The emission of gaseous methane makes this process irreversible.

The energy profile of DFT study [Halls and Raghavachari, 2004] shows that the formed surface species  $(\text{CH}_3)_2\text{Al}\overset{\wedge}{\text{O}}^*$  is in high energy state, and is kinetically inclined to interact with the nearby  $\text{OH}^*$  group resulting an intermediate surface group as shown in following reaction, R3,

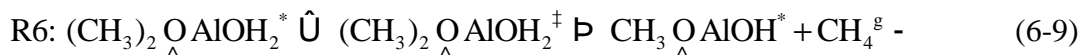
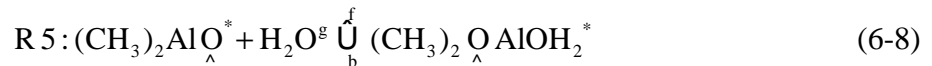


In the complex of  $(\text{CH}_3)_2\text{Al}\overset{\wedge}{\text{O}}_2\text{H}^*$ , a linkage between the Al atom and the hydroxyl O atom is formed. A transition structure is readily formed when the stand-alone hydroxyl H atom is attached to one of the two methyl ligands. As a result, a methane molecule is emitted as shown in Reaction R4.



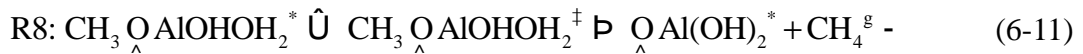
At this point, much more stable species  $\text{AlCH}_3^*$  indicated by the energy profile terminates the surface species evolutions in TMA pulse step. The initial OH-terminated substrate surface in R1 is transformed to  $\text{Al}(\text{CH}_3)_2^*$  by R2, and  $\text{AlCH}_3^*$  by R4, leaving O and Al atoms anchored in the formed surface structures. Since the double-methyl-mounted species ( $\text{Al}(\text{CH}_3)_2^*$ ) is kinetically unstable, the most part of the final substrate surface after TMA pulse is likely covered by  $\text{AlCH}_3^*$  with only a smaller number of  $\text{Al}(\text{CH}_3)_2^*$ .

For water pulse step, due to the coexistence of the two possible methyl-terminated surface species, the surface reaction mechanisms are two-fold. In the case of the double-methyl-terminated species  $\text{Al}(\text{CH}_3)_2^*$ , a water molecule is chemisorbed by the Al atom resulting two stand-alone H atoms as shown in Reaction R5. One of the H atoms is attracted by the C atom of the methyl group resulting in a temporary O-H-C linkage. The transitional bond is finally broken at the O-H bond leaving the surface site terminated with a heterogeneous mixture of OH and  $\text{CH}_3$ . Presented in Reaction R6, a methane molecule is emitted in the process.



Contacting with another water molecule, the surface site further evolves to an intermediate

structure denoted as  $\text{CH}_3\underset{\wedge}{\text{O}}\text{AlOH}_2^*$  shown in the following Reaction R7. A transition state structure is further generated in R8 when a similar transitional O-H-C bond is formed. The transition state structure  $\text{CH}_3\underset{\wedge}{\text{O}}\text{AlOH}_2^\ddagger$  is the barrier before reaching the final stable OH-terminated structure.



With breakage of the transitional bond, a methane molecule is generated, which leaves the surface sites fully covered by two OH groups. The structure has no more place for extra water molecules, and the transformation of the double-methyl-terminated species  $\text{Al}(\text{CH}_3)_2^*$  to double-hydroxyl-terminated species  $\text{Al}(\text{OH})_2^*$  is finalized.

The process of single-methyl-terminated species  $\text{AlCH}_3^*$  interacting with water molecules is similar and presented in the following Reactions R9 and R10.



Water molecule is firstly adsorbed by the Al atom resulting in an intermediate species denoted as  $\text{CH}_3\underset{\wedge}{\text{Al}}\text{OH}_2^*$ . With extra energy, the species further evolves into a transition state structure by forming the O-H-C bond. The excited structure is finally transformed to a single-hydroxyl-terminated species by emitting a methane molecule. During the process, an extra Al-O is formed.

As described in the above deposition reactions R1-R10, the ALD deposition process is actually involved with the transformations of different surface species. TMA pulse leaves the substrate surface with O-Al bonds and methyl-terminated surface sites, which are further converted in water pulse by forming Al-O bonds leaving the surface covered by hydroxyl-terminated sites. Within one ALD cycle, the silicon surface is reconstructed with the O-Al-O bonds which represents a single layer of Al<sub>2</sub>O<sub>3</sub> film. Revealed by the DFT energy profiles of the mechanisms [Delabie, et al., 2012, Elliott and Greer, 2004, Halls and Raghavachari, 2004, Hass, et al., 1998, Widjaja and Musgrave, 2002], the success of these atomic-level transformations heavily depends on the energy conditions, the availability of gaseous species and surface species. The reaction conditions are defined by the macro-level process parameters, such as the temperature, precursor distributions.

### 6.2.3 Surface chemical kinetics

For an irreversible reaction, the reaction rate constant of  $r$ th surface reaction is determined by the Arrhenius expression,

$$k_r = A \exp\left(-\frac{E_a}{RT}\right) \quad (6-14)$$

where  $A$  is the pre-exponential factor,  $E_a$  is the activation energy,  $T$  is temperature in K, and  $R$  is the universal gas constant.

The pre-exponential factor, also known as the frequency factor represents the frequency of collisions between reactant molecules. It is practically unfeasible to obtain the pre-exponential factor empirically by experiments in our case, and the collision theory estimation is not accurate for gas-solid surface interactions [Atkins and de Paula, 2011, Chang, 2005]. The transition state theory gives more accurate representation of the pre-exponential factor through the Eyring equation [Chang, 2005]. Detailed derivations of the following expression for pre-exponential factor can be found in the cited literatures [Chang, 2005, Davis and Davis, 2012].

$$A = \frac{k_B T}{h} \exp\left(\frac{\Delta S_0^\ddagger}{R}\right) \quad (6-15)$$

where  $h$  and  $k_B$  are Planck's constant and Boltzmann's constant, respectively.  $\Delta S_0^\ddagger$  is the change in standard entropy of forming the transition state.

The activation energy in Arrhenius expression is the change in standard enthalpy of forming the transition state as following,

$$E_a = \Delta H_0^\ddagger \quad (6-16)$$

The activation energy is the energy barrier which can be characterized from the energy profiles achieved from DFT calculations, while entropy change  $\Delta S_0^\ddagger$  is evaluated through the equilibrium constant of forming the transition state, which is expressed as [Davis and Davis, 2012],

$$\Delta S_0^\ddagger = R \ln K^\ddagger + \frac{\Delta H_0^\ddagger}{T} \quad (6-17)$$

where the equilibrium constant is computed using statistical mechanics methods and the

molecular partition functions [Remmers, et al., 2015].

The backward reaction constant  $k_b$  in the ALD reversible reactions are evaluated by the equilibrium constant  $K$ ,

$$k_b = \frac{k_f}{K} \quad (6-18)$$

The equilibrium constants pertaining to these ALD reactions are listed in the cited reference [Remmers, et al., 2015]. The reaction energy data such as change of enthalpy can be found in the cited DFT studies [Delabie, et al., 2012, Elliott and Greer, 2004, Halls and Raghavachari, 2004, Hass, et al., 1998, Widjaja and Musgrave, 2002].

With the improved ALD chemical kinetic model, three levels of four process parameters, temperature (150°C, 200°C and 250°C), pulse time (0.015, 0.02, and 0.025 s), purge time (5, 10 and 15 s) and carrier gas flow rate (10, 20 and 30 sccm) are simulated to study their effects on the surface deposition, process wastes and emissions.

### 6.3 Experiments

Based on the same ALD system in the numerical model, experiments of characterizing the surface reaction process and emissions in Al<sub>2</sub>O<sub>3</sub> ALD are carried out in the Cambridge NanoTech Savannah 100 ALD reactor. To benchmark the numerical model especially the chemical kinetics in terms of film growth rate, Al<sub>2</sub>O<sub>3</sub> films are deposited on substrates of Si using 99.9% TMA and 99.0% distilled water under three levels of deposition temperatures,

150°C, 200°C and 250°C. The ALD cycle starts with 300 seconds stabilization, followed by 0.02 s pulse and 10 s purge procedures for both TMA and water. The Al<sub>2</sub>O<sub>3</sub> films are deposited with 500 cycles, and the film thickness is characterized by the UVISEL Spectroscopic Ellipsometer (HORIBA, Ltd.).

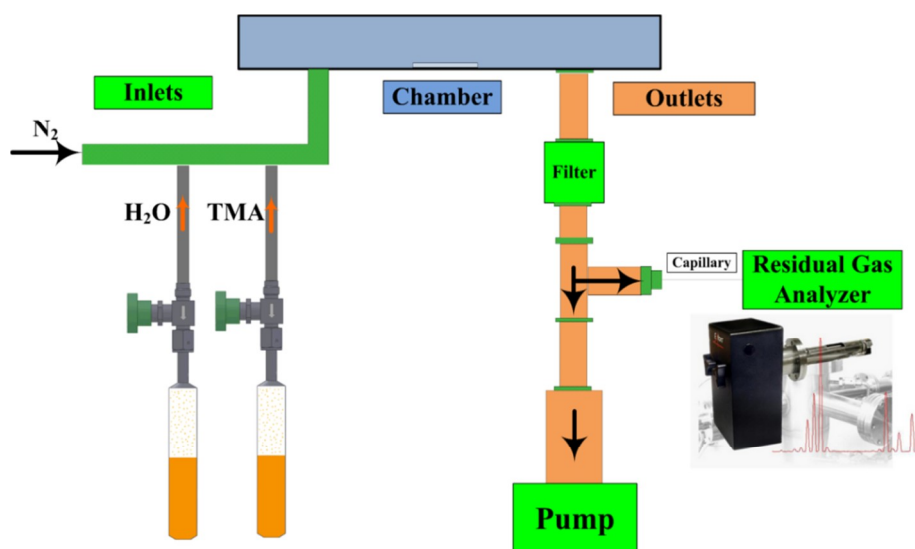


Figure 6.1 Experimental ALD system with residual gas analyzer (RGA) to characterize the methane emissions.

In the proceeding of ALD cycles, an in-situ gas analyzer is used to characterize methane emissions in Al<sub>2</sub>O<sub>3</sub> ALD as shown in the scheme of Figure 6.1. Precursors stored in separate cylinders are injected sequentially into the ALD chamber when the corresponding ALD valve is open. Si wafers with 10 mm by 20 mm are placed in the center of the chamber. A residual gas analyzer (Extorr XT Series RGA) is connected in the outlet after a gas particulate filter with 100 nm pore size filter element. The emissions are sampled through a capillary tube into the RGA device. In our specific experimental setup, due to the possible condensation of water vapor in the cooler outlet and RGA tubing, and considering the

possible reactions of TMA wastes with the condensed water, it is extremely difficult to accurately characterize either TMA waste or water vapor in our ALD system. In our experiments, we particularly focus on methane emissions.

## 6.4 Results and discussion

### 6.4.1 Al<sub>2</sub>O<sub>3</sub> ALD deposition process

Using the reaction mechanisms and the chemical kinetic model, a full cycle of Al<sub>2</sub>O<sub>3</sub> ALD with 0.02 s pulse and 10 s purge is simulated with the chamber temperature 200°C. The contour plots of gaseous species distributions and the bulk species deposition rates in the entire ALD system are presented in Figure 6.2 (a) and (b) at the end of the two pulse steps, 0.02 s and 10.04 s, respectively, and Figure 6.3 shows the gaseous species distributions in the full ALD cycle with the data probed in the center area of the ALD chamber.

At the initial state, only carrier gas N<sub>2</sub> exists in the chamber. As the ALD valve is open for TMA pulse, TMA concentration increases steadily, while N<sub>2</sub> concentration decreases as seen in Figure 6.3. The increasing methane concentration shows the surface reactions are activated and material deposition is initiated. Methane concentration reaches its peak during the 0.02 s pulse step and declines slightly after that. The declined methane concentration is mainly due to the fact that the reaction rate decreases as the reactive surface sites OH\* is being consumed.



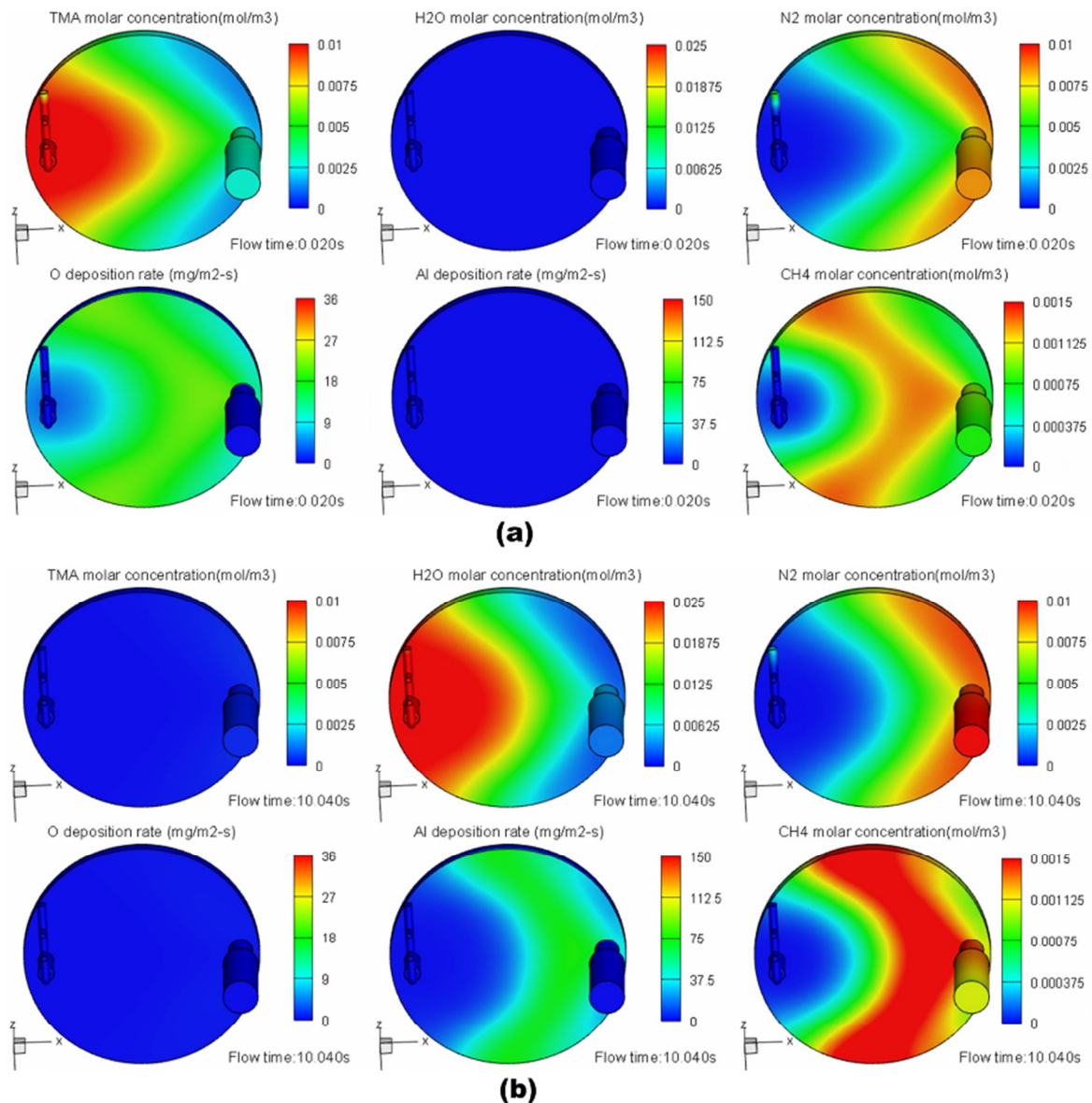


Figure 6.2 Contour plots of gaseous species distributions and the bulk species deposition rates (a) 0.02 s at the end of TMA pulse and (b) 10.04 s at the end of water pulse.

Methane generation rate is further decreased as the TMA pulse process ends. As TMA concentration declines during the purge step, the low level of methane concentration in the center area of chamber is maintained by the TMA residuals during the first half of purge step. The increasing carrier gas concentration shows that N<sub>2</sub> dominates the chamber space again during the purge step. The materials are not evenly distributed in the entire ALD

geometry, and along the flow field, the inlet area encounters the precursor flow first as shown in Figure 6.2.

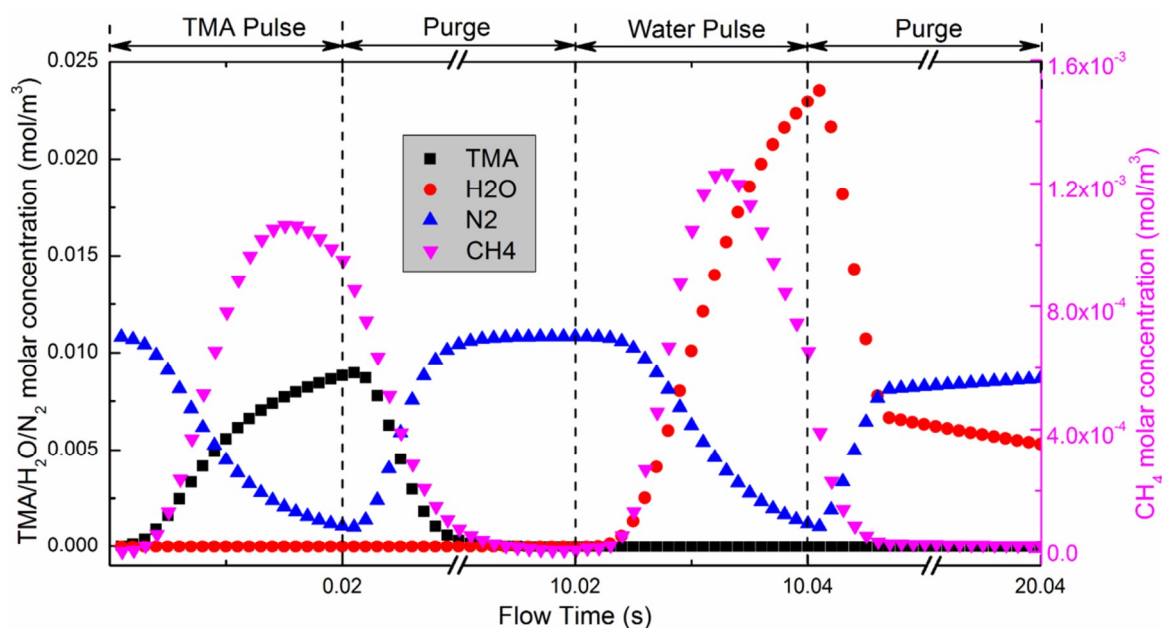


Figure 6.3 Gaseous species distributions during the full ALD cycle.

The material concentrations in water pulse process have the similar variations as seen in TMA pulse step. As water is being injected into the chamber, methane concentration increases steadily and reaches a higher peak. In the second purge process, as water concentration declines promptly, much less methane can be detected in the center area. The gaseous material distribution variations in the center area are profoundly related to the surface species coverage as presented in Figure 6.4. The contour plots of surface coverage and precursor distributions in the entire ALD system for TMA and water pulse steps are shown in Figure 6.5 (a) and (b), respectively. A full coverage of OH\* is assumed initially, and its coverage declines slightly in the first few milliseconds as shown in Figure 6.4, and decreases promptly following that, until it reaches ~ 20% at the end of the TMA pulse step.

To be specific, 21.8% OH\* species are left on the surface and are further consumed in the following purge step. This indicates that within TMA pulse step, the surface reactions are not saturated as also shown by the contour plots in Figure 6.5 (a), especially in the outlet area. Part of surface reactions is completed during the following purge step.

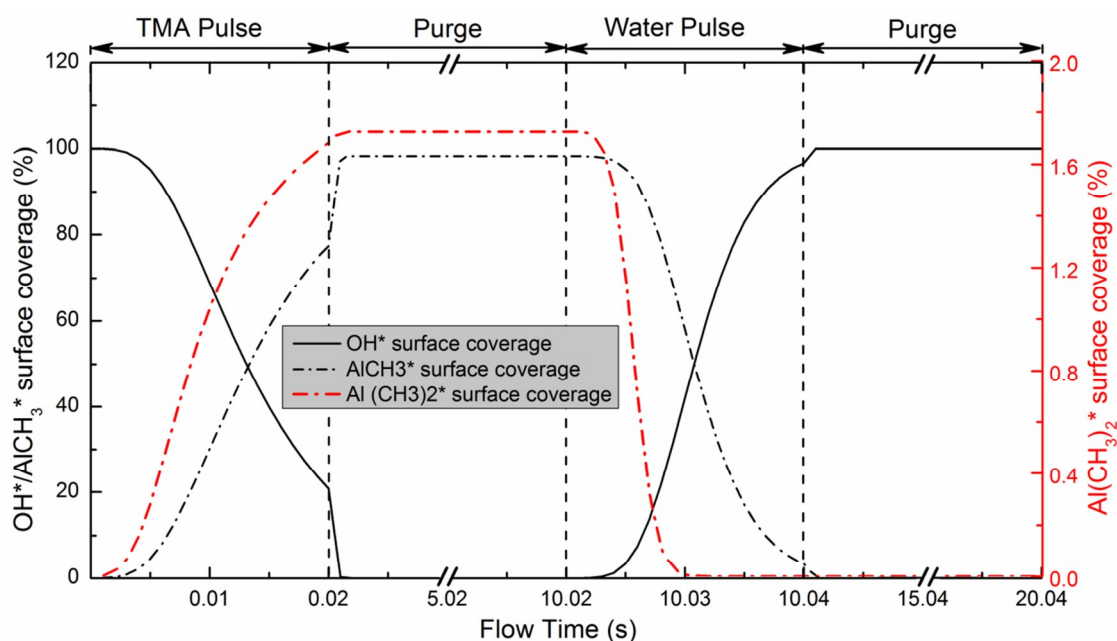


Figure 6.4 Surface coverage for the main surface species during the full ALD cycle.

Meanwhile, the two types of methyl-terminated species, Al(CH<sub>3</sub>)<sub>2</sub>\* and AlCH<sub>3</sub>\* are being generated on the surface. At the end of TMA pulse step as shown in Figure 6.5 (a), the majority of the surface area is covered by AlCH<sub>3</sub>\* (~ 77.5% in the center area), while only ~ 1.7% is covered by Al(CH<sub>3</sub>)<sub>2</sub>\*. Other intermediate surface species involved in R1-R10 have much lower level coverage (in the level of 10<sup>-6</sup>) as indicated in Figure 6.5. This is consistent with conclusion from DFT studies that Al(CH<sub>3</sub>)<sub>2</sub>\* is not stable [Halls and Raghavachari, 2004]. At the end of the first purge step, 98% substrate surface in the center area is covered by AlCH<sub>3</sub>\* and less than 2% is covered by Al(CH<sub>3</sub>)<sub>2</sub>\*. In water pulse, these two

methyl-terminated surface species are converted back to OH\* species as shown in Figure 6.4 and Figure 6.5 (b). At the end of pulse process, ~ 96.7% surface sites are covered by hydroxyl-terminated species. A very small portion of surface reactions are completed in the second purge step.

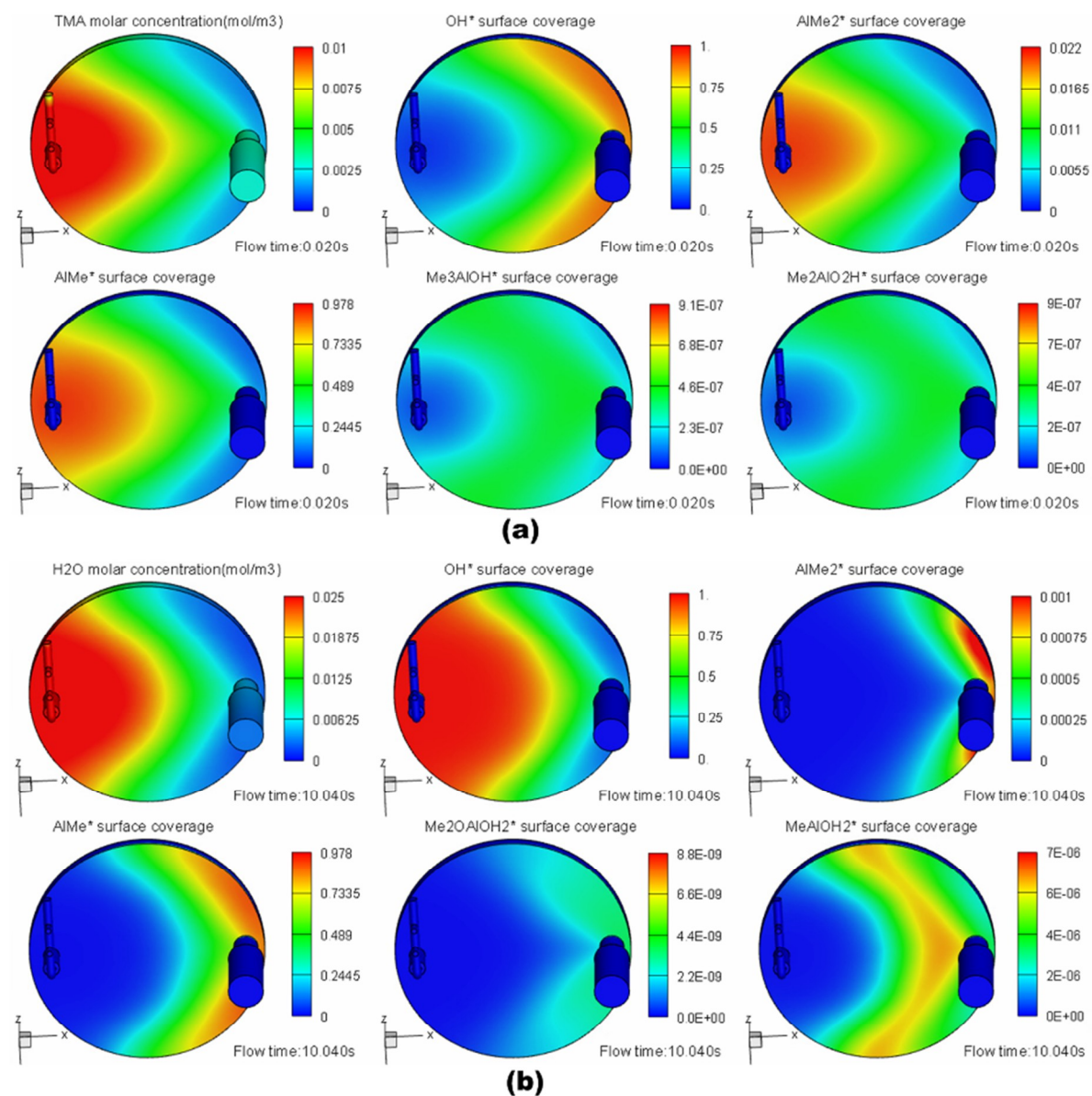


Figure 6.5 Contour plots of surface coverage and precursor distributions in the entire ALD system (a) 0.02 s at the end of TMA pulse and (b) 10.04 s at the end of water pulse.

Figure 6.6 presents the bulk species deposition rate correlated with precursor concentrations

during the full ALD cycle in the center area. It's found that the bulk species deposition rate is proportional to the corresponding precursor concentration. As shown in Figure 6.6, both of the Al and O deposition rates take the parabolic shape with peak values in the pulse process. This is due to the fact that deposition process is not only dependent on the gaseous species concentration, but also influenced by the reactive surface species. Although the precursor concentrations are increasing during the pulse steps, the increased deposition rate is balanced by the decreasing reactive surface sites.

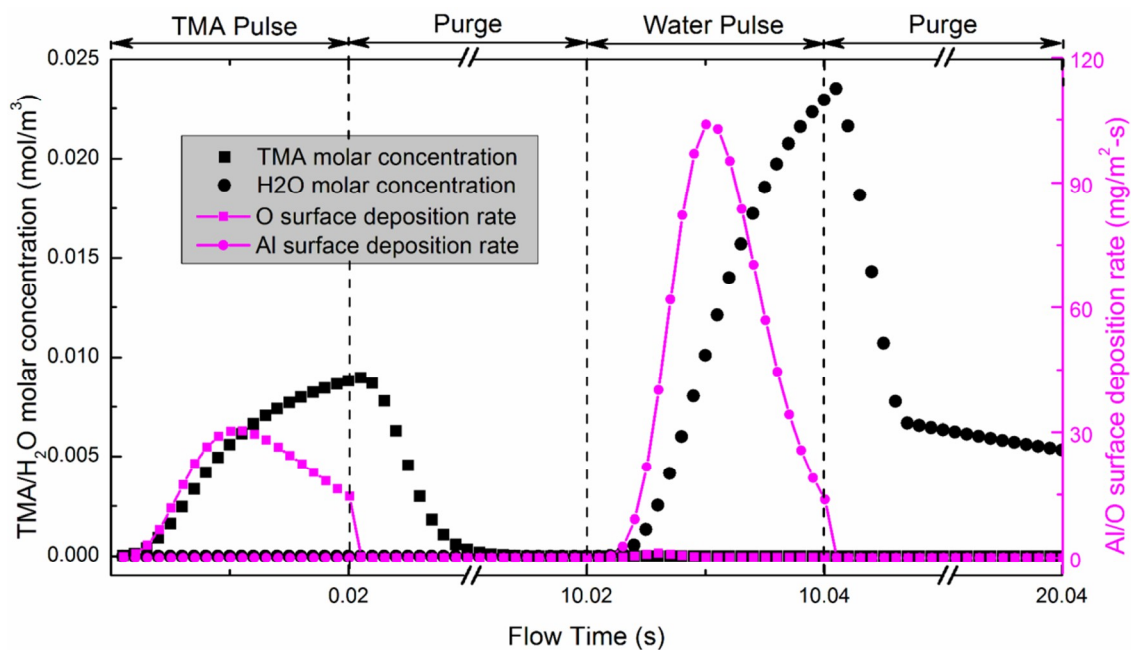


Figure 6.6 Correlation of the bulk species deposition rate and precursors concentration during the ALD cycle.

Together with the analysis of the elementary chemical reactions in the previous section, the full-cycle ALD simulations confirm that the processes of the chemisorption of the gaseous species and conversion of the surface species bulk material depositions in ALD.

Accompanying the deposition process, methane emissions are generated, and process wastes are released. The actual deposition process is heavily dependent on interactions of the gaseous, surface and bulk species, which are essentially influenced by the process parameters such as temperature, pulse and purge procedures as well as the carrier gas flow rate. In the section that follows, these influential factors are investigated systematically.

#### 6.4.2 Effects of process parameters on ALD wastes and emissions

In this section, the four process parameters, temperature, pulse time, purge time, and carrier gas flow rate are specially investigated to explore their effects on the gaseous wastes and emissions. The objective of the effect studies is to minimize the negative environmental impacts such as wastes and emissions while maintaining a high material deposition rate in the concerned ALD process.

Temperature is an essential factor in ALD chemical process defined in the Arrhenius equation(6-14). Same as experimental settings, the inlet and outlet tubing of numerical model is heated to 150°C, and chamber temperature is adjusted in three levels of 150°C, 200°C and 250°C. The effects of chamber temperature on total precursor dosage, precursor wastes and methane emissions are presented in Figure 6.7 with 0.02/10/0.02/10 s ALD cycle and 30 sccm carrier gas flow rate. The experimental results are also plotted in Figure 6.7 to benchmark the numerical results. It is found that precursor dosage is barely affected by the process temperature. In fact, precursor dosage is mainly determined by the pressure



difference between precursor cylinder and the vacuum chamber, which is rarely influenced by the chamber temperature [Pan, et al., 2015].

As described in the reaction mechanisms, methane emissions are closely pertinent to the deposition process. The actual ALD involves both chemisorption and desorption or decomposition (backward reactions). Higher temperature of 200°C accelerates both chemisorption and desorption, but the overall effect as shown by the results in Figure 6.7 is the enhancement of chemisorption process. As a result, methane emissions are increased as shown in Figure 6.7 (a) from 150°C to 200°C. This is consistent with the film growth rate presented in Figure 6.7 (b). When the chamber is further heated to 250°C, however, the growth rate is shown decreased in both experimental and numerical results.

This is largely because the enhanced desorption process dominates over the chemisorption at higher temperature of 250°C. Taking Reactions R1 and R5 as examples, the extra energy at 250°C in the system can be sufficient to overcome the energy barriers of the reverse reactions which are 0.6 eV and 0.85 eV for R1 and R5, respectively [Halls and Raghavachari, 2004]. This leads to the breakage of the formed O-Al bond in R1 and Al-O bond in R5.

With the enhanced desorption process, surface reactions cannot proceed to form O or Al atom depositions on the substrate surface, and as an undesirable result, the precursor

molecules are returned to chamber and purged out as wastes. As shown in Figure 6.7 (a), the total precursor wastes are increased at 250°C from 200°C. Presented in Figure 6.7 (b), the precursor wastes are reversely related to the deposition rate.

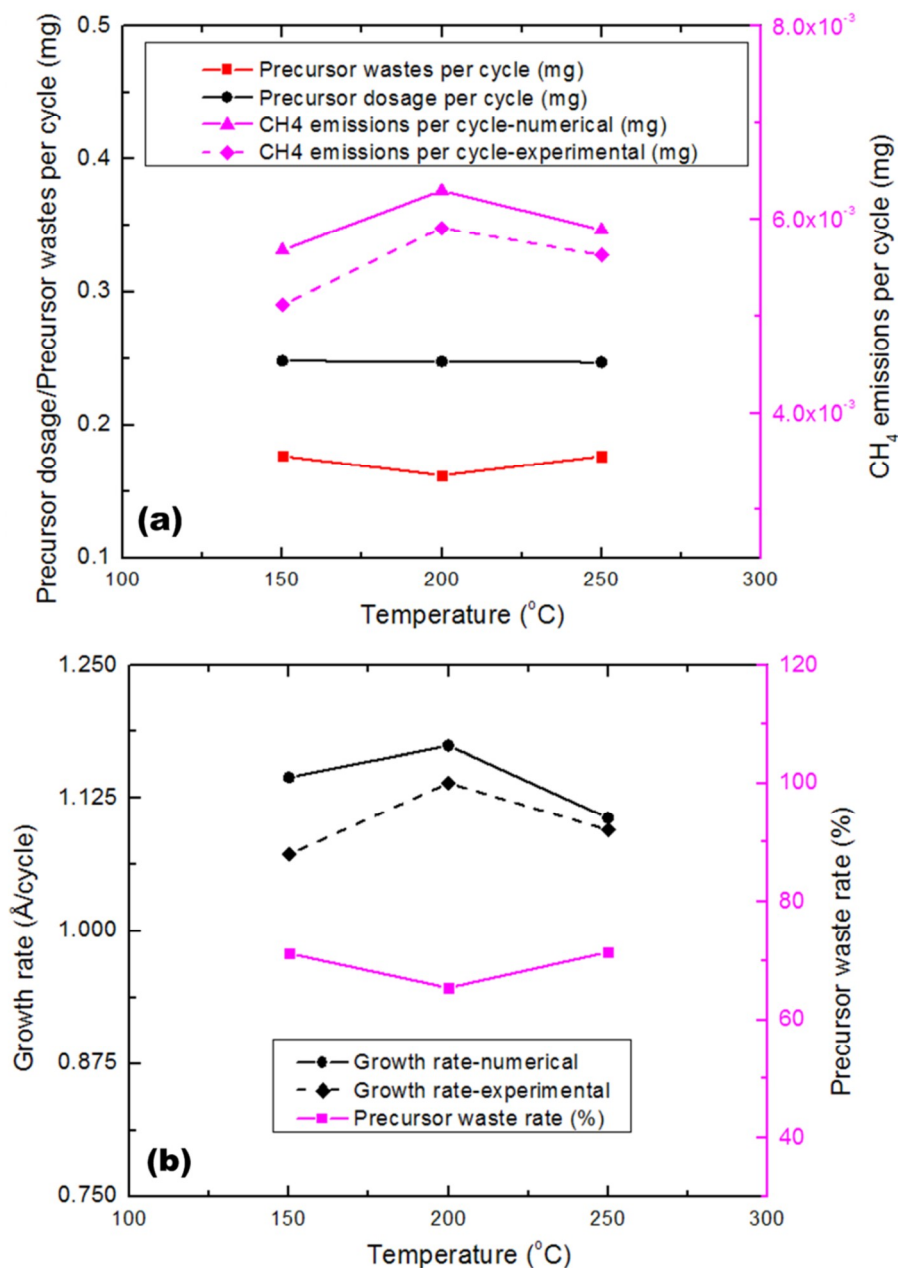


Figure 6.7 Effects of chamber temperatures on the process wastes and emissions (a) precursor dosage, precursor wastes and methane emissions and (b) film growth rate and precursor waste rate.

The experimental data of methane emission in 500 cycles of depositions are also plotted to



benchmark the numerical results in Figure 6.7. As an overall remark on the effects of temperature in terms of material deposition, wastes and emissions, the results show that at moderate temperature of 200°C, more precursors are utilized for film depositions with the lowest precursor waste rate (65.4%), and in the meantime, the highest growth rate of 1.17 Å/cycle is achieved.

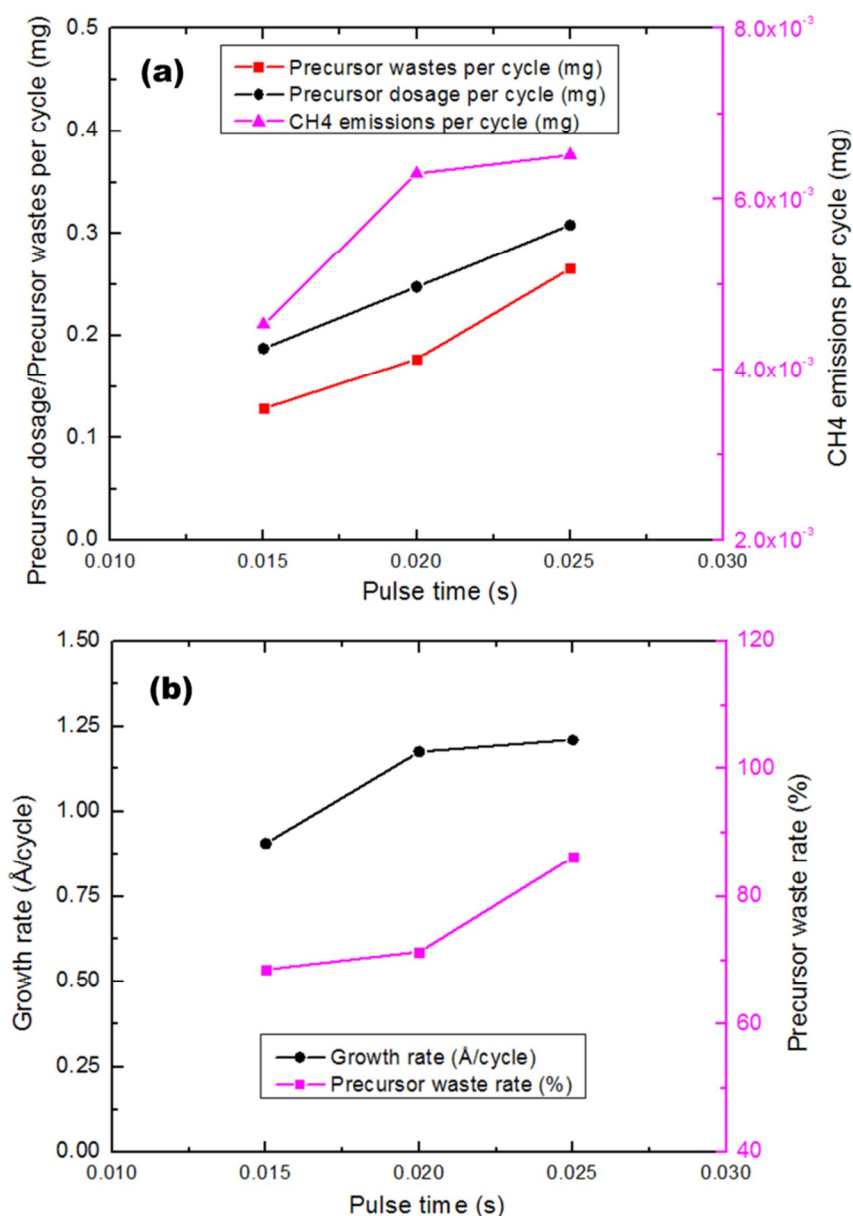


Figure 6.8 Effects of pulse time on the process wastes and emissions (a) precursor dosage, precursor wastes and methane emissions and (b) film growth rate and precursor waste rate.

Precursor dosage is directly proportional to the pulse time as shown in Figure 6.8, in which ALD process is simulated at three levels of pulse time 0.015 s, 0.02 s and 0.025 s with 10 s purge time at 200°C and 30 sccm carrier gas flow rate. Driven by the pressure difference, the precursor dosage in one ALD cycle is increased from 0.187 mg to 0.308 mg as pulse time is prolonged from 0.015 s to 0.025 s. With more precursor molecules injected into the reactor, the reactions are driven to the forward direction, and the reverse reactions are restrained, which results in more material depositions and methane generations. As shown in Figure 6.8 (a), methane emissions per cycle are increased from  $4.5 \times 10^{-3}$  mg to  $6.3 \times 10^{-3}$  mg, and meanwhile, the growth rate presented in Figure 6.8 (b) is significantly increased from 0.91 Å/cycle to 1.17 Å/cycle when the pulse time is increased to 0.02 s from 0.015 s.

When pulse time is further increased to 0.025 s, slight increments are seen for both methane emissions and growth rate. In the case of 0.025 s pulse time when too much precursor is supplied to the substrate surface, these extra materials cannot be absorbed in a limited time, and are finally purged out of the system due to the possible saturation of the surface reactions. As revealed in Figure 6.8 (a), a significant increment of precursor wastes is observed at 0.025 s pulse. In such a condition, precursors are greatly overdosed, and this seriously deteriorates the sustainability performance of ALD. As presented in Figure 6.8 (b), the precursor waste rate is as high as 86.2% at 0.025 s pulse time compared to 70% of 0.02 s. Fewer precursors are wasted at 0.015 s pulse time, but the growth rate is low, only 0.91 Å/cycle as shown in Figure 6.8 (b). As a trade-off, 0.02 s might be the optimal value for

pulse time which yields higher growth rate with a relatively higher material usage efficiency.

Figure 6.9 shows the effects of purge time on the process wastes and emissions at three levels (5 s, 10 s and 15 s) with 0.02 s pulse time at 200°C and 30 sccm carrier gas flow rate. The effect of purge time on precursor dosage is very weak as shown in Figure 6.9 (a), while it increases the precursor wastes especially from 5 s purging time to 10 s. With longer purge time, more precursor residuals in the chamber are purged by the carrier gas. As the majority of precursor residuals are cleaned within 10 s, there is no evident increase in the precursor wastes with 15 s purge.

Methane emissions are increased from 5 s purge time to 10 s and a slightly increment is seen at 15 s as shown in Figure 6.9 (a). The similar effect of purge time on material deposition rate is observed in Figure 6.9 (b). Methane generation is positively related to the material deposition process, and longer purge time implies more surface reactions on the substrate surface due to the longer contact of precursor molecules with the surface sites. As a result, the growth rate is increased from 1.15 Å/cycle with 5 s purge time to 1.17 Å/cycle with 10 s.

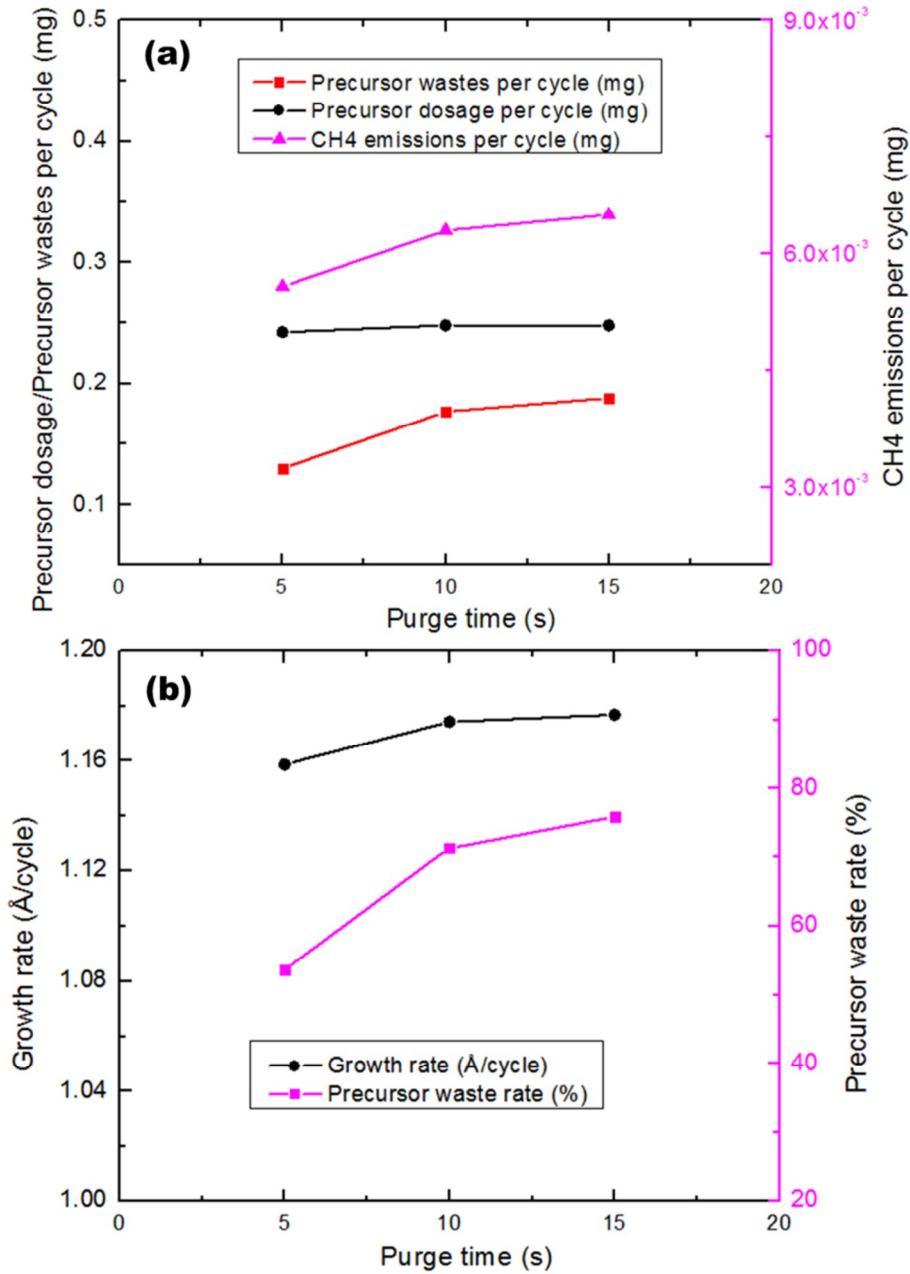


Figure 6.9 Effects of purge time on the process wastes and emissions (a) precursor dosage, precursor wastes and methane emissions and (b) film growth rate and precursor waste rate.

When the purge process is further prolonged to 15 s, the growth rate is seen at the same level as 10 s. This is mainly due to the fact that in the first 10 s, the majority of the reactive surface species has been consumed. Lack of reactive surface species has inhibited the material chemisorption. The material waste rate shown in Figure 6.9 (b) is higher in longer

purge process. From the results in Figure 6.9, shorter purge process, e.g., 5 s, generates fewer precursor wastes, but also results in lower growth rate. With both deposition throughput and sustainability performance taken into account, 10 s might be the optimal choice for the purge time.

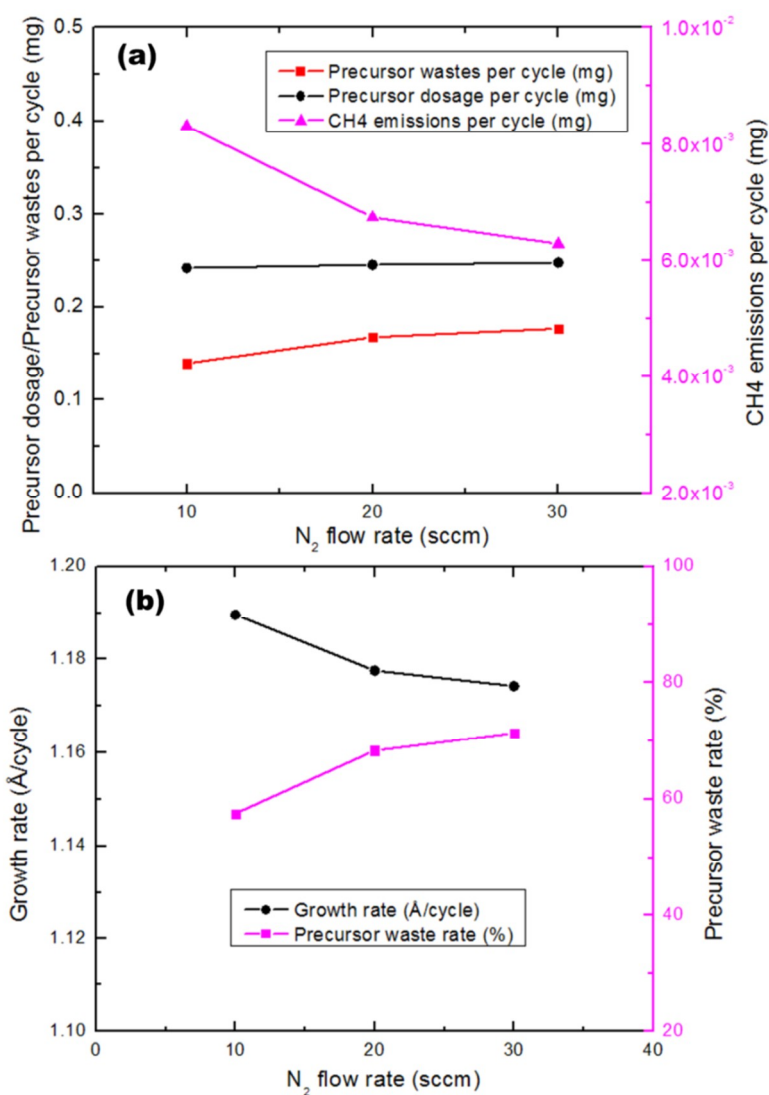


Figure 6.10 Effects of carrier gas flow rate on the process wastes and emissions (a) precursor dosage, precursor wastes and methane emissions and (b) film growth rate and precursor waste rate.

Carrier gas flow rate affects the surface deposition process and emissions by enhancing the convective heat and mass transfer in ALD system as revealed by Figure 6.10, in which three

levels of carrier gas flow rate 10, 20 and 30 sccm are investigated with 0.02/10/0.02/10 s ALD cycle at 200°C chamber temperature. As shown in Figure 6.10 (a), precursor wastes increase with higher flow rate. Total precursor wastes gathered from the outlet increase from 0.13 mg/cycle with 10 sccm flow rate to 0.18 mg/cycle with 30 sccm. Higher carrier gas flow rate shortens the contact time of precursors with substrate surface, and thus more unreacted precursor materials are carried out of the system.

As more unreacted precursor materials are purged by higher N<sub>2</sub> flow rate, less surface reactions are resulted in due to lower gaseous precursor concentrations on the wafer surface. The growth rate is decreased from 1.19 Å/cycle with 10 sccm carrier gas flow rate to 1.17 Å/cycle with 30 sccm. Methane emissions also decrease due to the weakened surface reactions. Because more precursor molecules are purged out without reacting with the surface species on substrate, the precursor waste rate is seen higher at higher flow rate in Figure 6.10 (b). From the results presented in Figure 6.10, lower carrier gas flow rate, e.g., 10 sccm is desirable to achieve higher growth rate, and meanwhile restrain the precursor waste rate.

## **6.5 Summary and conclusions**

This chapter systematically studied the transient deposition process and sustainability performance with the aid of DFT calculations regarding the Al<sub>2</sub>O<sub>3</sub> ALD reaction mechanisms. The detailed ALD surface reaction mechanisms including 10 elementary

surface reactions in Al<sub>2</sub>O<sub>3</sub> ALD process were examined and developed based on the DFT atomic-level investigations. The improved surface reaction mechanisms with accurate kinetic data were coupled and integrated in the physical thermal-fluid model. Using the numerical model, the transient deposition process was studied and analyzed by probing the distribution variations of the gaseous, surface and bulk species in a full Al<sub>2</sub>O<sub>3</sub> ALD cycle. The full-cycle ALD simulations revealed that the depositions of bulk material in ALD are in essence the chemisorption of the gaseous species and the conversion of surface species. The actual deposition process is heavily dependent on the interactions of these various species, which are essentially influenced by the process parameters.

To explore the effects of the four process parameters of temperature, pulse and purge procedures as well as the carrier gas flow rate on material deposition, process wastes and emissions, film growth rate on Si substrate was characterized, and methane emissions were gathered in both actual ALD system and numerical simulations. It is found by the studies that ALD process has very high material waste rate, and ~ 60% precursor dosage is wasted. It is also concluded that methane emissions are positively proportional to the film deposition process. Temperature fundamentally affects the ALD chemical process by changing the energy states in the surface reactions. Both experimental and numerical results show that moderate chamber temperature of 200°C results in higher growth rate and fewer precursor wastes. Too high temperature decreases the film growth rate by enhancing the decomposition process.

Pulse time is directly related to the precursor dosage. Longer pulse time enhances the deposition process, but also increases the precursor wastes which can weaken the sustainability performance. Purge time and carrier gas flow rate have very weak influences on deposition process, wastes and emissions. Purge time influence the ALD process by changing the gas-surface interaction time, and high carrier gas flow rate alters the ALD flow field by enhancing the convective heat and mass transfer in ALD process. The effects of the process parameters must be considered by minimizing the process wastes and emissions while maintaining a high deposition rate. In many cases, a trade-off must be made in defining the optimal process parameters.



# CHAPTER 7 CONCLUSIONS AND RECOMMENDATIONS FOR FUTURE STUDY

## 7.1 Conclusions

ALD was born with two serious sustainability issues, especially for industrial-level applications. One is the low throughput defined by its nature of depositing material in atomic level. Another is the potential negative environmental impacts, largely due to the highly toxic chemicals used in ALD process, toxic wastes, greenhouse gas emissions and nano-particle generations. This dissertation extensively studied the ALD process using both numerical and experimental methods with aims to better understand the transient physical and chemical processes, and identify the influential process or geometric factors to improve its throughput and minimize its emissions and wastes.

A mesoscopic numerical model was built based on Lattice Boltzmann Method to study the carrier gas flow in ALD vacuum reactor using two LBM models: LBGK-D2Q9 and TRT. The two models in both incompressible and compressible scenarios were compared in the aspects of flow features, stability and efficiency. The simulations showed that TRT model is superior to the LBGK-D2Q9 model with better stability and reliability especially in compressible scenarios. The flow in ALD was shown in a laminar steady state with velocity concentrated at the corners and around the wafer. Steady and evenly-distributed velocity field was demonstrated to contribute to higher precursor concentration near the wafer.

To further characterize the deposition process, a combined experimental and numerical study on the physical and chemical details of Al<sub>2</sub>O<sub>3</sub> ALD using TMA and water was conducted. Found in our experiments, the film deposition is positively dependent on temperature below 200°C. The growth rate declines at higher temperature, e.g., 250°C. The inlet sample has higher growth rate than other samples. Longer purging time slightly increases the growth rate, but specific sample responds differently. The reactive thermal-fluid dynamic model and simulation showed that ALD is a strictly self-limited process: surface deposition reactions are restrained once the surface species get saturated, even though the precursor material is still being introduced into the system. The ALD process is a complex strong-coupled fluid, thermal and chemical process which is not only heavily dependent on the chemical kinetics and surface conditions but also the flow and material distributions. The numerical simulations also clarified the experimental observations by correlating the deposition rate with precursor distributions. ALD process is a complex strong-coupled fluid, thermal and chemical process which is not only heavily dependent on the chemical kinetics and surface conditions but also the flow and material distributions.

Multi-wafer batch ALD process was studied to explore the effects of geometric factor on deposition process by comparing vertical and horizontal wafer arrangements. It was found from both experiments and simulations that the wafer layout indeed influences the deposition rates significantly. The vertical multi-wafer arrangement is superior to the horizontal one in film growth rate. By transient simulations, the experimental difference in

deposition rate was explained due to the significantly enhanced convective effect of chemical species transport to wafer surfaces in the vertical multi-wafer batch ALD process. The numerical simulations further revealed more details of the flow and surface reaction processes. Deposition process is under a joint influence of precursor concentration and surface site saturation status. The ALD deposition process is, in essence, a conversion of surface species with adsorptions of certain atoms on the substrate surface. Further data from the transient simulations also showed the overall position dependence of deposition rate in multi-wafer ALD process is weak and negligible.

Spatial ALD is promising in improving the ALD throughput. An in-line spatial ALD system was studied by numerical investigations in depositing  $\text{Al}_2\text{O}_3$  thin films. The effects of three geometric and process parameters, namely, gap size, temperature, and pumping pressure, were considered with three levels, respectively. By simulations, it's found that bigger gap (e.g., 2 mm) results in less precursor intermixing, but it generates slightly lower saturated deposition GPC level. The optimal gap size is heavily dependent on the trade-off between precursor intermixing and deposition rate. Wafer temperature is a significant factor in both flow and surface deposition processes. Higher temperature, 250°C for example, accelerates the diffusive mass transport which largely contributes to the precursor intermixing. Well-maintained pumping pressure is beneficial to decrease the concentration of precursor from the other side, but its effect on the deposition process is seen very weak. It was also concluded that the time scale of in-line spatial ALD process is only in tens of milliseconds.

As demonstrated in our study, it only takes  $\sim 30$  milliseconds for a specific point on the moving wafer belt to complete a full deposition cycle, with which, it is possible to define the wafer belt moving speed as  $\sim 0.67$  m/s. Considering the in-line spatial ALD is a continuous process without purging step, the overall throughput is shown as high as  $\sim 4$  nm/s, which is much higher compared to the conventional sing-wafer ALD with several nanometers growth in a minute.

In order to study and understand the formations of gaseous wastes and emissions in ALD process, the transient deposition process with detailed chemical reaction mechanisms of  $\text{Al}_2\text{O}_3$  ALD obtained from DFT calculations was investigated numerically and experimentally. The improved surface reaction mechanisms with accurate kinetic data were coupled and integrated in the physical thermal-fluid model to explore the effects of the four process parameters of temperature, pulse and purge procedures as well as the carrier gas flow rate on material deposition, process wastes and emissions.

It was found by the studies that ALD process has very high material waste rate, and  $\sim 60\%$  or more precursor dosage is wasted. It was also concluded that methane emissions are positively proportional to the film deposition process. Both experimental and numerical results showed that moderate chamber temperature of  $200^\circ\text{C}$  results in higher growth rate and fewer precursor wastes. Longer pulse time enhances the deposition process, but also increases the precursor wastes which can weaken the sustainability performance. Purge time

and carrier gas flow rate have very weak influences on deposition process, wastes and emissions. The effects of the process parameters must be considered by minimizing the process wastes and emissions while maintaining a high deposition rate.

## **7.2 Recommendations for future study**

In this dissertation, ALD process was explored extensively using both numerical and experimental methods. The LBM method was introduced in modeling the ALD flow. A robust reactive thermal-fluid dynamic numerical model was developed, and experiments were carried out to study the influential factors on throughput and ALD emissions. However, ALD is an extremely complex physical and chemical process, and there is still plenty of work to be done in better understanding the ALD process and improve its sustainability performance.

Firstly, mesoscopic methods such as the LBM method are versatile in simulating fluid phenomena especially for the cases with relatively higher vacuum such as ALD process. The theoretical part of LBM needs to be further developed to simulate phenomena including heat/mass transfer process, multi-component flow, multi-phase flow, as well as gas-solid surface reactions.

Secondly, fundamental experiments need to be carried out extensively in understanding the transient ALD deposition process. Especially, more surface chemical information needs to

be obtained from these experiments regarding the complex surface reaction mechanisms. For instance, the reactive thermal-fluid dynamic model is thirsty for such experimental data to be more accurate in characterizing the ALD deposition process. The possible complex side reactions involved in ALD process should also be explored experimentally.

In understanding and minimizing the potential hazard of ALD emissions and wastes, the experimental work on ALD wastes and emissions, especially nano-wastes formation mechanisms need to be carried out. Novel and effective in-situ nano-particle investigation methods need to be developed. The effective methods to collect and characterize nano-particles are needed. Numerical models which are capable of simulating the nano-wastes process in ALD are also needed in optimizing the deposition process.

Finally, in further improving the throughput of ALD, further systematic optimization work needs to be done both experimentally and numerically. Better ALD equipment can be devised such as plasma-enhanced ALD, roll-to-roll fast ALD.

## REFERENCES

Aarik, J., et al., Influence of carrier gas pressure and flow rate on atomic layer deposition of HfO<sub>2</sub> and ZrO<sub>2</sub> thin films, *Appl. Surf. Sci.*, 252 (2006) 5723-5734.

Adomaitis, R.A., A Ballistic Transport and Surface Reaction Model for Simulating Atomic Layer Deposition Processes in High-Aspect-Ratio Nanopores, *Chem. Vap. Deposition*, 17 (2011) 353-365.

Adomaitis, R.A., Development of a multiscale model for an atomic layer deposition process, *J. Cryst. Growth*, 312 (2010) 1449-1452.

Afshar, A., K.C. Cadien, Growth mechanism of atomic layer deposition of zinc oxide: A density functional theory approach, *Appl. Phys. Lett.*, 103 (2013).

Al-Jahmany, Y.Y., et al., Comparative study of lattice-Boltzmann and finite volume methods for the simulation of laminar flow through a 4 : 1 planar contraction, *Int. J. Numer. Methods Fluids*, 46 (2004) 903-920.

Anacleto, A.C., et al., Atomic layer deposition of tantalum nitride based thin films from cyclopentadienyl type precursor, *Thin Solid Films*, 519 (2010) 367-372.

Atkins, P., J. de Paula, *Physical Chemistry for the Life Sciences*, W. H. Freeman 2011.

Bergman, T.L., F.P. Incropera, *Fundamentals of Heat and Mass Transfer*, Wiley 2011.

Busnaina, A.A., et al., Nanomanufacturing and sustainability: opportunities and challenges, *J. Nanopart. Res.*, 15 (2013).

Chai, Z.H., et al., Multiple-relaxation-time lattice Boltzmann model for generalized Newtonian fluid flows, *Journal of Non-Newtonian Fluid Mechanics*, 166 (2011) 332-342.

Chai, Z.H., et al., Simulating high Reynolds number flow in two-dimensional lid-driven cavity by multi-relaxation-time lattice Boltzmann method, *Chinese Physics*, 15 (2006) 1855-1863.

Chang, R., *Physical Chemistry for the Biosciences*, University Science Books 2005.

Chapra, S., et al., *Numerical Methods for Engineers*, McGraw-Hill Higher Education 2010.

Cheng, H.E., et al., The effect of deposition temperature on the properties of TiN diffusion barriers prepared by atomic layer chemical vapor deposition, *Thin Solid Films*, 485 (2005) 59-65.

Chun, D.M., et al., A nano-particle deposition system for ceramic and metal coating at room temperature and low vacuum conditions, *International Journal of Precision Engineering and Manufacturing*, 9 (2008) 51-53.

Coronell, D.G., K.F. Jensen, Analysis of Transition Regime Flows in Low-Pressure Chemical Vapor-Deposition Reactors Using the Direct Simulation Monte-Carlo Method, *J. Electrochem. Soc.*, 139 (1992) 2264-2273.

Coronell, D.G., K.F. Jensen, Simulation of Rarefied-Gas Transport and Profile Evolution in Nonplanar Substrate Chemical-Vapor-Deposition, *J. Electrochem. Soc.*, 141 (1994) 2545-2551.

d'Humieres, D., et al., Multiple-relaxation-time lattice Boltzmann models in three dimensions, *Philosophical Transactions of the Royal Society of London Series a-Mathematical Physical and Engineering Sciences*, 360 (2002) 437-451.

Davis, M.E., R.J. Davis, *Fundamentals of Chemical Reaction Engineering*, Dover Publications 2012.

Delabie, A., et al., Reaction mechanisms for atomic layer deposition of aluminum oxide on semiconductor substrates, *J. Vac. Sci. Technol., A*, 30 (2012).



Delft, J.A.v., et al., Atomic layer deposition for photovoltaics: applications and prospects for solar cell manufacturing, *Semicond. Sci. Technol.*, 27 (2012) 074002.

Dkhissi, A., et al., Multiscale Modeling of the Atomic Layer Deposition of HfO<sub>2</sub> Thin Film Grown on Silicon: How to Deal with a Kinetic Monte Carlo Procedure, *J. Chem. Theory Comput.*, 4 (2008) 1915-1927.

Elliott, S.D., J.C. Greer, Simulating the atomic layer deposition of alumina from first principles, *J. Mater. Chem.*, 14 (2004) 3246-3250.

Fox, R.W., et al., *Introduction to Fluid Mechanics*, John Wiley & Sons Canada, Limited 2009.

George, S.M., Atomic Layer Deposition: An Overview, *Chem. Rev.*, 110 (2010) 111-131.

Gilmer, G.H., et al., Lattice Monte Carlo models of thin film deposition, *Thin Solid Films*, 365 (2000) 189-200.

Ginzburg, I., Equilibrium-type and link-type lattice Boltzmann models for generic advection and anisotropic-dispersion equation, *Advances in Water Resources*, 28 (2005) 1171-1195.

Ginzburg, I., et al., Two-relaxation-time Lattice Boltzmann scheme: About parametrization, velocity, pressure and mixed boundary conditions, *Communications in Computational Physics*, 3 (2008) 427-478.

Gobbert, M.K., et al., Modeling and simulation of atomic layer deposition at the feature scale, *J. Vac. Sci. Technol., B*, 20 (2002) 1031-1043.

Goldstein, D.N., et al., Al<sub>2</sub>O<sub>3</sub> Atomic Layer Deposition with Trimethylaluminum and Ozone Studied by in Situ Transmission FTIR Spectroscopy and Quadrupole Mass Spectrometry, *J. Phys. Chem. C*, 112 (2008) 19530-19539.

Gou, F., et al., The application of molecular dynamics to the study of plasma-surface interactions: CF<sub>x</sub> with silicon, *Int. Rev. Phys. Chem.*, 27 (2008) 229-271.

Granneman, E., et al., Batch ALD: Characteristics, comparison with single wafer ALD, and examples, *Surface & Coatings Technology*, 201 (2007) 8899-8907.

Groner, M.D., et al., Low-temperature Al<sub>2</sub>O<sub>3</sub> atomic layer deposition, *Chem. Mater.*, 16 (2004) 639-645.

Guo, Z.L., et al., Lattice BGK model for incompressible Navier-Stokes equation, *Journal of Computational Physics*, 165 (2000) 288-306.

Halls, M.D., K. Raghavachari, Atomic layer deposition growth reactions of Al<sub>2</sub>O<sub>3</sub> on Si(100)-2 x 1, *J. Phys. Chem. B*, 108 (2004) 4058-4062.

Halls, M.D., K. Raghavachari, Atomic layer deposition of Al<sub>2</sub>O<sub>3</sub> on H-passivated Si. I. Initial surface reaction pathways with H/Si(100)-2X1, *J. Chem. Phys.*, 118 (2003) 10221-10226.

Hamalainen, J., et al., Atomic Layer Deposition of Noble Metals and Their Oxides, *Chem. Mater.*, 26 (2014) 786-801.

Hass, K.C., et al., The chemistry of water on alumina surfaces: Reaction dynamics from first principles, *Science*, 282 (1998) 265-268.

Haukka, S., ALD Technology - Present and Future Challenges, *ECS Transactions*, 3 (2007) 15-26.

He, X.Y., et al., Lattice Boltzmann simulation of diffusion-convection systems with surface chemical reaction, *Mol. Simulat.*, 25 (2000) 145-156.

Higashi, G.S., C.G. Fleming, Sequential Surface Chemical-Reaction Limited Growth of

High-Quality Al<sub>2</sub>O<sub>3</sub> Dielectrics, *Appl. Phys. Lett.*, 55 (1989) 1963-1965.

Hirvikorpi, T., et al., Barrier properties of plastic films coated with an Al<sub>2</sub>O<sub>3</sub> layer by roll-to-roll atomic layer deposition, *Thin Solid Films*, 550 (2014) 164-169.

Hoffman, J.D., S. Frankel, *Numerical Methods for Engineers and Scientists, Second Edition*, Taylor & Francis 2001.

Holmqvist, A., et al., A model-based methodology for the analysis and design of atomic layer deposition processes-Part I: Mechanistic modelling of continuous flow reactors, *Chem. Eng. Sci.*, 81 (2012) 260-272.

Holmqvist, A., et al., A model-based methodology for the analysis and design of atomic layer deposition processes-Part II: Experimental validation and mechanistic analysis, *Chem. Eng. Sci.*, 94 (2013) 316-329.

Hsueh, Y.C., et al., Fabrication of catalyst by atomic layer deposition for high specific power density proton exchange membrane fuel cells, *J. Catal.*, 294 (2012) 63-68.

Hu, Z., et al., Molecular dynamics simulation of the Al<sub>2</sub>O<sub>3</sub> film structure during atomic layer deposition, *Mol. Simulat.*, 35 (2009) 270-279.

Johansson, P., et al., Atomic layer deposition process for barrier applications of flexible packaging, Tappi 2010 PLACE Conference, TAPPI, 2010.

Kays, W., et al., *Convective Heat & Mass Transfer W/ Engineering Subscription Card*, McGraw-Hill Companies, Incorporated 2005.

King, P.J., et al., Effect of deposition temperature on the properties of CeO<sub>2</sub> films grown by atomic layer deposition, *Thin Solid Films*, 519 (2011) 4192-4195.

Klaus, J.W., et al., Atomic layer deposition of tungsten nitride films using sequential surface

reactions, *J. Electrochem. Soc.*, 147 (2000) 1175-1181.

Ko, C.H., W.J. Lee, Formation of Al<sub>2</sub>O<sub>3</sub>-TiO<sub>2</sub> bilayer using atomic layer deposition and its application to dynamic random access memory, *J. Solid State Electrochem.*, 11 (2007) 1391-1397.

Krajewski, T., et al., The influence of growth temperature and precursors' doses on electrical parameters of ZnO thin films grown by atomic layer deposition technique, *Microelectron. J.*, 40 (2009) 293-295.

Kukli, K., et al., Influence of growth temperature on properties of zirconium dioxide films grown by atomic layer deposition, *J. Appl. Phys.*, 92 (2002) 1833-1840.

Kukli, K., et al., Influence of thickness and growth temperature on the properties of zirconium oxide films grown by atomic layer deposition on silicon, *Thin Solid Films*, 410 (2002) 53-60.

Kurhekar, A.S., P. Apte, Spectroscopic-ellipsometric study of native oxide removal by liquid phase HF process, *Int. Nano Lett.*, 3 (2013) 10.

Lallemand, P., L.S. Luo, Theory of the lattice Boltzmann method: Dispersion, dissipation, isotropy, Galilean invariance, and stability, *Physical Review E*, 61 (2000) 6546-6562.

Lankhorst, A.M., et al., Transient ALD simulations for a multi-wafer reactor with trenched wafers, *Surface & Coatings Technology*, 201 (2007) 8842-8848.

Lee, Y.J., Low-impurity, highly conformal atomic layer deposition of titanium nitride using NH<sub>3</sub>-Ar-H<sub>2</sub> plasma treatment for capacitor electrodes, *Mater. Lett.*, 59 (2005) 615-617.

Li, M.Y., et al., Effect of process pressure on atomic layer deposition of Al<sub>2</sub>O<sub>3</sub>, *J. Electrochem. Soc.*, 154 (2007) H967-H972.

Li, Q., et al., Additional interfacial force in lattice Boltzmann models for incompressible multiphase flows, *Physical Review E*, 85 (2012).

Luo, L.S., et al., Numerics of the lattice Boltzmann method: Effects of collision models on the lattice Boltzmann simulations, *Physical Review E*, 83 (2011).

Ma, L., et al., Atomic layer deposition of Al<sub>2</sub>O<sub>3</sub> process emissions, *RSC Advances*, 5 (2015) 12824-12829.

Martys, N.S., H.D. Chen, Simulation of multicomponent fluids in complex three-dimensional geometries by the lattice Boltzmann method, *Physical Review E*, 53 (1996) 743-750.

Martys, N.S., J.F. Douglas, Critical properties and phase separation in lattice Boltzmann fluid mixtures, *Physical Review E*, 63 (2001).

Maydannik, P., et al., An atomic layer deposition process for moving flexible substrates, *Chem. Eng. J.*, 171 (2011) 345-349.

Mazaleyrat, G., et al., A methodology for the kinetic Monte Carlo simulation of alumina atomic layer deposition onto silicon, *Comput. Mater. Sci.*, 33 (2005) 74-82.

McDonnell, S., et al., Trimethyl-aluminum and ozone interactions with graphite in atomic layer deposition of Al<sub>2</sub>O<sub>3</sub>, *J. Appl. Phys.*, 112 (2012).

Meng, X.B., et al., Emerging Applications of Atomic Layer Deposition for Lithium-Ion Battery Studies, *Adv. Mater.*, 24 (2012) 3589-3615.

Mills, A.F., *Basic Heat and Mass Transfer: Pearson New International Edition*, Pearson Education, Limited 2013.

Mistry, K., et al., A 45nm Logic Technology with High-k+Metal Gate Transistors, *Strained*

Silicon, 9 Cu Interconnect Layers, 193nm Dry Patterning, and 100% Pb-free Packaging, Electron Devices Meeting, 2007. IEDM 2007. IEEE International, 2007, pp. 247-250.

Mohamad, A.A., Lattice Boltzmann Method: Fundamentals and Engineering Applications with Computer Codes, Springer London 2011.

Mousa, M.B.M., et al., Effect of temperature and gas velocity on growth per cycle during Al<sub>2</sub>O<sub>3</sub> and ZnO atomic layer deposition at atmospheric pressure, J. Vac. Sci. Technol., A, 30 (2012).

Mousa, M.B.M., et al., Atmospheric Pressure Atomic Layer Deposition of Al<sub>2</sub>O<sub>3</sub> Using Trimethyl Aluminum and Ozone, Langmuir, 30 (2014) 3741-3748.

Munson, B.R., Fundamentals of Fluid Mechanics 6th Edition with WileyPlus 5th Edition Set, John Wiley & Sons Canada, Limited 2008.

Narayan, R.J., et al., Atomic layer deposition-based functionalization of materials for medical and environmental health applications, Philosophical Transactions of the Royal Society a-Mathematical Physical and Engineering Sciences, 368 (2010) 2033-2064.

Niu, W., et al., Applications of atomic layer deposition in solar cells, Nanotechnology, 26 (2015) 064001.

Okuyama, Y., et al., Batch process for atomic layer deposition of hafnium silicate thin films on 300-mm-diameter silicon substrates, J. Vac. Sci. Technol., A, 23 (2005) L1-L3.

Owyang, J., L. Bartholomew, Implementing a batch atomic layer deposition approach for advanced DRAM dielectrics, Micro, 23 (2005) 49-+.

Pan, D., et al., On the physical and chemical details of alumina atomic layer deposition: A combined experimental and numerical approach, J. Vac. Sci. Technol., A, 33 (2015).

Pan, D.Q., et al., Numerical modeling of carrier gas flow in atomic layer deposition vacuum reactor: A comparative study of lattice Boltzmann models, *J. Vac. Sci. Technol., A*, 32 (2014).

Poodt, P., et al., Spatial atomic layer deposition: A route towards further industrialization of atomic layer deposition, *J. Vac. Sci. Technol., A*, 30 (2012).

Poodt, P., et al., Low temperature and roll-to-roll spatial atomic layer deposition for flexible electronics, *J. Vac. Sci. Technol., A*, 30 (2012).

Poodt, P., et al., High-Speed Spatial Atomic-Layer Deposition of Aluminum Oxide Layers for Solar Cell Passivation, *Adv. Mater.*, 22 (2010) 3564-+.

Poodt, P., et al., On the kinetics of spatial atomic layer deposition, *J. Vac. Sci. Technol., A*, 31 (2013).

Puurunen, R.L., Growth per cycle in atomic layer deposition: A theoretical model, *Chem. Vap. Deposition*, 9 (2003) 249-257.

Puurunen, R.L., Growth per cycle in atomic layer deposition: Real application examples of a theoretical model, *Chem. Vap. Deposition*, 9 (2003) 327-332.

Puurunen, R.L., Surface chemistry of atomic layer deposition: A case study for the trimethylaluminum/water process, *J. Appl. Phys.*, 97 (2005).

Raabe, D., Overview of the lattice Boltzmann method for nano- and microscale fluid dynamics in materials science and engineering, *Modell. Simul. Mater. Sci. Eng.*, 12 (2004) R13-R46.

Rai, V.R., et al., Influence of surface temperature on the mechanism of atomic layer deposition of aluminum oxide using an oxygen plasma and ozone, *Langmuir*, 28 (2012) 350-357.

Regulski, W., J. Szumbariski, Numerical simulation of confined flows past obstacles - the comparative study of Lattice Boltzmann and Spectral Element Methods, *Archives of Mechanics*, 64 (2012) 423-456.

Remmers, E.M., et al., Reaction factorization for the dynamic analysis of atomic layer deposition kinetics, *Chem. Eng. Sci.*, 127 (2015) 374-391.

Ritala, M., et al., Perfectly Conformal TiN and Al<sub>2</sub>O<sub>3</sub> Films Deposited by Atomic Layer Deposition, *Chem. Vap. Deposition*, 5 (1999) 7-9.

Sammelseg, V., et al., TiO<sub>2</sub> thin films by atomic layer deposition: a case of uneven growth at low temperature, *Appl. Surf. Sci.*, 134 (1998) 78-86.

Santala, E., et al., The preparation of reusable magnetic and photocatalytic composite nanofibers by electrospinning and atomic layer deposition, *Nanotechnology*, 20 (2009).

Sbragaglia, M., S. Succi, Analytical calculation of slip flow in lattice Boltzmann models with kinetic boundary conditions, *Physics of Fluids*, 17 (2005).

Scarel, G., et al., Effects of growth temperature on the properties of atomic layer deposition grown ZrO<sub>2</sub> films, *J. Vac. Sci. Technol., A*, 21 (2003) 1359-1365.

Sengul, H., et al., Toward sustainable nanoproducts: An overview of nanomanufacturing methods, *Journal of Industrial Ecology*, 12 (2008) 329-359.

Shim, J.H., et al., Catalysts with Pt Surface Coating by Atomic Layer Deposition for Solid Oxide Fuel Cells, *J. Electrochem. Soc.*, 157 (2010) B793-B797.

Shokouhmand, H., A.H.M. Isfahani, An improved thermal lattice Boltzmann model for rarefied gas flows in wide range of Knudsen number, *International Communications in Heat and Mass Transfer*, 38 (2011) 1463-1469.



Shu, T., et al., Fabrication of platinum electrocatalysts on carbon nanotubes using atomic layer deposition for proton exchange membrane fuel cells, *Electrochim. Acta*, 75 (2012) 101-107.

Skoog, S.A., et al., Atomic layer deposition: medical and biological applications, *Int. Mater. Rev.*, 58 (2013) 113-129.

Soto, C., W.T. Tysoe, The Reaction Pathway for the Growth of Alumina on High Surface-Area Alumina and in Ultrahigh-Vacuum by a Reaction between Trimethyl Aluminum and Water, *J. Vac. Sci. Technol., A*, 9 (1991) 2686-2695.

Suh, S., et al., Investigation on spatially separated atomic layer deposition by gas flow simulation and depositing Al<sub>2</sub>O<sub>3</sub> films, *J. Vac. Sci. Technol., A*, 30 (2012).

Wang, Y., Nanomanufacturing technologies: advances and opportunities, *Proceedings of the 18th International Conference on Management of Technology*, 2009.

Widjaja, Y., C.B. Musgrave, Quantum chemical study of the mechanism of aluminum oxide atomic layer deposition, *Appl. Phys. Lett.*, 80 (2002) 3304-3306.

Wind, R.A., S.M. George, Quartz Crystal Microbalance Studies of Al<sub>2</sub>O<sub>3</sub> Atomic Layer Deposition Using Trimethylaluminum and Water at 125 degrees C, *J. Phys. Chem. A*, 114 (2010) 1281-1289.

Xie, Y., et al., Mechanistic modeling of atomic layer deposition of alumina process with detailed surface chemical kinetics, *Chem. Eng. J.*, 259 (2015) 213-220.

Yanguas-Gil, A., J.W. Elam, Simple model for atomic layer deposition precursor reaction and transport in a viscous-flow tubular reactor, *J. Vac. Sci. Technol., A*, 30 (2012).

Ylilammi, M., Mass-Transport in Atomic Layer Deposition Carrier Gas Reactors, *J. Electrochem. Soc.*, 142 (1995) 2474-2479.

Yu, M.P., et al., Performance enhancement of a graphene-sulfur composite as a lithium-sulfur battery electrode by coating with an ultrathin Al<sub>2</sub>O<sub>3</sub> film via atomic layer deposition, *Journal of Materials Chemistry A*, 2 (2014) 7360-7366.

Yuan, C.Y., D. Dornfeld, Environmental performance characterization of atomic layer deposition, *Electronics and the Environment*, 2008. ISEE 2008. IEEE International Symposium on, 2008, pp. 1-6.

Yuan, C.Y., D.A. Dornfeld, Integrated Sustainability Analysis of Atomic Layer Deposition for Microelectronics Manufacturing, *Journal of Manufacturing Science and Engineering-Transactions of the Asme*, 132 (2010).

Zhang, J.F., D.Y. Kwok, Pressure boundary condition of the lattice Boltzmann method for fully developed periodic flows, *Physical Review E*, 73 (2006).

Zou, Q.S., X.Y. He, On pressure and velocity boundary conditions for the lattice Boltzmann BGK model, *Physics of Fluids*, 9 (1997) 1591-1598.

# CURRICULUM VITAE

## Dongqing Pan

Place of Birth: Shaanxi, China

## Education

Ph.D., University of Wisconsin-Milwaukee, 5/2016

Major: Mechanical engineering

Minor: Chemistry

M.S., Harbin Institute of Technology, China, 7/2009

Major: Mechanical engineering

B.S., Nanjing University of Aeronautics and Astronautics, China, 6/2007

Major: Mechanical engineering

**Dissertation Title:** Numerical and Experimental Studies of Atomic Layer Deposition for Sustainability Improvement

## Publications

### Peer-reviewed journal papers

1. **Dongqing Pan**, Tao Li, Tien Chien Jen, Chris Yuan. "Numerical Modeling of Carrier Gas Flow in Atomic Layer Deposition (ALD) Process: a Comparative Study of Lattice Boltzmann Models", *Journal of Vacuum Science and Technology A*, 32(1), 01A110
2. **Dongqing Pan**, Lulu Ma, Yuanyuan Xie, Tien Chien Jen, Chris Yuan. "On the Physical and Chemical Details of Alumina Atomic Layer Deposition: a Combined Experimental and Numerical Approach", *Journal of Vacuum Science and Technology A*, 33 (2), 021511

3. **Dongqing Pan**, Lulu Ma, Yuanyuan Xie, Fenfen Wang, Tien Chien Jen, Chris Yuan. “Experimental and numerical investigations into the transient multi-wafer batch atomic layer deposition process with vertical and horizontal wafer arrangements”, *International Journal of Heat and Mass Transfer*, 91 (2015) 416-427
4. **Dongqing Pan**, Tien Chien Jen, Chris Yuan. “Effects of gap size, temperature and pumping pressure on the fluid dynamics and chemical kinetics of in-line spatial atomic layer deposition of Al<sub>2</sub>O<sub>3</sub>”, *International Journal of Heat and Mass Transfer*, 96 (2016) 189-198
5. **Dongqing Pan**, Dongsheng Guan, Tien Chien Jen, Chris Yuan. “Atomic Layer Deposition Process Modeling and Experimental Investigation for Sustainable Manufacturing of Nano Thin Films”, *Journal of Manufacturing Science and Engineering*, **under review**
6. Yuanyuan Xie, Lulu Ma, **Dongqing Pan**, Chris Yuan. “Mechanistic Modeling of Atomic Layer Deposition of Alumina Process with Detailed Surface Chemical Kinetics”, *Chemical Engineering Journal*, Volume 259, 2015, 213–220
7. Lulu Ma, **Dongqing Pan**, Yuanyuan Xie, Chris Yuan. “Atomic Layer Deposition of Al<sub>2</sub>O<sub>3</sub> Process Emissions”, *RSC Advances*, 5 (2015) 12824-12829
8. Yuanyuan Xie, **Dongqing Pan**, Lulu Ma, Chris Yuan. “Optimizing the process efficiency of atomic layer deposition of alumina for its sustainability improvement”, *Journal of Materials Chemistry A*, **under revision**
9. Lulu Ma, **Dongqing Pan**, Yuanyuan Xie, Fenfen Wang, Chris Yuan. “Experimental Study of Process Emissions from Atomic Layer Deposition of Al<sub>2</sub>O<sub>3</sub> under Various Temperatures and Purge Time”, *Environmental Science: Nano*, **under review**
10. Dongsheng Guan, Lulu Ma, **Dongqing Pan**, Jianyang Li, Xianfeng Gao, Yuanyuan Xie, Ming Qiu and Chris Yuan. “Enhancing the Cycling Stability of SnS<sub>2</sub> Anodes by Atomic Layer Deposition of Metal Oxides for Durable Lithium-Ion Batteries”, *ACS Applied Materials & Interfaces*, **under review**

## Conference papers/posters

1. **Dongqing Pan**, Chris Yuan. “Numerical Characterizations of Gas Fluid Dynamics and Chemical Kinetics in Alumina Atomic Layer Deposition Vacuum Reactor”, *Proceedings of 15<sup>th</sup> International Conference on Atomic Layer Deposition*, June 28-July 1, 2015, Portland, Oregon, USA
2. Lulu Ma, **Dongqing Pan**, Fenfen Wang, Yuanyuan Xie and Chris Yuan. “Sustainability of Atomic Layer Deposition Nanotechnology”, *Proceedings of 4<sup>th</sup> International Congress on Sustainability Science & Engineering*, May 26-29, 2015, Balatonfüred, Hungary
3. Chris Yuan, **Dongqing Pan**, Lulu Ma, Xianfeng Gao, Jianyang Li, Yuanyuan Xie. “Sustainable Development of Atomic Layer Deposition for Clean Energy Applications”. *Proceedings of the 2014 TechWorld- Nanotech, Microtech, Biotech, Cleantech Joint Conferences*, June 15-19, 2014, Washington D.C.
4. Chris Yuan, **Dongqing Pan**, Lulu Ma, Endong Wang, Xianfeng Gao “Integrated Sustainability Analysis and Life Cycle Assessment of Atomic Layer Deposition for Clean Energy Applications”, *Proceedings of the 2013 Sustainable Nanotechnology Organization Conference*, Santa Barbara, CA, Nov. 2-4, 2013.

## **Patents**

1. Guangyu Zhang, Zhongguo Wang, **Dongqing Pan**, Wenping Song, Huijuan Zhang, “A butt-joint water detection and blocking equipment”, 2012, Patent No. CN200810137183.6
2. Guangyu Zhang, **Dongqing Pan**, Zhongguo Wang, Wuyi Wang, Zhigang Chen, “A downhole cable fixation and protection device”, 2010, Patent No. CN200810137160.5
3. Guangyu Zhang, **Dongqing Pan**, Longqiu Li, Hongtao Zhang, Huijuan Zhang, “A rubber-filling type under-well armor cable connection apparatus”, 2009, Patent No.

### **Honors/Awards**

- Chancellor's Graduate Award, University of Wisconsin-Milwaukee, 2016
  
- Second Place, CEAS Student Research Poster Competition, University of Wisconsin, Milwaukee, April, 2015
  
- Student Travel Award, University of Wisconsin-Milwaukee, March, 2015
  
- CEAS Dean's Scholarship, University of Wisconsin-Milwaukee, 2014 – 2015
  
- Chancellor's Graduate Award, University of Wisconsin-Milwaukee, 2013 – 2014
  
- Excellent Student Scholarship, Harbin Institute of Technology, 2007 – 2008
  
- Excellent Student Scholarship, Nanjing University of Aeronautics and Astronautics, 2005 – 2007
  
- National Stipend Fellowship, Nanjing University of Aeronautics and Astronautics, 2004